



FINAL REPORT

RADOME FACILITY

Report No. 0038-RF-1

Prepared For:

National Aeronautics and Space Administration  
Goddard Space Flight Center  
Greenbelt, Maryland

Under:

Contract No. NAS 5-3232

Comsat Research Branch Code 625

CONDUCTRON CORPORATION  
343 S. Main Street  
Ann Arbor, Michigan

TABLE OF CONTENTS

1. INTRODUCTION . . . . .	.1-1
2. RADOME SUPPORT FACILITY . . . . .	.2-1
3. RADOME . . . . .	.3-1
3.1 Radome Construction.....	.3-1
3.2 Radome Operation . . . . .	.3-1
3.3 Radome Erection . . . . .	.3-6
3.4 Electrical Evaluation . . . . .	.3-8
3.4.1 Reflection Coefficients . . . . .	.3-9
3.4.2 Analysis of Radome - Target Interaction Effects . . . . .	.3-17
3.4.2.1 High-Frequency Scattering from a Conducting Sphere Surrounded by a Thin-Wall Radome . . . . .	.3-17
3.4.2.2 Target Location . . . . .	.3-28
3.4.3 Measurement Considerations . . . . .	.3-30
3.4.4 Experimental Evaluation . . . . .	.3-33
3.4.5 The Radome as a Housing for a Transmitting Antenna . . . . .	.3-50
4. TEST FIXTURE . . . . .	.4-1
4.1 Construction of Basic Structure . . . . .	.4-1
4.2 Construction of the Torus . . . . .	.4-6
5. INSTRUMENTATION . . . . .	.5-1
5.1 R. F. System . . . . .	.5-1
5.2 Pressure Monitoring System . . . . .	.5-5
5.3 Positioning System . . . . .	.5-5
5.4 Bistatic Cart . . . . .	.5-6
APPENDIX A - SUPPORT FACILITY DRAWINGS	
APPENDIX B - TEST FIXTURE DRAWINGS	

## TABLE OF ILLUSTRATIONS

2.1	Master Control Room . . . . .	.2-2
2.2	Hydraulic Pump and Fluid Storage Unit . . . . .	.2-5
3.1	Radome . . . . .	.3-2
3.2	Blower System . . . . .	.3-3
3.3	Operating Pressure as a Function of Wind Velocity . . . . .	.3-5
3.4	Furnace System . . . . .	.3-7
3.5	Geometry for Analysis of Two Parallel Dielectric Sheets . . . . .	.3-10
3.6	Reflection Coefficients of a Two-Layer Dielectric Sandwich . . . . .	.3-14
3.7	Radome Reflection Coefficient as a Function of Frequency . . . . .	.3-16
3.8	Optimum Location of the Measurement Fixture . . . . .	.3-31
3.9	Block Diagram of a Typical Bistatic CW Measurement System . . . . .	.3-35
3.10	Measurement Pattern . . . . .	.3-36
3.11	" " . . . . .	.3-37
3.12	" " . . . . .	.3-38
3.13	" " . . . . .	.3-39
3.14	" " . . . . .	.3-40
3.15	" " . . . . .	.3-41
3.16	" " . . . . .	.3-42
3.17	" " . . . . .	.3-43
3.18	" " . . . . .	.3-44
3.19	" " . . . . .	.3-45
3.20	" " . . . . .	.3-46
3.21	" " . . . . .	.3-47
3.22	" " . . . . .	.3-48
4.1	Test Fixture, Front View . . . . .	.4-2
4.2	Test Fixture, Rear View . . . . .	.4-3
4.3	Rim Attachments . . . . .	.4-5
4.4	Mounting Plate Attachments . . . . .	.4-5
4.5	Torus, Bladder Inflated . . . . .	.4-7
4.6	Torus, Bladder Deflated . . . . .	.4-8
4.7	Radius of Curvature VS Deflection for a 22 foot Diaphragm Tester . . . . .	.4-9

4.8	Pressure VS Stress for S-SIN-1 & 2 Material at Various Radii ( $t = 7.35 \times 10^{-4}$ in) . . . . .	4-11
4.9	Bladder Test Fixture . . . . .	4-14
4.10	Comparison of Theory & Experiment 6" Bladder . . . . .	4-15
4.11	Comparison of Theory & Experiment 8" Bladder . . . . .	4-16
5.1	Radome Facility Instrumentation . . . . .	5-2
5.2	Reflection Measurement System . . . . .	5-1
5.3	Antennas Used for a Transmission Measurements as Mounted on the Test Fixture . . . . .	5-4
5.4	Bistatic Cart . . . . .	5-7



1. INTRODUCTION

This report describes work performed under Contract No. NAS-5-3232 dealing specifically with the construction, installation and check out of a radome measurement facility located at the Conductron Radar Cross Section Measurement Range in Augusta Township, Washtenaw County, Michigan. The purpose of this facility is to provide a capability for the electrical evaluation of passive communications satellite materials.

The report discusses the support facility, the radome, the radome installation and electrical evaluation, and the facility instrumentation. As presently designed this facility provides a capability for measuring the microwave reflection and transmission characteristics of reflective materials. Twenty-two foot segments of passive communications satellites up to 400 feet in diameter can be evaluated. With this fixture, it is possible to maintain the segment radius of curvature as material skin stress increases for any material which would be practical in the design of passive communications satellites.

## 2. RADOME SUPPORT FACILITY

The radome support facility encompasses all of the structures which are necessary to make the test site operational but which, because of their nature, cannot be removed from the site. These structures include the working buildings and storage space, the concrete runways around the site, and the hydraulic equipment in the radome. A complete set of facility drawings is shown in Appendix A.

All working buildings and storage areas were constructed underground for the purpose of minimizing radar reflection problems. There are two separate underground rooms. The master control room is located at one end of the facility and the radome equipment room is located at the other end, directly under the radome. The general layout and size of these rooms is shown in Appendix A.

A picture of the master control room is shown in Figure 2.1. This room has a floor space of approximately 324 square feet and houses all microwave equipment, pressure monitoring equipment, and position monitoring and control equipment for both the antennas and the test fixture. A reinforced concrete slab floor, 4 inches thick, rests on reinforced concrete perimeter footings 20 inches deep by 12 inches wide. A minimum of 4 inches of sand fill was used under the floor. The walls are constructed of 12 inch concrete block reinforced every third course with "Wal-Lock" and waterproofed with two coats of Thoroseal. The ceiling was slightly pitched and constructed of preformed concrete slabs 18 feet long, 4 feet wide and 5 inches thick, which span the exterior walls. The finished ceiling was intentionally constructed to be below the final grade level so that final grading could be accomplished by gravel fill. The gravel and the slight pitch which was built into the ceiling prevent an excessive amount of ground water from accumulating. Access to the room is gained by a set of wooden stairs which were made portable so that heavy, delicate equipment, such as microwave receivers and recorders, could be transported by an overhead crane. The floor plan of the rooms underneath the radome is shown in Appendix A. As can be seen, the general room area is irregular in shape, conforming to the circular contour of the radome pad support footing. The total floor space is approximately 672 square feet. The outside walls are recessed 12 inches from the radome pad footing and are constructed of 12 inch concrete block. These walls are reinforced every third course with "Wal-Lock" and are sealed on the outside with two coats of Thoroseal. The interior walls are constructed of 8 inch block and are also reinforced every third course

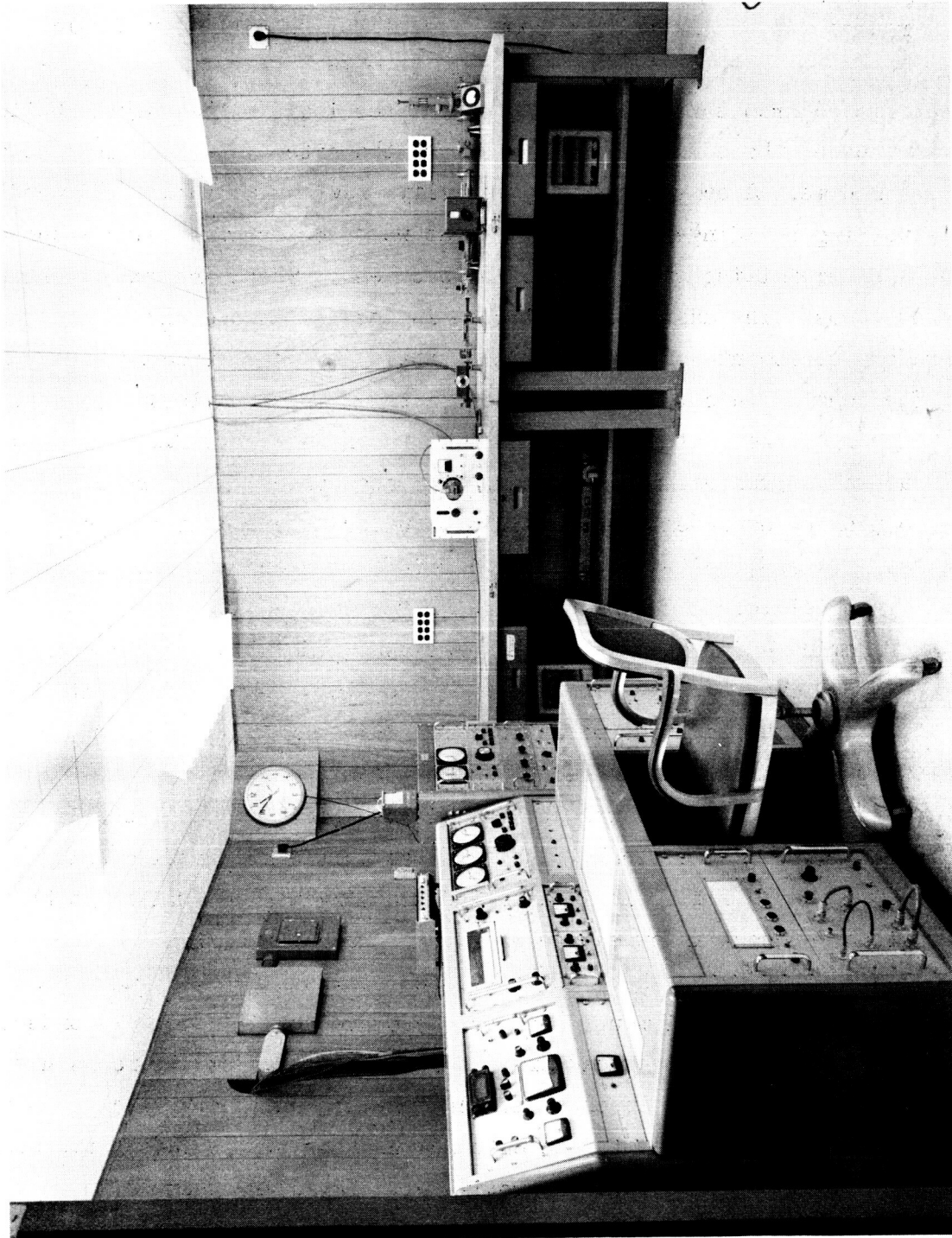


Figure 2.1 Master Control Room

with "Wal-Lock".

The blower room has a floor space of approximately 200 square feet and houses the radome inflation blower system and the emergency power system, which are discussed in detail in Section 3 of this report, and shown in Figure 3.2. The duct which supplies make-up air for the blower system was brought in through one wall of the blower room. The air duct is constructed of preformed concrete pipe, having an inside diameter of 30 inches, and is approximately 195 feet long. The positioning of the duct is shown in Appendix A. The primary reason for the length of the duct is that in order to provide enough air, the intake port must be removed from any obstruction which might cause turbulence. The radome causes significant air turbulence under windy conditions. The duct also provides a method for running instrumentation cables between the radome and the master control room. An eight inch duct connects the master control room to the make-up air duct for this purpose.

The furnace room has a floor space of approximately 200 square feet and houses the furnace, the hydraulic pump and the hydraulic fluid storage units. The furnace is described in Section 3.3 of this report and shown in Figure 3.4. The hydraulic system is discussed below.

The concrete runways provide surfaces over which materials and equipment can be moved with a minimum of difficulty. The runway which is shown as the bistatic track in Appendix A provides a surface for movement of the antenna towers. This track is 86.5 feet long, 8 feet wide and 5 inches thick, and rests on a minimum of 1 foot of sand fill. The front edge of the track is a 30 degree segment of a circle 150 feet in radius. The runway which connects the bistatic track to the radome pad is 120 feet long, 12 feet wide and 5 inches thick, and also rests on a minimum of 1 foot of sand fill.

The radome pad is made of reinforced concrete and is 64 feet in diameter and 6 inches thick. It rests on a reinforced footing, 48 inches deep by 10 inches wide, extending around the entire perimeter. Part of the pad serves as the ceiling for the underground rooms and the remainder was constructed over at least 2 feet of sand fill. The pad surface within the radome is flat while outside, the pad slopes sharply down to the final grade level in order to provide drainage.

The radome is attached to the pad by means of anchor bolts set in the concrete. Being an air supported structure, the radome exerts a considerable lifting force on

the attachment bolts. In the maximum pressure condition the total lifting force is in excess of 200,000 pounds. A total of 96 anchor bolts are used (as shown in Drawing No. Sk 1946 in Appendix A) making the lifting force on each bolt slightly in excess of 2,000 pounds. The anchor bolts are welded to reinforcing rods which extend around the entire radome perimeter. These rods are attached periodically to other rods which extend down into the footings. This is shown in detail in Appendix A. The attachment method spreads the lifting force uniformly over the attachment area and provides a uniform surface which will not be affected by frost heaving.

A hydraulic system has been installed inside the radome to lift the test fixture above the radome floor so that radar reflection and transmission measurements can be made. The hydraulic post and cylinder was manufactured by the Joyce-Gridland Company and has 14 feet of travel. The post is shown in the fully extended position in Figures 4.1 and 4.2. The post is powered by a single phase 220 Volt electric pump rated at 5 hp. Hydraulic fluid reservoirs having a total capacity of 132 gallons have been provided. This equipment is shown in Figure 2.2. A non-rotating device has been incorporated into the system so that a fixed angular reference can be obtained. The height of the hydraulic post is controlled by means of push button switches located in the stairwell leading from the air lock to the radome. The post position and the test fixture position can thus be observed while changes in the post position are being made. The post position can be changed in increments of less than 0.25 inch using the push button controls.

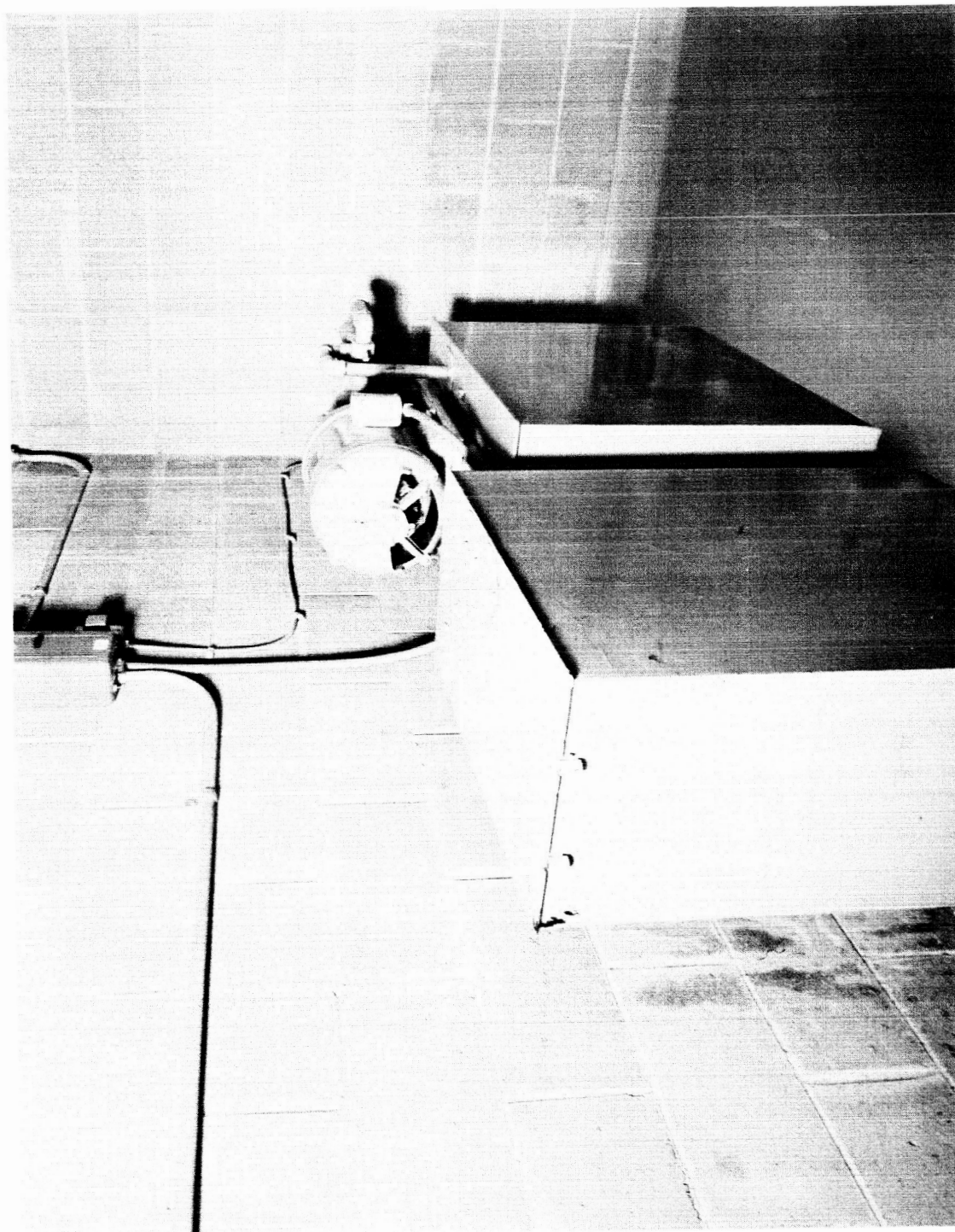


Figure 2.2 Hydraulic Pump and Fluid Storage Unit

### 3. RADOME

The radome is an air supported truncated sphere 60 feet in diameter and 37.5 feet high and is shown in Figure 3.1.

#### 3.1 Radome Construction

The basic material used in the construction of the radome was a white vinyl coated nylon fabric weighing approximately 29 ounces per square yard. Gore construction was used and the gores are tied together and reinforced at the top by a pole cap. A crown plate was placed at the pole which will withstand a downward force of 500 pounds. A provision was made for the installation of an eye ring in this plate so that a small hoist can be installed for handling small pieces of equipment.

A 1/2 inch braided nylon rope is bonded to the radome material around the bottom of the radome. The radome is attached to the pad by bolting the material between a metal plate, which is set into the concrete, and a piece of channel stock with the rope below the bolt line. This is shown in Drawing #SK 1946 in Appendix A. An extra piece of material was bonded to the exterior surface of the radome at the bottom which protects the attachment area from weathering.

Since the radome is to be used in the performance of radar cross section measurements, discontinuities in the radome surface were carefully avoided. All blowers and associated equipment were placed underground. There are no doors in the radome and entrance is gained by a stairwell in the floor leading from the underground air lock. The crown plate was made from a dielectric material as were the two exhaust ports in the side of the radome.

#### 3.2 Radome Operation

The radome is an air-supported structure requiring a certain minimum internal pressure in order to remain erect. The pressurization system consists of two centrifugal backward-blade blowers whose operation is controlled manually and/or automatically. A picture of this system is shown in Figure 3.2. Blower No. 1 is a high-volume, low-pressure blower designed to run continuously and is the larger of the two blowers. The blower motor is rated at 5 hp and requires 60 cps 220 V single-phase power. An On-Off switch and



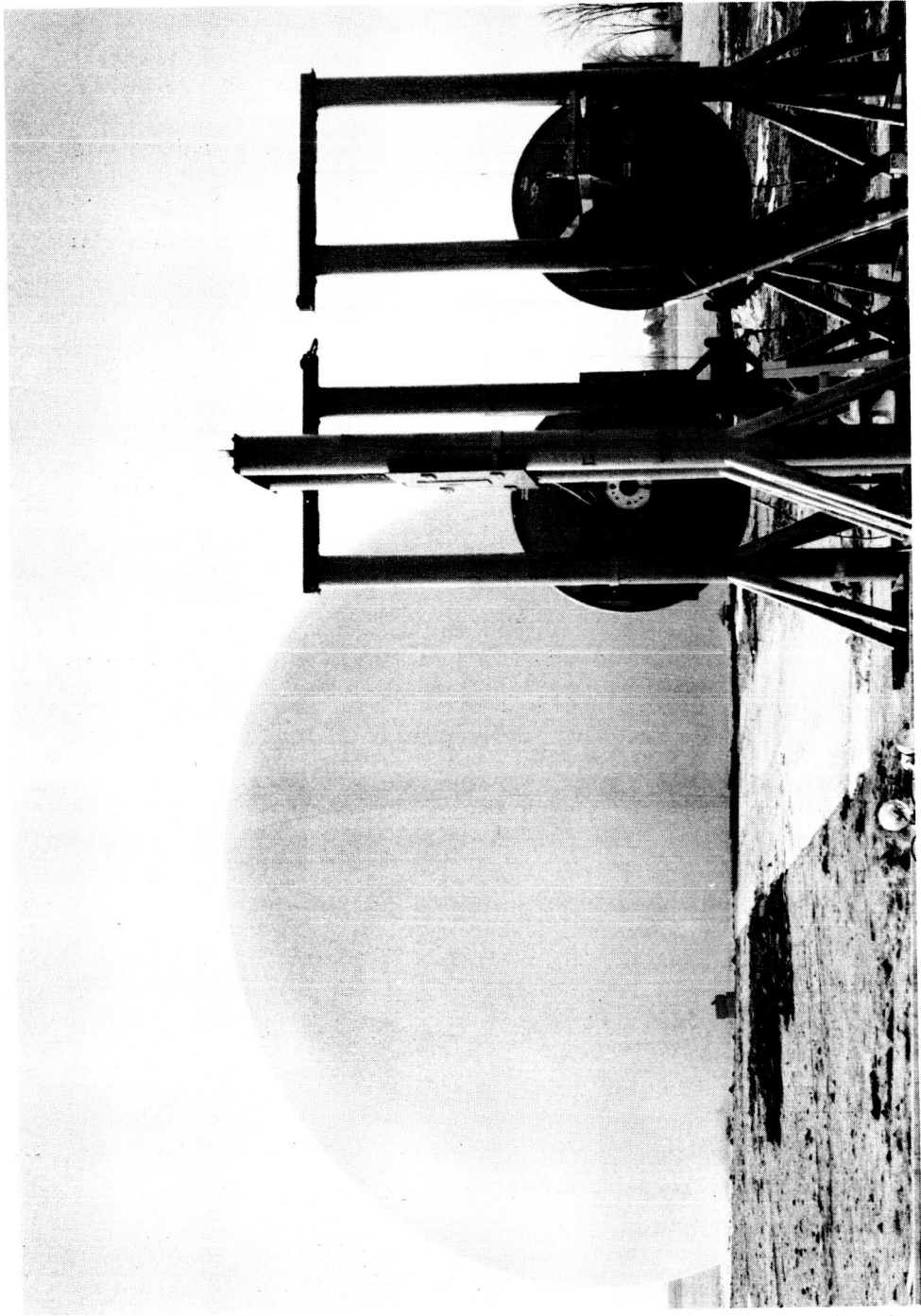


Figure 3.1 Radome



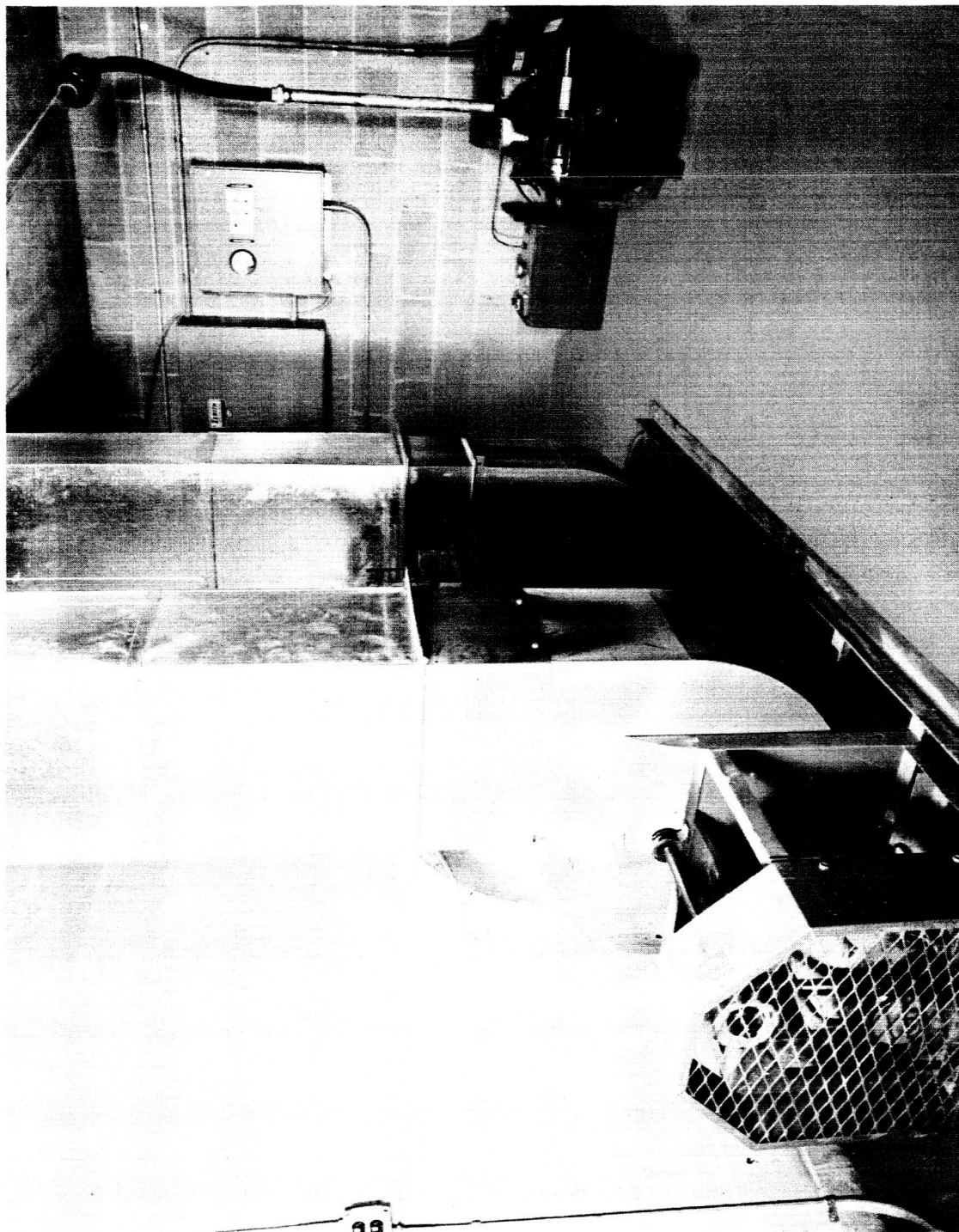


Figure 3.2 Blower System

indicating light on the control panel are connected through a magnetic starter to this blower. Normal operating pressure, with this blower alone, should be approximately 2.5 inches of water.

The smaller blower is used for higher pressure or when additional air flow is required. Normally, higher pressures are required only when the wind is between 70 and 100 mph. Additional air flow is required only for initial erection of the radome or for abnormal loss of air due to large area venting for greater circulation of air. The blower motor is rated at 2 hp and requires 60 cps 220 V single-phase power. This blower is controlled through a three-position switch, AUTO ON, MAN ON, and OFF or RESET, mounted on the control panel. The blower installation is shown in detail in Drawing #SK 1938 in Appendix A.

For normal operation the switch for Blower No. 1 is left in the ON position. The blower will run continuously providing an operating pressure of approximately 2.5 inches of water which is sufficient for wind speeds up to 70 mph. The switch for Blower No. 2 is set to the AUTO ON position. (See Figure 3.3 for guide to operating pressures.)

If at any time, with main power ON, the pressure level in the radome drops to 1.5 inches of water, the pressure switch will turn on the warning and, after a 20 second delay, start Blower No. 2 which will continue to run until the switch is turned to the OFF or RESET position. If the winds exceed 70 mph, or gusts are sufficient to cause the envelope to distort, the pressure is raised. It is then necessary to manually switch on Blower No. 2. The exact pressure level required for any given wind velocity is shown in Figure 3.3. However, it is not absolutely necessary to know the exact velocity as the basic reason for the increased pressures is to prevent radome distortion or whipping, and this condition is readily visible.

The structural stability of the radome is dependent upon a continual source of blower power. An emergency motor-generator has been installed which will supply blower power in the event of a line power failure. The generator is a single phase Kohler Model #10RM61 and will supply 44 amps at 230 V at 60 cps. If line power is lost, the motor-generator is automatically started and

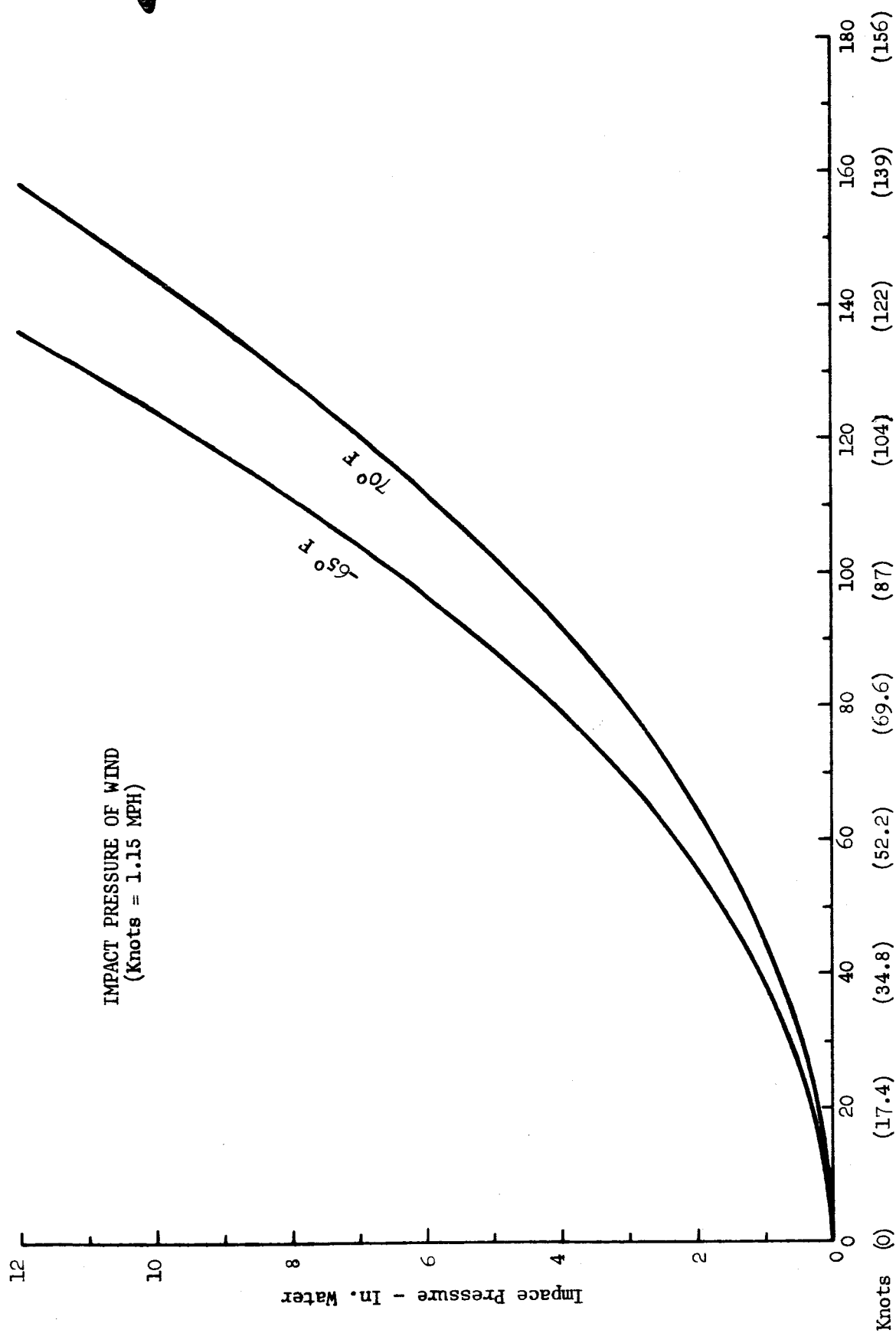


Figure 3.3 Operating Pressure as a Function of Wind Velocity

supplies power to the high pressure blower. When line power is restored the motor-generator automatically shuts off. The emergency system is equipped with an exercising unit so that the equipment can be exercised periodically. This is a device for automatically turning the system on, allowing it to run for a predetermined period of time, and automatically shutting the system off. The number of exercise periods per week can be varied; Conduccion exercises the system at least twice each week.

In the winter it is necessary to take certain additional precautions to insure that there not be an excessive build up of ice and snow. Due to the spherical design of the radome, snow will not usually accumulate on the structure. However, in the case of wet snow, some accumulation might occur which would cause a distortion of the radome surface. In order to prevent this, a Shafconaire Model SC-350 horizontal oil-fired furnace which produces 350,000 btu per hour output has been installed. A picture of this furnace is shown in Figure 3.4. The main furnace unit is 96 inches long by 39 inches wide by 32 inches high and it is mounted on an angle bracket skid approximately 8 inches high. Both the cold air return and the heater inlet duct are 28.5 inches by 36 inches. Warm air is forced into the radome by means of a 1 hp blower motor. A 500 gallon underground oil tank has been provided to supply fuel for the furnace which consumes approximately 3 gallons of fuel oil per hour. Since the furnace is used primarily for ice and snow removal, the amount of underground oil storage is adequate. If the furnace were to be used to provide a warm working environment it would be advisable to install a tank with greater capacity. The furnace is exhausted through a Transite exhaust duct which is equipped with a draft-inducing fan to assist in ventilation.

### 3.3 Radome Erection

The radome arrived at Conduccion folded into a compact package for shipment and ease of handling. A Birdair engineer, Mr. Charles Hoff, was present to assist during the erection procedure. The erection took place on a relatively calm day when the winds were less than 10 miles per hour. A crew of seven men and a portable boom crane were necessary to complete the erection. The entire operation was completed in less than 4 hours.

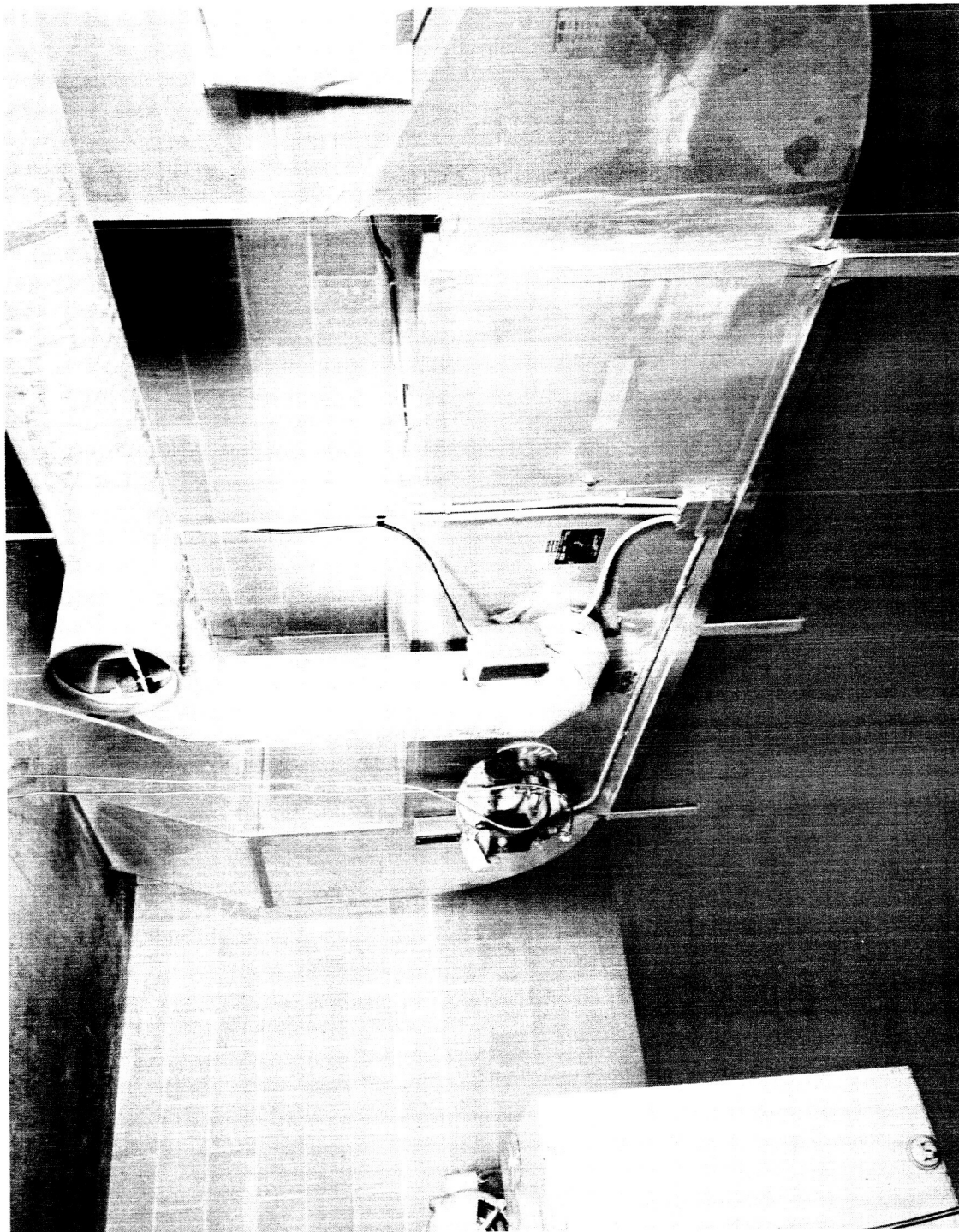


Figure 3.4 Furnace System

The folded radome package was placed near the center of the radome pad and the radome was unfolded toward the edges of the pad. A line was attached from the overhead crane to an eye bolt in the crown plate of the radome. The crane lifted the center of the radome off the pad to allow personnel access to the underside of the radome to make the attachments between the radome pad and the radome. As discussed in Section 3.1 above, the attachment is made by bolting the radome material between an anchor plate set into the concrete curb- ing and the channel clamp ring. The attachment hardware is shown in Drawing #SK 1946 of Appendix A. The channel clamp ring is first put in place and the nuts installed finger tight. The material was then straightened and smoothed and the nuts tightened securely.

When all 16 channel clamp rings were in place the blower system was turned on and the radome was slowly inflated. When power was first supplied to the blower system the Low Pressure Warning Light came on. The switch for Blower No. 1 was turned to the ON position and the switch for Blower No. 2 was turned to the AUTO ON position to provide maximum delivery of air for inflation. As soon as the Low Pressure Warning Light went out, the switch on Blower No. 2 was turned to the OFF position. This prevented over-pressuriza- tion of the radome until the anchorage and attachments were secured. The radome was then inspected for leaks and fabric alignment. The structure was tight and no problems were encountered.

#### 3.4 Electrical Evaluation

This section will present both the theoretical and experimental evalua- tion of the radome. Particular attention has been given to the electrical properties of the radome and their relative effects on the measurements of large (22 foot diameter) segments of reflecting material. The theoretical effort was devoted primarily to the discovery of factors which could cause measurement error. The experimental effort was devoted to evaluating these factors and establishing practical limitations on the type of measurements which can be performed. In addition, attention has been given to using the radome for housing a transmitting antenna. The results indicate that no major problems will be encountered; however, an adequate evaluation of the

radome for this purpose requires a different series of tests than those performed under this program.

#### 3.4.1 Reflection Coefficients

Prior to the purchase of the radome, reflection coefficients were calculated for two different radome samples (A & B) supplied by Birdair Structures, Inc. of Buffalo, New York. Several experiments were conducted on these samples at the Conductron Corporation Radar Range, to provide the information necessary to compute the reflection coefficient. The 6 inch by 6 inch samples of flexible radome material were attached to flat, relatively thick, slabs of polystyrene foam (styrofoam). This was necessary to offer the support needed to maintain the sample as true as possible for controlled test conditions.

The tape (Scotch Brand #810) used to attach the sample to the styrofoam was applied very smoothly, and it would appear that the combination is accurately modeled by two parallel dielectric sheets in air. A theoretical analysis of the measurement program is shown below.

We will first assume that both materials are non-conducting. In this case, Maxwell's equations may be written

$$\begin{aligned}\nabla \times \vec{E} &= -\frac{1}{c} \frac{\partial \vec{B}}{\partial t} & \nabla \cdot \vec{D} &= 0 \\ \nabla \times \vec{H} &= \frac{1}{c} \frac{\partial \vec{D}}{\partial t} & \nabla \cdot \vec{B} &= 0\end{aligned}$$

If the incident field is normal to the interfaces, the fields in all of the regions in Figure 3.5 take the form

$$E_z = A e^{ikx} + A_1 e^{-ikx}$$

and

$$H_y = -\frac{c}{\omega \mu} k (A e^{ikx} - A_1 e^{-ikx})$$

where we assume that  $\mu = 1$  for all materials.

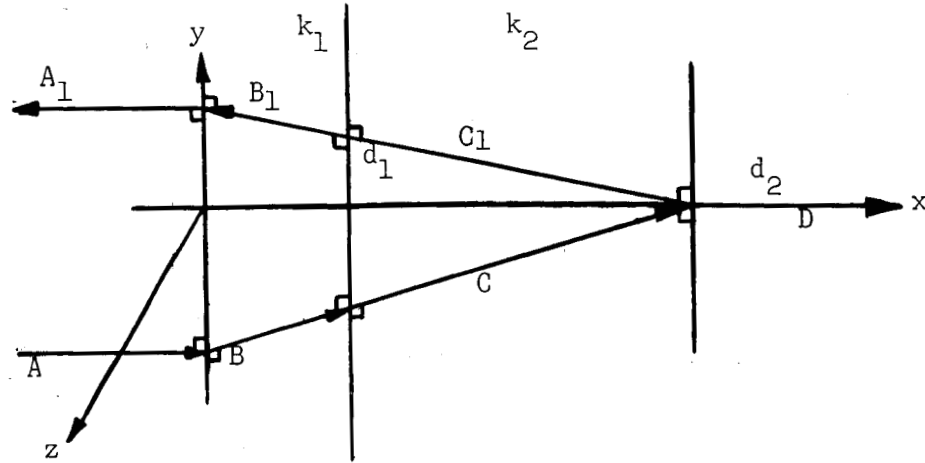


Figure 3.5

### Geometry for Analysis of Two Parallel Dielectric Sheets

Since the tangential components of  $\vec{E}$  and  $\vec{H}$  must be continuous across the interfaces,  $A_1$ ,  $B$ ,  $B_1$ ,  $C$ ,  $C_1$  and  $D$  can be found by solving the six independent equations represented by

$A_1$	$B$	$B_1$	$C$	$C_1$	$D$	$A$
1	-1	-1				-1
-1	$-\eta_1$	$\eta_1$				-1
	$\gamma_{11}$	$1/\gamma_{11}$	$-\gamma_{21}$	$-1/\gamma_{21}$		0
	$\eta_1 \gamma_{11}$	$-\eta_1/\gamma_{11}$	$-\eta_2 \gamma_{21}$	$\eta_2/\gamma_{21}$		0
			$\gamma_{22}$	$1/\gamma_{22}$	$-\gamma_{02}$	0
			$\eta_2 \gamma_{22}$	$-\eta_2/\gamma_{22}$	$-\gamma_{02}$	0

where  $k_1 = \eta_1 k$ ,  $k_2 = \eta_2 k$ ,  $\gamma_{11} = e^{ik_1 d_1}$ ,  $\gamma_{21} = e^{ik_2 d_1}$ ,  $\gamma_{22} = e^{ik_2 d_2}$ , and

$$\gamma_{02} = e^{ikd_2}.$$



If we introduce  $r_1 = \frac{1 - \eta_1}{1 + \eta_1}$  and  $r_2 = \frac{1 - \eta_2}{1 + \eta_2}$ ,

the reflection coefficient of any two layers of dielectric in air is,

$$R_{12} = |A_1|^2$$

$$= \left| \frac{\left\{ \eta_1 \left(1 + \frac{1}{\gamma^2} r_1\right) \left(1 - \frac{\gamma_{22}^2}{\gamma_{21}^2} r_2\right) - \eta_2 \left(1 - \frac{1}{\gamma_{11}^2} r_1\right) \left(1 + \frac{\gamma_{22}^2}{\gamma_{21}^2} r_2\right) \right\}}{\left\{ \eta_1 \left(1 + \frac{1}{\gamma^2} r_1\right) \left(1 - \frac{\gamma_{22}^2}{\gamma_{21}^2} r_2\right) + \eta_2 \left(1 - \frac{1}{\gamma_{11}^2} r_1\right) \left(1 + \frac{\gamma_{22}^2}{\gamma_{21}^2} r_2\right) \right\}} \right|^2$$

The subscript on R indicates that the field strikes the material having propagation constant  $k_1$  first. When the layers are reversed so that the field strikes material 2 first, the same formal result is true if the various parameters are permuted appropriately. In particular as,

$$R_{12} \longrightarrow R_{21}; \gamma_{11} \longrightarrow \gamma'_{11} = \gamma_{22}/\gamma_{21}, \gamma_{21} \longrightarrow \gamma'_{21} = \gamma_{12}/\gamma_{11}$$

$$\gamma_{02} \longrightarrow \gamma'_{22} = \gamma_{12} \text{ and } \gamma_{02} \longrightarrow \gamma'_{02} = \gamma_{02}$$

while

$$d_1 \longrightarrow d'_1 = d_2 - d_1, d_2 \longrightarrow d'_2 = d_2,$$

as

$$\eta_1 \longrightarrow \eta_2 \text{ and } \eta_2 \longrightarrow \eta_1$$

The reflection coefficient is now,

$$R_{21} = \left| \frac{\left\{ -\eta_1 (1 + \gamma_{11}^2 r_1) \left(1 - \frac{\gamma_{21}^2}{\gamma_{22}^2} r_2\right) + \eta_2 (1 - \gamma_{11}^2 r_1) \left(1 + \frac{\gamma_{21}^2}{\gamma_{22}^2} r_2\right) \right\}}{\left\{ \eta_1 (1 + \gamma_{11}^2 r_1) \left(1 - \frac{\gamma_{21}^2}{\gamma_{22}^2} r_2\right) + \eta_2 (1 - \gamma_{11}^2 r_1) \left(1 + \frac{\gamma_{22}^2}{\gamma_{21}^2} r_2\right) \right\}} \right|^2$$

We note that the denominators of  $R_{12}$  and  $R_{21}$  are the same and that the numerators are just negative complex conjugates of each other. Therefore, the power reflection coefficient is independent of whether the sample or support faces the transmitter if both are dielectrics.

If the measured values of  $R_{12}$  and  $R_{21}$  are different, this must be attributed to either experimental error or to non-zero conductivity.

Measurements were made on both samples A and B at 5.45 kmc. Each sample was .05 cm thick, while the supporting material was 2.54 cm thick.

From the experimental data:

	$\sigma_{12}^A = \sigma_{\text{cond.}}$	$R_{12}^A = 1.54 \times 10^{-3} \text{ m}^2$
<u>Sample A</u>	$\sigma_{21}^A = \sigma_{\text{cond.}}$	$R_{21}^A = 2.44 \times 10^{-3} \text{ m}^2$
	$\sigma_{12}^B = \sigma_{\text{cond.}}$	$R_{12}^B = 2.15 \times 10^{-3} \text{ m}^2$
<u>Sample B</u>	$\sigma_{21}^B = \sigma_{\text{cond.}}$	$R_{21}^B = 3.77 \times 10^{-3} \text{ m}^2$

The cross section,  $\sigma_{\text{cond.}}$  of a 6 inch x 6 inch plate is

$$\sigma_{\text{cond.}} = \frac{4\pi}{\lambda} A^2 = 2.23 \text{ m}^2.$$

So, the reflection coefficients are bounded by,

$$\begin{aligned} 0.69 \times 10^{-3} &\leq R_A \leq 1.09 \times 10^{-3} \\ 0.96 \times 10^{-3} &\leq R_B \leq 1.69 \times 10^{-3} \end{aligned}$$

The averages are

$$\bar{R}_A = 0.89 \times 10^{-3}$$

$$\bar{R}_B = 1.32 \times 10^{-3}$$

The reflection coefficients  $R_{12}$  or  $R_{21}$  have been evaluated at the experimental frequency of 5.45 kmc and plotted in Figure 3.6 versus the index of refraction of the samples A and B for several values of  $\eta_2$ , the refractive index of the supporting material. According to VonHippel<sup>(1)</sup>

$$\eta_2 = 1.015.$$

We see that Sample A satisfies the experimental data if

$$1.455 \leq \eta_1^A \leq 1.535$$

and similarly for Sample B

$$1.512 \leq \eta_1^B \leq 1.628$$

Corresponding to  $\bar{R}_A$  and  $\bar{R}_B$  we have

$$\eta_1^A = 1.500$$

$$\eta_1^B = 1.575$$

The reflection coefficient of the NASA radome material is easily obtained now that we know its dielectric constant. According to Stratton<sup>(2)</sup>, the reflection coefficient of a dielectric sheet in the air is,

---

(1) VonHippel, A., "Dielectric Materials and Applications", pp. 337.

(2) Stratton, J.A., "Electromagnetic Theory", McGraw-Hill Publications, pp. 514.

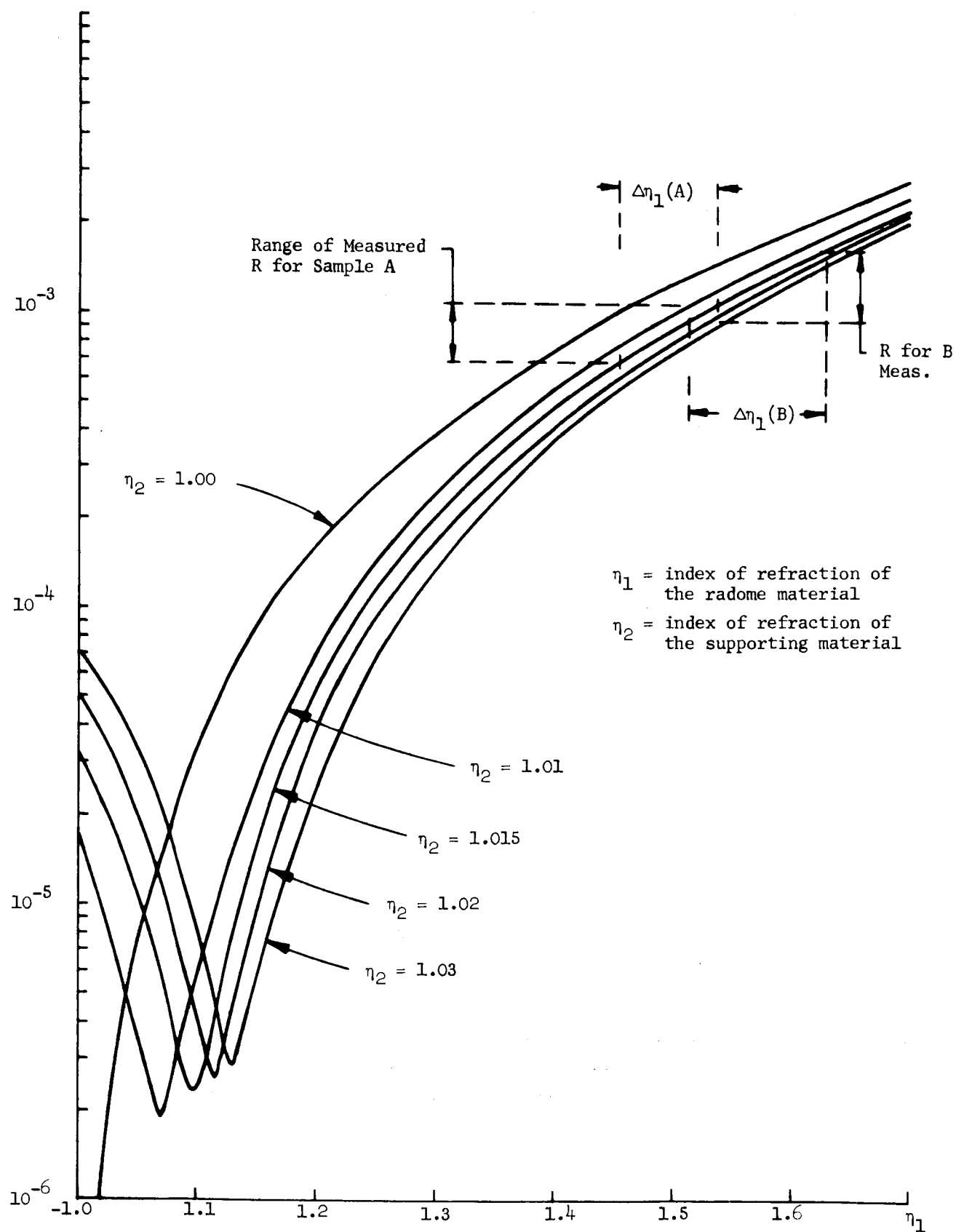


Figure 3.6 Reflection Coefficients of a 2-Layer Dielectric Sandwich

$$R(\lambda)_{\text{radome}} = \frac{4r^2 \sin^2 (\eta_1 k d_1)}{(1 - r^2)^2 + 4r^2 \sin^2 (\eta_1 k d_1)} \approx 4r^2 \sin^2 (\eta_1 k d_1)$$

where

$$r = \frac{1 - \eta_1}{1 + \eta_1}$$

Since the values for  $\eta_1$  determined graphically are only valid at the experimental frequency,  $R(\lambda)_{\text{radome}}$  will only give the general character of the reflection coefficient as a function of frequency. We will evaluate  $R_{\text{radome}}$  from the above (Figure 3.7) for frequencies near the experimental frequency of 5.45 kmc. Note the agreement of  $R(\lambda)_{\text{radome}}$  with  $R_{2\text{-layer}}$  in the limiting case where  $\eta_2 = 1.00$ .

We see that depending on the nature of the difference between  $R_{12}$  and  $R_{21}$ , that the reflection coefficient of the radome materials at 5.45 kmc are,

$$1.0 \times 10^{-3} \leq R_{\text{radome}}^A \leq 1.5 \times 10^{-3}$$

and

$$1.3 \times 10^{-3} \leq R_{\text{radome}}^B \leq 2.35 \times 10^{-3}$$

or

$$\bar{R}_{\text{radome}}^A = 1.25 \times 10^{-3}$$

and

$$\bar{R}_{\text{radome}}^B = 1.75 \times 10^{-3}$$

Using the above reflection coefficients,  $\bar{R}^A$  and  $\bar{R}^B$ , we find that the radar cross section of a radome 60 feet in diameter is

$$\begin{aligned} \sigma_{\text{radome}} &= \bar{R} \pi a^2 = 262.6 \bar{R} \text{ m}^2 \\ &= 3.3 \times 10^{-1} \text{ m}^2 \text{ For Sample A} \\ &= 4.6 \times 10^{-1} \text{ m}^2 \text{ For Sample B} \end{aligned}$$

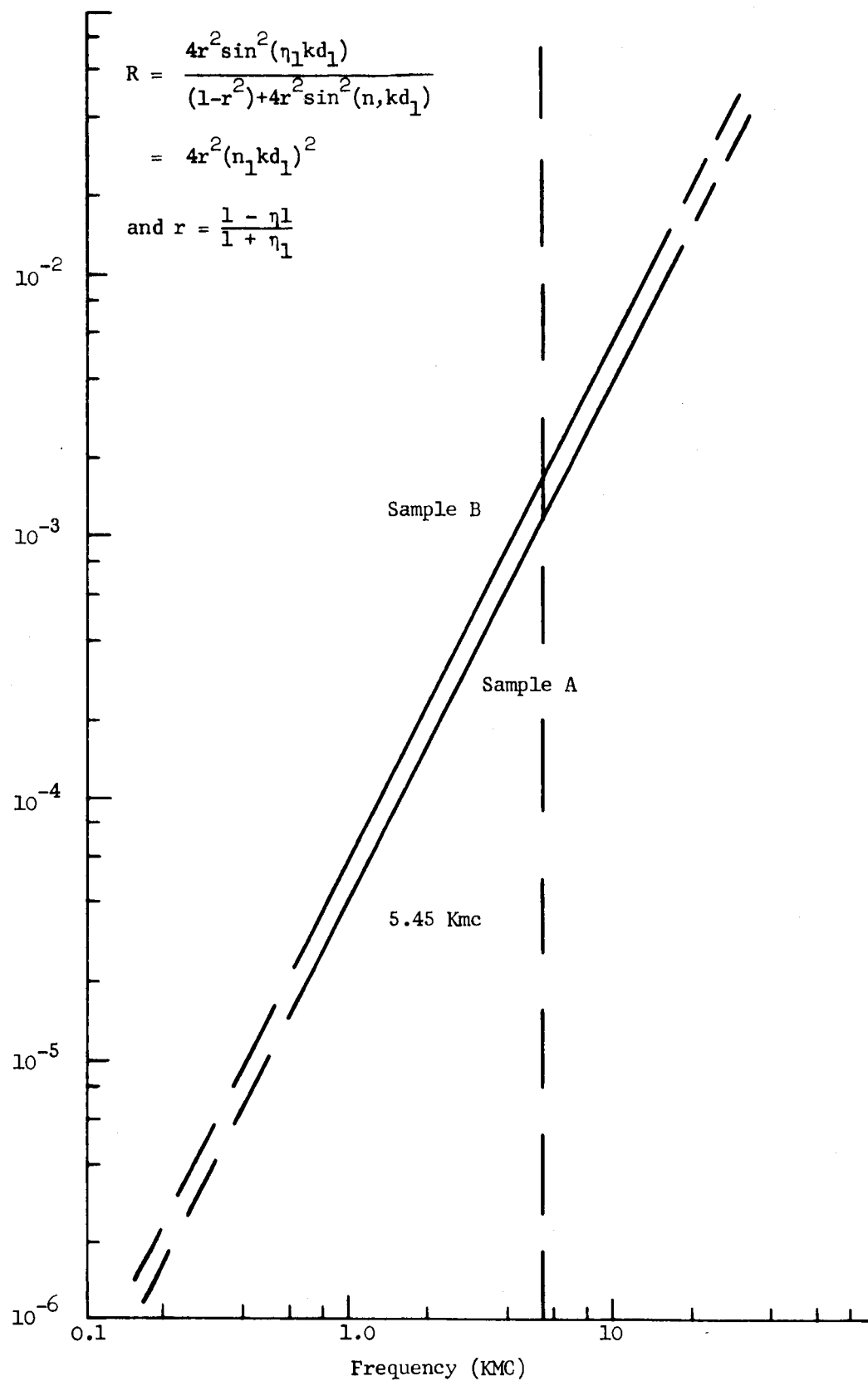


Figure 3.7 Radome Reflection Coefficient Vs. Frequency

The effect on the 2-layer reflection coefficient of assuming that one or both dielectrics have a very slight conductivity can most easily be seen by allowing  $\eta_1$  and  $\eta_2$  to be complex in our expressions for  $R_{12}$  and  $R_{21}$  and expanding around the real part. The complex part of polystyrene foam is small

$$\eta_2 = 1.015 + i 10^{-4}$$

and can in fact be ignored since it cannot account for the observed  $\Delta R$ .

If we set  $\eta_1 = 1.5 + i\eta_1''$  and solve for  $\eta_1'$ , we find that the observed  $\Delta R$  requires  $\eta_1'' = 10^{-2} \eta_1'$ .

Even that value of  $\eta_1''$  cannot greatly effect the radome reflection coefficient which must still lie between the bounds determined earlier, i.e.,

$$10^{-3} \leq R_A \leq 1.4 \times 10^{-3}$$

and

$$1.5 \times 10^{-3} \leq R_B \leq 2.2 \times 10^{-3}.$$

### 3.4.2 Analysis of Radome - Target Interaction Effects

It is clear that in addition to primary reflections from the radome surface, any reflection data obtained on the segment material might be affected by interactions between the radome and the target. In order to evaluate the extent to which such interactions might affect the measurement data, a theoretical analysis was performed and the results are described below. The analysis was concerned with two separate phenomena; first, assuming that a target inside the radome is illuminated with a plane wave, it is necessary to determine the extent to which the far field reflection pattern is distorted by the radome; and second, the effect of multiple reflections must be minimized by correct placement of the target in the radome.

#### 3.4.2.1 High-Frequency Scattering from a Conducting Sphere Surrounded by a Thin-Wall Radome

It is first necessary to investigate the radar cross section distortions produced by a large and spherical thin-wall radome surrounding a perfectly con-

ducting target. In considering this problem it is convenient to confine attention to the specular backscatter generated by a plane electromagnetic wave incident upon the system. In particular, we shall consider the problem of scattering by a perfectly conducting sphere placed at the center of the spherical dielectric housing or radome. Since all boundary surfaces are now concentric spheres, the exact Mie series can be obtained in straight-forward fashion and the high-frequency fields can be evaluated by standard analytical techniques.

Specifying the problem, we have a plane electromagnetic wave

$$\vec{E} = \hat{x} e^{-i\omega t + ikz}, \quad k = \omega (\epsilon_0 \mu_0)^{1/2} \quad (3.1)$$

incident upon a perfectly conducting sphere with radius  $c$  covered by two concentric layers. The outer layer consists of a dielectric with relative electric permittivity  $\epsilon$  and with relative magnetic permeability  $\mu = 1$ . The inside radius of this layer will be denoted by  $b$ , its outside radius by  $a$ , and its thickness by  $\delta = a - b$ . In general, the products  $k\delta$  and  $k_1\delta$ , where  $k_1 = \sqrt{\epsilon}k$  is the propagation constant within the dielectric, will be assumed much smaller than unity. The outer layer, then, represents the thin-wall radome. The inner layer extending from radius  $c$  to radius  $b$  consists of free space. We shall take the free-space constants  $\epsilon_0$  and  $\mu_0$  to be equal to unity. Ordinarily, the inner free-space layer is thick so that  $k(b-c)$  is much larger than one; however, we have no need to use this fact in the calculations.

We shall consider in turn the magnetic field on the surface of the conducting sphere at the backscattering specular point and the far-zone electric field scattered in the back direction. In both cases the exact Mie series are represented as contour integrals by means of the Watson transform technique. The contour integrals are evaluated asymptotically under the following conditions

$$kc, kb \gg 1,$$

$$k\delta, k_1\delta \ll 1$$



to yield the first two terms in the asymptotic series corresponding to a Luneberg-Kline expansion. The creeping wave or diffracted field contribution is not obtained.

Before investigating the exact Mie series representations it is useful to obtain the geometrical-optics fields by means of ray-tracing. This is easily done and the result will act as both a check and a guideline for the complicated expansions to follow.

#### GEOMETRICAL-OPTICS

In the geometrical-optics approximation, the effect of the radome wall is most conveniently represented in terms of transmission and reflection coefficients, these coefficients being calculated by replacing the curved surface of the radome by a plane sheet. For a thin wall and normal incidence, the amplitude reflection and transmission coefficients for the electric and magnetic fields are given by

$$\begin{aligned} R_H &= -R_E = \frac{k\delta}{2i} (\epsilon-1) + O(k\delta)^2, \\ T_H &= T_E = 1 - \frac{k\delta}{2i} (\epsilon-1) + O(k\delta)^2. \end{aligned} \quad (3.2)$$

In all of our calculations we shall keep only the first order in  $k\delta$  and hence only the first order in the reflection coefficient.

At the specular point ( $x=0$ ,  $y=0$ ,  $z=-c$ ) on the surface of the metal sphere, the magnetic field is, by geometrical optics,

$$H_y^{\text{surf}} = 2 T_H e^{-ikc} + 2 T_H R_H \left(\frac{b}{3b-2c}\right) e^{-ikc} e^{2ik(b-c)}, \quad (3.3)$$

where the second term corresponds to a double bounce in the free-space layer. Higher order multiple bounces introduce higher powers of the reflection coefficient and are neglected. Introducing (3.2) into (3.3) we have explicitly

$$H_y^{\text{surf}} = 2e^{-ikc} \left\{ \left[ 1 - \frac{k\delta}{2i} (\epsilon-1) \right] + \frac{k\delta}{2i} (\epsilon-1) \left(\frac{b}{3b-2c}\right) e^{2ik(b-c)} \right\} \quad (3.4)$$

Similarly, the far backscattered electric field in the optics approximation is

$$\begin{aligned}
E_x^{bs} = & -T_E^2 \left(\frac{c}{2r}\right) e^{ik(r-2c)} + R_E \left(\frac{b}{2r}\right) e^{ik(r-2b)} \\
& + T_E^2 R_E \left(\frac{c}{2r} \frac{b}{2b-c}\right) e^{ik(r-2c)} e^{2ik(b-c)},
\end{aligned}
\tag{3.5}$$

or, in explicit form, we have

$$\begin{aligned}
E_x^{bs} = & -\frac{c}{2r} e^{ik(r-2c)} \left\{ \left[ 1 - 2 \frac{k\delta}{2i} (\epsilon-1) \right] + \frac{k\delta}{2i} (\epsilon-1) \left(\frac{b}{2b-c}\right) e^{2ik(b-c)} \right. \\
& \left. + \frac{k\delta}{2i} (\epsilon-1) \left(\frac{b}{c}\right) e^{-2ik(b-c)} \right\}.
\end{aligned}
\tag{3.6}$$

Equations (3.4) and (3.6) represent the expected first order terms in a Luneberg-Kline expansion. To obtain higher order terms we turn to the exact Mie series representation.

#### FIELD ON THE CONDUCTING SPHERE

After much algebra the electromagnetic field on the surface of the conducting sphere is found to be

$$\begin{aligned}
H_\theta = & -\frac{4 \sin\varphi}{ikc} \sum_{n=1}^{\infty} i^n \frac{2n+1}{n(n+1)} \left\{ \frac{1}{ia'_n} \frac{\partial}{\partial\theta} - \frac{1}{b'_n} \frac{1}{\sin\theta} \right\} P_n^1(\cos\theta), \\
H_\varphi = & -\frac{4 \cos\varphi}{ikc} \sum_{n=1}^{\infty} i^n \frac{2n+1}{n(n+1)} \left\{ \frac{1}{ia'_n} \frac{1}{\sin\theta} - \frac{1}{b'_n} \frac{\partial}{\partial\theta} \right\} P_n^1(\cos\theta), \\
E_r = & -\frac{4 \cos\varphi}{(kc)^2} \sum_{n=1}^{\infty} i^n (2n+1) \frac{P_n^1(\cos\theta)}{b'_n},
\end{aligned}
\tag{3.7}$$

where

$$\begin{aligned}
a'_n = & h_n^{(1)}(ka) \left[ \sqrt{\frac{\epsilon}{\mu}} \frac{\partial^2 c_n}{\partial(k_1 b) \partial(k_1 a)} c'_n - \frac{\partial c_n}{\partial(k_1 a)} \frac{\partial c'_n}{\partial(kb)} \right] \\
& - h_n^{(1)}(ka) \left[ \frac{\partial c_n}{\partial(k_1 b)} c'_n - \sqrt{\frac{\mu}{\epsilon}} \frac{\partial c'_n}{\partial(kb)} c_n \right]
\end{aligned}
\tag{3.8}$$

and where  $b'_n$  is obtained from  $a'_n$  by replacing  $C'_n$  with  $\partial C'_n / \partial(kc)$  and by interchanging  $\epsilon$  and  $\mu$ . In the above

$$C_n = h_n^{(1)}(k_1 a) h_n^{(2)}(k_1 b) - h_n^{(1)}(k_1 b) h_n^{(2)}(k_1 a), \quad (3.9)$$

$$C'_n = h_n^{(1)}(kb) h_n^{(2)}(kc) - h_n^{(1)}(kc) h_n^{(2)}(kb),$$

and the spherical Hankel functions are given by

$$h_n^{(1)(2)}(x) = \sqrt{\pi x/2} H_{\nu}^{(1)(2)}(x)$$

with  $\nu = n + 1/2$ .

Setting  $a = b + \delta$  we now expand those Hankel functions which are functions of  $ka$  or  $k_1 a$  into Taylor series, thus e.g.

$$h_n^{(1)(2)}(ka) = h_n^{(1)(2)}(kb) + (k\delta) h'_n{}^{(1)(2)}(kb) + \dots,$$

and we find, by making use of the Wronskian relation

$$h'_n{}^{(1)} h_n^{(2)} - h_n^{(1)} h'_n{}^{(2)} = 2i,$$

that

$$C_n = 2i (k_1 \delta), \quad \frac{\partial C_n}{\partial(k_1 a)} = - \frac{\partial C_n}{\partial(k_1 b)} = 2i,$$

$$\frac{\partial^2 C_n}{\partial(k_1 b) \partial(k_1 a)} = 2i (k_1 \delta) \left[ 1 - \frac{n(n+1)}{(k_1 b)^2} \right].$$

Terms of order  $(k_1 \delta)^2$  have been neglected. Employing the immediately preceding equations and recalling that  $\mu = 1$ , we find that  $a'_n$  and  $b'_n$  take the form

$$a_n' = 4 h_n^{(1)}(kc) A_n' , \quad (3.10)$$

$$b_n' = 4 h_n^{(1)}(kc) B_n' ,$$

where

$$A_n' = 1 - \frac{k\delta}{2i} (\epsilon-1) \frac{h_n^{(1)}(kb)}{h_n^{(1)}(kc)} C_n' , \quad (3.11)$$

$$B_n' = 1 - \frac{k\delta}{2i} (\epsilon-1) \frac{h_n^{(1)}(kb)}{h_n^{(1)}(kc)} \frac{\partial^2 C_n'}{\partial(kb)\partial(kc)} - \frac{k\delta}{2i} \left(1 - \frac{1}{\epsilon}\right) \frac{h_n^{(1)}(kb)}{h_n^{(1)}(kc)} \frac{\partial C_n'}{\partial(kc)} \frac{n(n+1)}{(kb)^2} .$$

At the backscattering specular point,  $\theta = \pi$  and

$$\frac{P_n^1}{\sin\theta} \rightarrow (-)^n \frac{n(n+1)}{2} , \quad \frac{\partial P_n^1}{\partial\theta} \rightarrow -(-)^n \frac{n(n+1)}{2} ;$$

hence at this point the only non-zero component of the electromagnetic field is

$$H_y = - \frac{1}{2ikc} \sum_{n=1}^{\infty} (-i)^n (2n+1) \left\{ \frac{1}{i h_n^{(1)}(kc) A_n'} + \frac{1}{h_n^{(1)}(kc) B_n'} \right\} . \quad (3.12)$$

To effect a high-frequency asymptotic evaluation, we convert the summation over  $n$  into a contour integral: define

$$f(v) = \frac{1}{i h_n^{(1)}(kc) A_n'} + \frac{1}{h_n^{(1)}(kc) B_n'} \quad (3.13)$$

with  $v = n + 1/2$ , then

$$H_y = \frac{1}{2kc} \left\{ \frac{1}{i} f\left(\frac{1}{2}\right) + e^{-i\frac{\pi}{4}} \int_0^{\infty} \frac{dv v}{\cos v\pi} e^{i\frac{v\pi}{2}} f(v) \right\} . \quad (3.14)$$

The contour  $C$ , which encircles the positive real axis in a clockwise fashion, can be deformed into the path  $C'$  passing from the fourth quadrant through the origin to the second quadrant. Any poles of the integrand which are captured by this contour deformation contribute to the diffracted field and are not of interest here.

It is an easy matter to show that the factor  $A'_n$  in the denominator in (3.13) has no zeros on the real  $v$  axis. From (3.11),

$$A'_n = 1 - \frac{k\delta}{2i} (\epsilon - 1) \frac{h_n^{(1)}(kb)}{h_n^{(1)}(kc)} C'_n$$

where

$$\begin{aligned} C'_n &= h_n^{(1)}(kb) h_n^{(2)}(kc) - h_n^{(1)}(kc) h_n^{(2)}(kb) \\ &= 2i \{j_n(kc) y_n(kb) - j_n(kb) y_n(kc)\} . \end{aligned}$$

Thus  $C'_n$  is pure imaginary for real  $n$ . In order for  $A'_n$  to be zero, the ratio  $h_n^{(1)}(kb)/h_n^{(1)}(kc)$  must therefore be real, so we must have

$$\text{Im} \frac{h_n^{(1)}(kb)}{h_n^{(1)}(kc)} = \frac{j_n(kc) y_n(kb) - j_n(kb) y_n(kc)}{j_n^2(kc) + y_n^2(kc)} = 0 .$$

But if this is true, then  $C'_n$  is zero. Therefore  $A'_n$  has no zeros on the real  $v$  axis. Similar, but more complicated, considerations apply to  $B'_n$ . Thus on the real  $v$  axis the integrand in (3.14) possesses poles only at the zeros of  $\cos v\pi$ .

The line integral over  $C'$  can be evaluated asymptotically at the stationary point  $v = 0$  following the technique of Scott<sup>(3)</sup>. Using the asymptotic approximations ( $x$  being large)

---

(3) Scott, J. M. C., A.E.C. Research Est. Rpt. T/M 30 (1949).

$$h_n^{(1)}(x) \sim \exp \left( ix - \frac{iv\pi}{2} + \frac{iv^2}{2x} - \frac{i\pi}{4} \right) \left\{ 1 - \frac{i}{8x} + \frac{1}{4} \frac{v^2}{x^2} + \frac{iv^4}{24x^3} + \dots \right\},$$

$$h_n^{(2)}(x) \sim \exp \left( -ix + \frac{iv\pi}{2} - \frac{iv^2}{2x} + \frac{i\pi}{4} \right) \left\{ 1 + \frac{i}{8x} + \frac{1}{4} \frac{v^2}{x^2} - \frac{iv^4}{24x^3} + \dots \right\},$$

we obtain the following expansion for  $f(v)$

$$\begin{aligned} f(v) \sim & \frac{1}{i} \exp \left( -ikc + \frac{iv\pi}{2} - \frac{iv^2}{2kc} + \frac{i\pi}{4} \right) \left\{ 2 + \frac{i}{4kc} - \frac{iv^4}{12(kc)^3} \right\} \left\{ 1 - \frac{k\delta}{2i} (\epsilon-1) \right\} \\ & - \frac{1}{i} \frac{k\delta}{2i} \left( 1 - \frac{1}{\epsilon} \right) \exp \left( -ikc + \frac{iv\pi}{2} - \frac{iv^2}{2kc} + \frac{i\pi}{4} \right) \left\{ \frac{v^2}{(kb)^2} \right\} \\ & + \frac{1}{i} \frac{k\delta}{2i} (\epsilon-1) \exp \left[ ik(2b-3c) + \frac{iv\pi}{2} + \frac{iv^2}{k} \left( \frac{1}{b} - \frac{3}{2c} \right) + \frac{i\pi}{4} \right] \left\{ 2 - \frac{i}{2k} \left( \frac{1}{b} - \frac{3}{2c} \right) + \right. \\ & \left. + \frac{iv^4}{6k^3} \left( \frac{1}{b^3} - \frac{3}{2c^3} \right) \right\} - \frac{1}{i} \frac{k\delta}{2i} \left( 1 - \frac{1}{\epsilon} \right) \exp \left[ ik(2b-3c) + \frac{iv\pi}{2} + \frac{iv^3}{k} \left( \frac{1}{b} - \frac{3}{2c} \right) + \frac{i\pi}{2} \right] \\ & \left\{ \frac{v^2}{(kb)^2} \right\}. \end{aligned} \quad (3.15)$$

We also note the exact identity

$$f\left(\frac{1}{2}\right) = 2e^{-ikc} \left\{ 1 + \frac{k\delta}{2i} (\epsilon-1) \left[ e^{2ik(b-c)} - 1 \right] \right\}. \quad (3.16)$$

When (3.15) is substituted into (3.14) the resulting line integral is of the form considered by Scott<sup>(4)</sup>. The combination of the asymptotic expression for the line integral and the term involving  $f(1/2)$  in the expression (3.14) gives the Luneberg-Kline contribution to the surface field. We obtain

---

(4) Scott, Ibid.

$$\begin{aligned}
 H_y^{\text{surf}} \sim & 2e^{-ikc} \left\{ \left[ 1 - \frac{k\delta}{2i} (\epsilon-1) \right] - \frac{1}{ikc} \frac{k\delta}{2i} \left( 1 - \frac{1}{\epsilon} \right) \frac{c^2}{b^2} \right\} \\
 & + 2e^{ik(2b-3c)} \left\{ \frac{k\delta}{2i} (\epsilon-1) \left( \frac{b}{3b-2c} \right) + \frac{1}{3ikc} \frac{k\delta}{2i} (\epsilon-1) \left[ 1 - \frac{3b^3-2c^3}{(3b-2c)^3} \right] \right. \\
 & \left. - \frac{1}{ikc} \frac{k\delta}{2i} \left( 1 - \frac{1}{\epsilon} \right) \frac{c^2}{b^2} \left( \frac{b}{3b-2c} \right)^2 \right\}. \quad (3.17)
 \end{aligned}$$

One verifies that the first order term in this expansion agrees with the geometrical-optics expression given in (3.4).

#### THE BACKSCATTERED FIELD

The asymptotic expansion of the backscattered field can be obtained in a fashion analogous with that presented above. One finds that the far back-scattered field may be written in the form

$$\begin{aligned}
 E_x^{\text{bs}} &= \frac{e^{ikr}}{ikr} \sum_{n=1}^{\infty} (-)^n \left( n + \frac{1}{2} \right) \frac{i (A_n - B_n)}{L_v(A_n) L_v(B_n)} \\
 &= - \frac{e^{ikr}}{2kr} \left\{ \frac{A_0 - B_0}{L_{\frac{1}{2}}(A_0) L_{\frac{1}{2}}(B_0)} + \int_C \frac{dv v}{\cos v \pi} \frac{i (A-B)}{L_v(A) L_v(B)} \right\}, \quad (3.18)
 \end{aligned}$$

where

$$L_v(A_n) = h_n^{(1)}(ka) A_n - h_n'^{(1)}(ka) \quad (3.19)$$

and similarly for  $L_v(B_n)$ . The coefficients  $A_n$  and  $B_n$  are given by Bowman <sup>(5)</sup> in connection with the problem of a doubly absorber-coated sphere. For application to the problem at hand, we simply state that one finds, again after much manipulation, the following expansion to first order in  $(k\delta)$

(5) Bowman, J. J., Conductron Memorandum D0620-177-M, 24 September 1963.

$$\begin{aligned}
\frac{A-B}{L_v(A)L_v(B)} &= \frac{-1}{h_n^{(1)}(kc) h_n'^{(1)}(kc)} \left\{ 1 + \frac{k\delta}{4} (\epsilon-1) \left[ \frac{\partial C_n'}{\partial(kb)} \frac{\partial^2 C_n'}{\partial(kb)\partial(kc)} - C_n' \frac{\partial C_n'}{\partial(kc)} \right] \right. \\
&+ \frac{k\delta}{2i} (\epsilon-1) \left[ \frac{h_n^{(1)}(kb)}{h_n^{(1)}(kc)} C_n' + \frac{h_n'^{(1)}(kb)}{h_n'^{(1)}(kc)} \frac{\partial^2 C_n'}{\partial(kb) \partial(kc)} \right] \\
&\left. + \frac{k\delta}{2i} \left( 1 - \frac{1}{\epsilon} \right) \frac{n(n+1)}{(kb)^2} \left[ \frac{h_n^{(1)}(kb)}{h_n'^{(1)}(kc)} \frac{\partial C_n'}{\partial(kc)} - \frac{C_n'}{2i} \frac{\partial C_n'}{\partial(kc)} \right] \right\}
\end{aligned} \tag{3.20}$$

where  $C_n'$  is defined in Equation (3.9).

To evaluate the line integral in (3.18) asymptotically at the stationary point  $v = 0$  we require the following expansion

$$\frac{A-B}{L_v(A)L_v(B)} \sim -e^{-2ikc + iv\pi} \left\{ \right\}, \tag{3.21}$$

where

$$\begin{aligned}
\left\{ \right\} &= \exp \left( -\frac{iv^2}{kc} \right) \left\{ \left[ 1 + \frac{i}{4kc} - \frac{iv^4}{12(kc)^3} \right] \left[ 1 - 2 \frac{k\delta}{2i} (\epsilon-1) \right] - \frac{k\delta}{2i} \left( 1 - \frac{1}{\epsilon} \right) \left[ \frac{v^2}{(kb)^2} \right] \right\} \\
&+ \exp \left[ -2ik(b-c) - \frac{iv^2}{kb} \right] \left\{ \frac{k\delta}{2i} (\epsilon-1) \left[ 1 + \frac{i}{4kb} - \frac{iv^4}{12(kb)^3} \right] - \frac{k\delta}{4i} \left( 1 - \frac{1}{\epsilon} \right) \left[ \frac{v^2}{(kb)^2} \right] \right\} \\
&+ \exp \left[ 2ik(b-c) + \frac{iv^2}{k} \left( \frac{1}{b} - \frac{2}{c} \right) \right] \left\{ \frac{k\delta}{2i} (\epsilon-1) \left[ 1 - \frac{i}{4k} \left( \frac{1}{b} - \frac{2}{c} \right) + \frac{iv^4}{12k^3} \left( \frac{1}{b^3} - \frac{2}{c^3} \right) \right] \right. \\
&\left. - \frac{k\delta}{4i} \left( 1 - \frac{1}{\epsilon} \right) \left[ \frac{v^2}{(kb)^2} \right] \right\}.
\end{aligned} \tag{3.22}$$



$$\frac{A_o - B_o}{L_{1/2}(A_o) L_{1/2}(B_o)} = \frac{1}{i} e^{-2ikc} \left\{ \left[ 1 - 2 \frac{k\delta}{2i} (\epsilon - 1) \right] + 2 \frac{k\delta}{2i} (\epsilon - 1) \cos 2k(b-c) \right\}. \quad (3.23)$$

When (3.21) and (3.22) are substituted into (3.18) the resulting line integral is again of the form considered by Scott<sup>(6)</sup>. The combination of the asymptotic expression for the line integral and the term given by (3.23) in the expression (3.18) yields the Luneberg-Kline contribution to the back-scattered field, namely

$$\begin{aligned} E_x^{bs} \sim & -\frac{c}{2r} e^{ik(r-2c)} \left\{ \left( 1 + \frac{1}{2ikc} \right) \left[ 1 - 2 \frac{k\delta}{2i} (\epsilon - 1) \right] - \frac{1}{ikc} \frac{k\delta}{2i} \left( 1 - \frac{1}{\epsilon} \right) \frac{c^2}{b^2} \right\} \\ & - \frac{b}{2r} e^{ik(r-2b)} \left\{ \left( 1 + \frac{1}{2ikb} \right) \frac{k\delta}{2i} (\epsilon - 1) - \frac{1}{2ikc} \frac{k\delta}{2i} \left( 1 - \frac{1}{\epsilon} \right) \right\} \\ & - \frac{c}{2r} e^{ik(r+2b-4c)} \left\{ \frac{k\delta}{2i} (\epsilon - 1) \left( \frac{b}{2b-c} \right) + \frac{2}{3ikc} \frac{k\delta}{2i} (\epsilon - 1) \left[ 1 - \frac{1}{4} \frac{2b^3 - c^3}{(2b-c)^3} \right] \right. \\ & \left. - \frac{1}{2ikc} \frac{k\delta}{2i} \left( 1 - \frac{1}{\epsilon} \right) \frac{c^2}{b^2} \left( \frac{b}{2b-c} \right)^2 \right\} \end{aligned} \quad (3.24)$$

The first order term in this expansion agrees with the geometrical-optics expression given in (3.6).

The dominant contribution to the backscattered field arises, of course, from the term

$$-\frac{c}{2r} e^{ik(r-2c)}$$

corresponding to specular reflection from the conducting sphere. The next important contributor to the geometrical-optics field arises from

---

(6) Scott, Ibid.

$$- \frac{b}{2r} \frac{k\delta}{2i} (\epsilon-1) e^{ik(r-2b)}$$

corresponding to reflection from the radome itself. This term is small compared to the leading term provided

$$k\delta(\epsilon-1) \frac{b}{c} \ll 1.$$

#### 3.4.2.2 Target Location

Since no radome material exists which will transmit all frequencies of interest with 100 per cent efficiency, it is necessary to locate the segment where the smallest amount of multiply-reflected energy returns to the radar. To determine this location, considerations were given to the key factors shown below.

##### A. Scattering from the Edges of the Balloon and Mounting Structure

Even though the termination is designed to minimize backscattering, the relatively small radius of curvature here will tend to scatter energy off the roof and floor of the radome. This can be minimized by locating the segment half way between the top and bottom of the radome. The return from this contribution will be approximately,

$$\sigma_I \approx R \frac{\pi a^2 R_o}{4 \sqrt{2} d}$$

where  $2 R_o$  is the diameter of the balloon segment  $2 R_o \approx 22$  feet,  $a$  is the radius of curvature of the termination,  $d$  is distance from termination to radome and  $R$  is reflection coefficient of radome.

##### B. Standing Waves Set up Between Parallel Surfaces

If the segment is located incorrectly it is possible for the surfaces to be parallel and perpendicular to the line joining them. If so, a standing wave will be set up between the surfaces which will be fed by almost any direct source of scattering in the neighborhood.

Equation of Radome:  $R_R^2 = X_R^2 + Y_R^2$

Normal:  $\hat{N}_R = X_R/R_R \hat{X} + Y_R/R_R \hat{Y}$

Equation of Segment:  $R_B^2 = (X_B - X_1)^2 + (Y_B - Y_1)^2$

Normal:  $\hat{N}_B = (X_B - X_1)/R_B \hat{X} + (Y_B - Y_1)/R_B \hat{Y}$

A line passing through the center of curvature of the segment will intersect both segment and radome normally only if it passes through the radome center.

$$\tan \phi_B = Y_1/X_1 \quad (\text{Condition II})$$

The condition in Section A requires  $(X_1, Y_1)$  to be high enough that the lower edge of the segment is approximately at radome center. The above condition II and condition I can be satisfied if the segment is moved forward from the center of the radome but not if the segment is moved backward.

#### C. Focusing

There are two important foci of the radome. The first is due to the reflection of energy off the rear of the radome. This energy will be focused near  $(Y = 0, X = 1/2 R_R)$ . The second focus is at the center of the radome. Scattering from any small discontinuity in the radome or from an object at the center of the radome will be focused here.

If the segment is located at the center or towards the rear, the lower edge of the termination will be in or near one or the other of these foci.

#### D. Backscattering

The condition required for backscattering is that the ray deflected from the balloon surface at an angle  $2\phi_B$  be reflected normally from the radome surface. This occurs when

$$R_B \sin \phi_B + X_1 \sin 2\phi_B - Y_1 \cos 2\phi_B = 0$$

$\phi_B$  is limited by the size of the segment

$$\phi_B - 180 = \frac{S_B}{R_B} = \frac{22'}{67.5'} = 0.163 \text{ rad} = 9.32^\circ$$

In the worst cases  $\phi_B = 180 \pm 9.32$

$$\mp .162 (67.5) \pm X_1 (.320) - Y_1 (.950) = 0$$

and

$$\begin{aligned} Y_1 &= \mp 11.5 \pm .336 X_1 = \pm 6.3' \text{ (If segment is 15' forward)} \\ &= \pm 12.3' \text{ (If segment is at center)} \\ &= \pm 18.3' \text{ (If segment is 15' back)} \end{aligned}$$

In order to avoid backscattering of this type, the center of the balloon segment must be higher than the maximum values given above at each location.

Within conditions I, II, and III, we see that only in the forward position where  $Y_1 \approx 9.5'$  can condition IV be satisfied.

NOTE: at center position  $Y_1 \approx 11'$   
at rear position  $Y_1 \approx 10'$

At the position  $X_B = -10'$  (10 feet forward)  $Y_1$  must be greater than 8.0' to satisfy (IV) at this position, (I) requires  $Y_1 = 10.5'$ .

### 3.4.3 Measurement Considerations

In a CW measurement system of the type which Conductron uses, background contributions can be a serious problem. If an unbalanced system is used, the amplitude of the reflected wave must be sufficiently below the amplitude of the wave scattered from the target to preclude errors due to phase additions and subtractions. If, on the other hand, a balanced system is used, we are less concerned with the background and much more concerned with extent to which the background is modified by the placement of the target in the field.

The results of the theoretical analyses shown above indicate that the level of energy backscattered directly from the radome should be well below

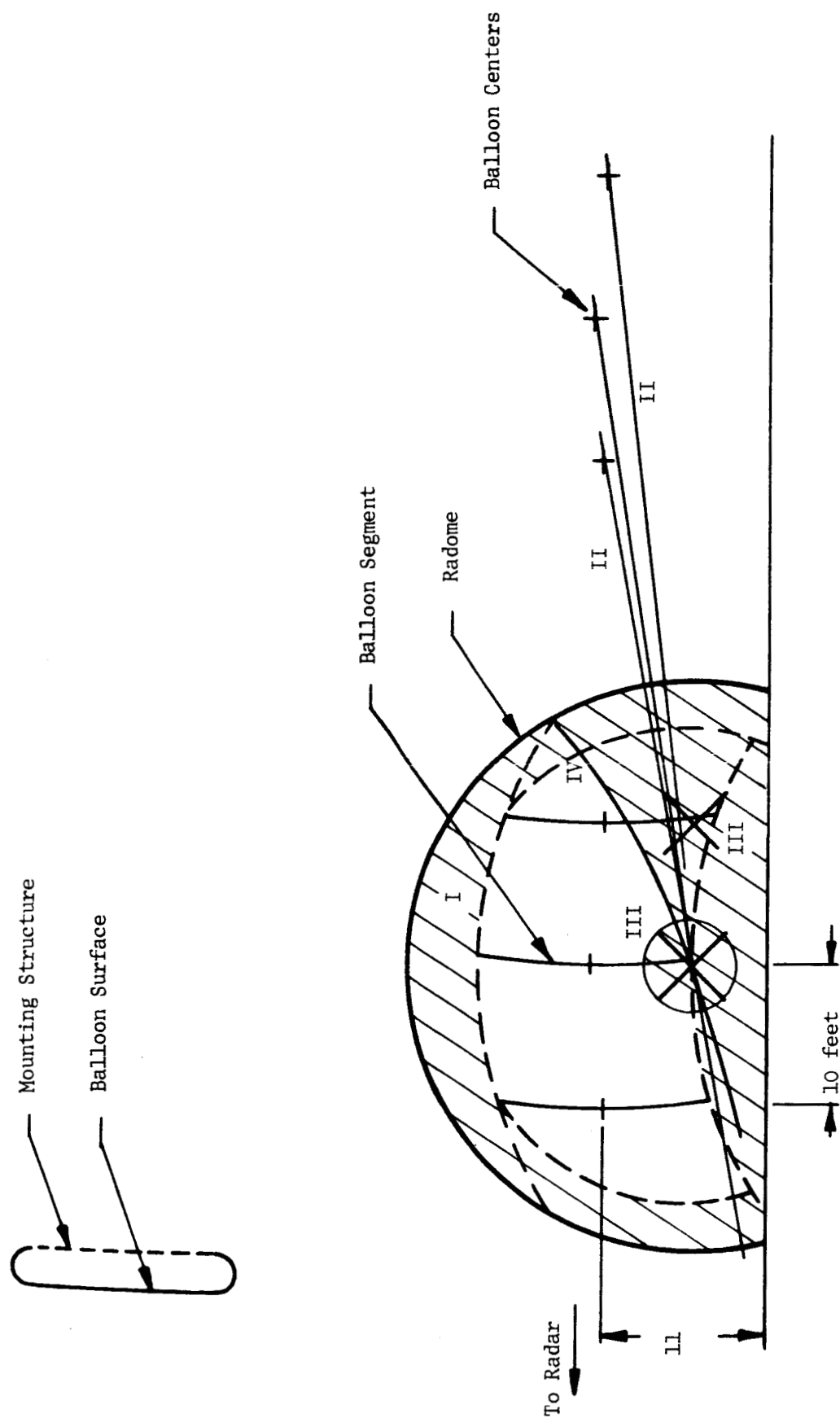


Figure 3.8 The Optimum Location of the Test Fixture

that of the usual target measured inside the radome. However, when the target is located in the equatorial plane of the radome, three specular sources, the near and far side of the radome plus the target, contribute to the backscattered field. When no target is in the radome the field comes primarily from the front and rear specular points of the radome. This field is designated:

$$E_{\text{radome}} = E_1 e^{i\phi_1} + E_2 e^{i\phi_2}$$

When the CW radar bridge is balanced this involves the introduction of signal into the detector such that:

$$E_{\text{detected}} = E_1 e^{i\phi_1} + E_2 e^{i\phi_2} - E_1 e^{i\phi_1} - E_2 e^{i\phi_2} = 0$$

Thus when a target is placed in the radome the detected signal becomes:

$$E_{\text{detected}} = E_1 e^{i\phi_1} + E_2 e^{i\phi_2} - E_1 e^{i\phi_1} - E_2 e^{i\phi_2} + E_3 e^{i\phi_3} = E_3 e^{i\phi_3}.$$

However, when a target large enough to completely shield the rear specular zone is measured, the detected signal is:

$$E_{\text{detected}} = E_3 e^{i\phi_3} - E_2 e^{i\phi_2}$$

Since  $|E_2|^2 \approx \frac{1}{2} |E_1|^2$  the measured cross section of a target placed in the radome's equatorial plane is,

$$\sigma_{\text{meas.}} \approx \sigma_{\text{target}} + \frac{1}{2} \sigma_{\text{radome}} - \sqrt{2} (\sigma_t \sigma_r)^{1/2} \cos (\phi_3 - \phi_2).$$

The phase,  $\phi_3 - \phi_2 = 2k l$ , varies as a function of the distance between the target and the back wall and it can be seen that if  $\sigma_r$  is much greater than  $0.02 \sigma_t$ , a noticeable error could result. This error can be eliminated by moving the target up in the radome. The target must be located sufficiently above the equatorial plane so that the shadow area which is caused by the placement of the target in the field is not a significant contributor to the

radar cross section of the radome. As noted above,  $\sigma_r$  is of the order of  $0.5 \text{ m}^2$ . For the segments  $\sigma_t$  is of the order of  $1200 \text{ m}^2$  and thus no noticeable errors should be introduced by shadowing the back wall.

Except as noted above, the radome-target multipath contributions are approximately,

$$\sigma_{\text{multipath}} \approx R \sigma_{\text{target}}$$

where  $R (\approx 2 \times 10^{-3})$  is the radome reflection coefficient. These contributions can be safely ignored for the large backscattered echo area targets usually measured inside the radome.

The above considerations eliminate the necessity of further considering the multipath errors caused by the general range geometry. After the radome is eliminated as a significant source of backscattered energy, the problem reduces to one of the same type as has previously been considered in other phases of this program. One might point out that the radome, being spherical in shape, is an isotropic scatterer and thus the fresnel zone on the ground will be illuminated with energy which is of the same intensity as the primary wave. It can be shown, however, that the pattern of the receiving antenna is such that the energy from the fresnel zone is not received in the area of a pattern maximum. Even if this were not the case, and the waves were of equal amplitude at the receiving antenna, the magnitude of the radome reflection coefficient is such that the resultant effective echo area would still be less than  $1 \text{ m}^2$ , and thus of no importance to segment measurements.

#### 3.4.4 Experimental Evaluation

In addition to the above described analytical evaluations, the radome was evaluated experimentally. A series of measurements were performed in the X- and C-band microwave frequency regions on several different spheres and flat plates to determine if their reflection patterns or echo areas were changed by placement in the radome.

For radar cross section measurements, Conductron generally uses a CW measurement technique. For this project a bistatic system with  $\beta \leq 3^\circ$  was

used and Figure 3.9 is a representative block diagram of such a system. In general, the measurement system consists of a microwave network used in conjunction with a Scientific-Atlanta series 402B Wide Range Receiver and a Scientific-Atlanta model APR-23 linear-logarithmic rectangular recorder. The output data were provided in rectangular analog recordings of backscattered power versus azimuth rotation angle. The recorder specifications include accuracies of  $\pm 0.25$  db in power and  $\pm 0.05^\circ$  in azimuth angle, and a linearity of 0.5 db over the full 40 db dynamic range.

The microwave network consists of a frequency source, an antenna, and the necessary microwave components and transmission lines. For this project the frequency sources used were phase-stabilized klystron oscillators having output powers of greater than 0.5 watt. Linearly polarized parabolic reflector antennas were used as the radiation sources and were mounted in such a way that the electric vector could be oriented at any angle. A Scientific-Atlanta Model PP-13 polarization positioner, having an angular accuracy of  $0.05^\circ$ , was used for this purpose.

The first step in the measurement procedure was to place an azimuth positioner in the correct spot and make sure that the turntable was perfectly level. When this was accomplished, a Dylite support column was set in place. The column was rotated and a K & E model KE-1E theodolite was used to assure that the column was centered and level. The composite background return, including reflections from the model support structure as well as from the radome and the general range, was cancelled in a balancing network. The model was then placed on the support column and the theodolite was used to minimize position error. The model was then rotated  $360^\circ$  in azimuth and the backscattered power plotted as a function of rotation angle. After the measurement was completed the model was removed from the column and a check made to assure that the background level had not changed. In cases where the background level had changed, the data was discarded.

Figures 3.10 through 3.22 are typical of the measurement data which was obtained. The information in the data box of each pattern will serve to identify the pattern. It will be seen that four separate targets were



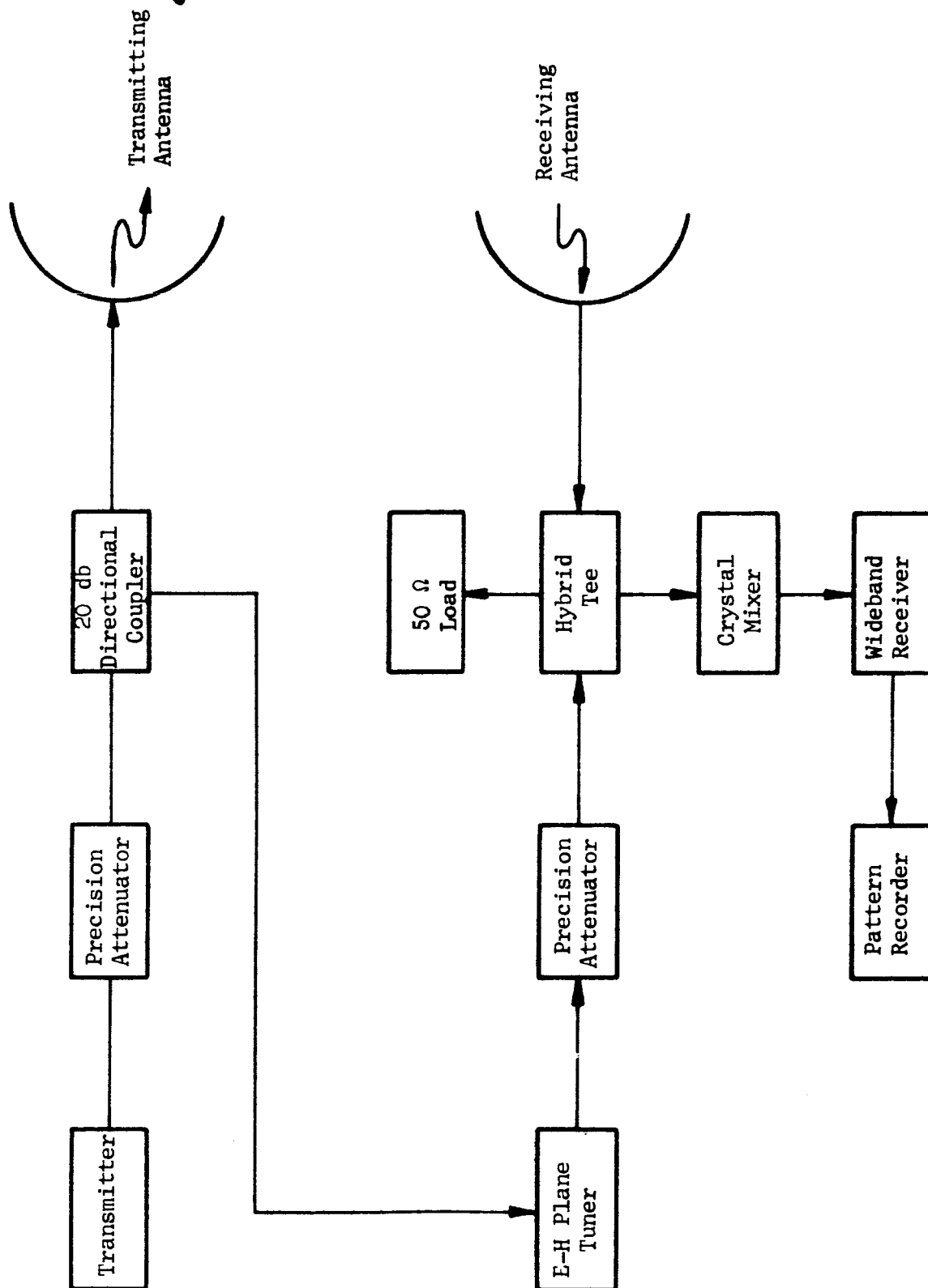
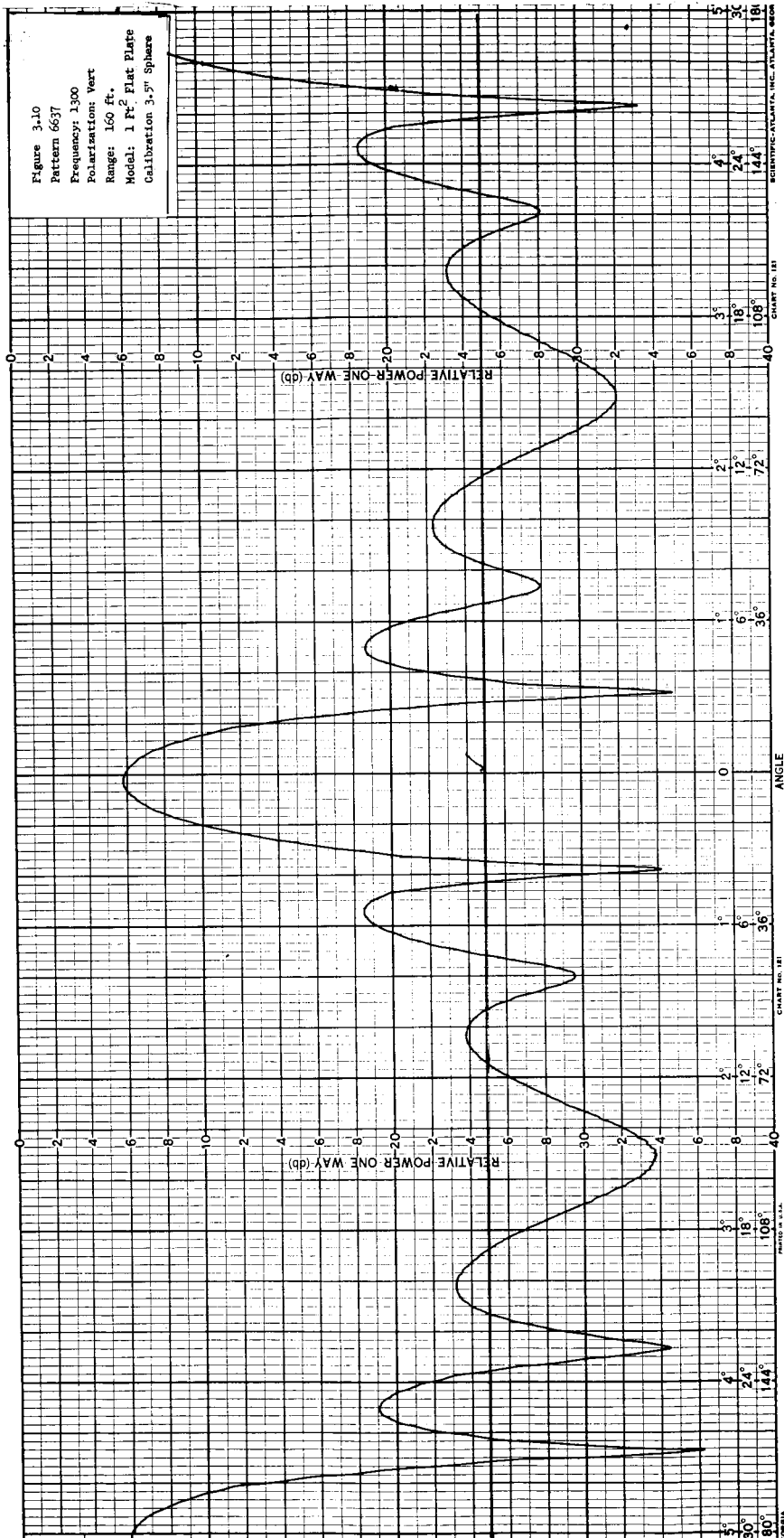
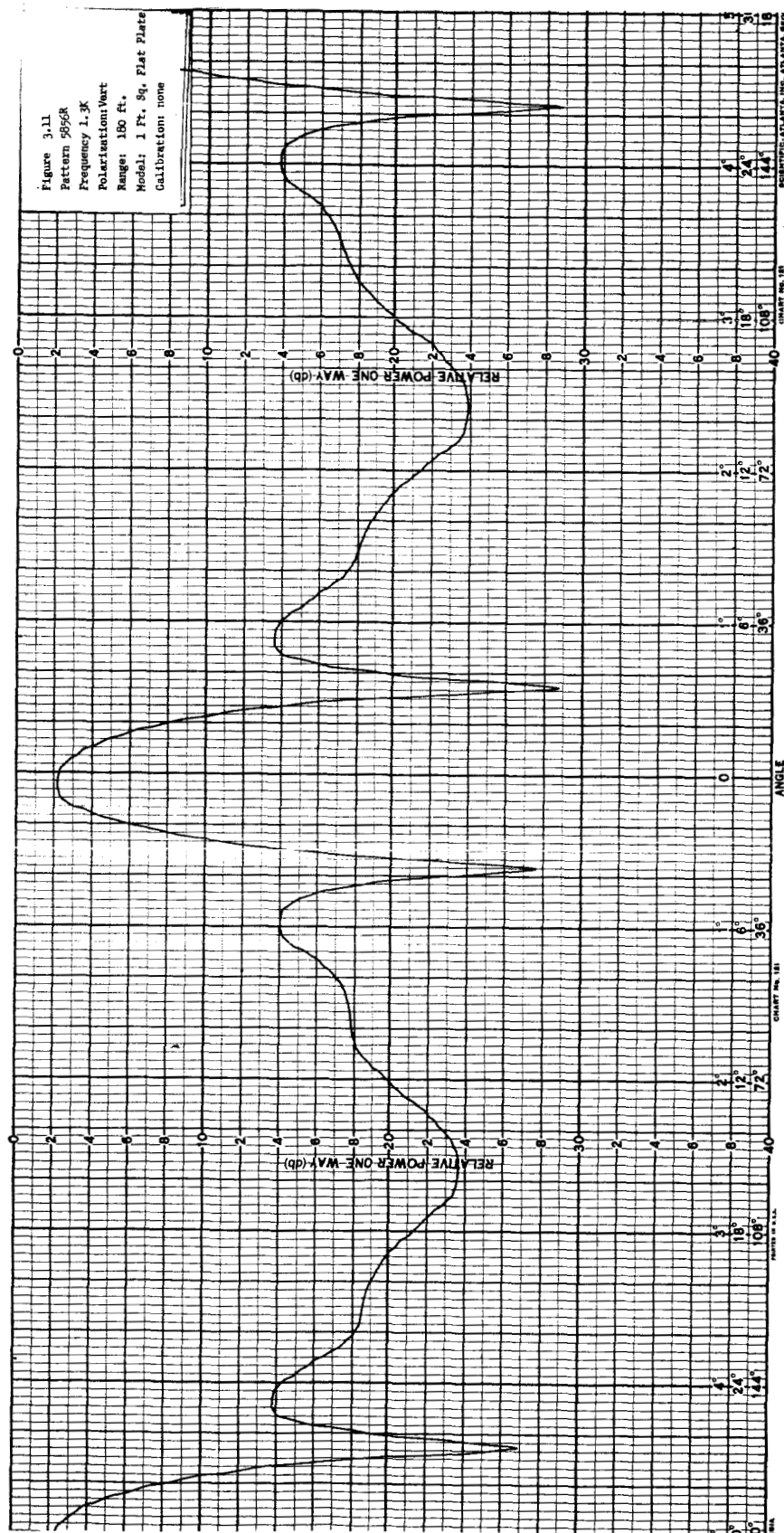
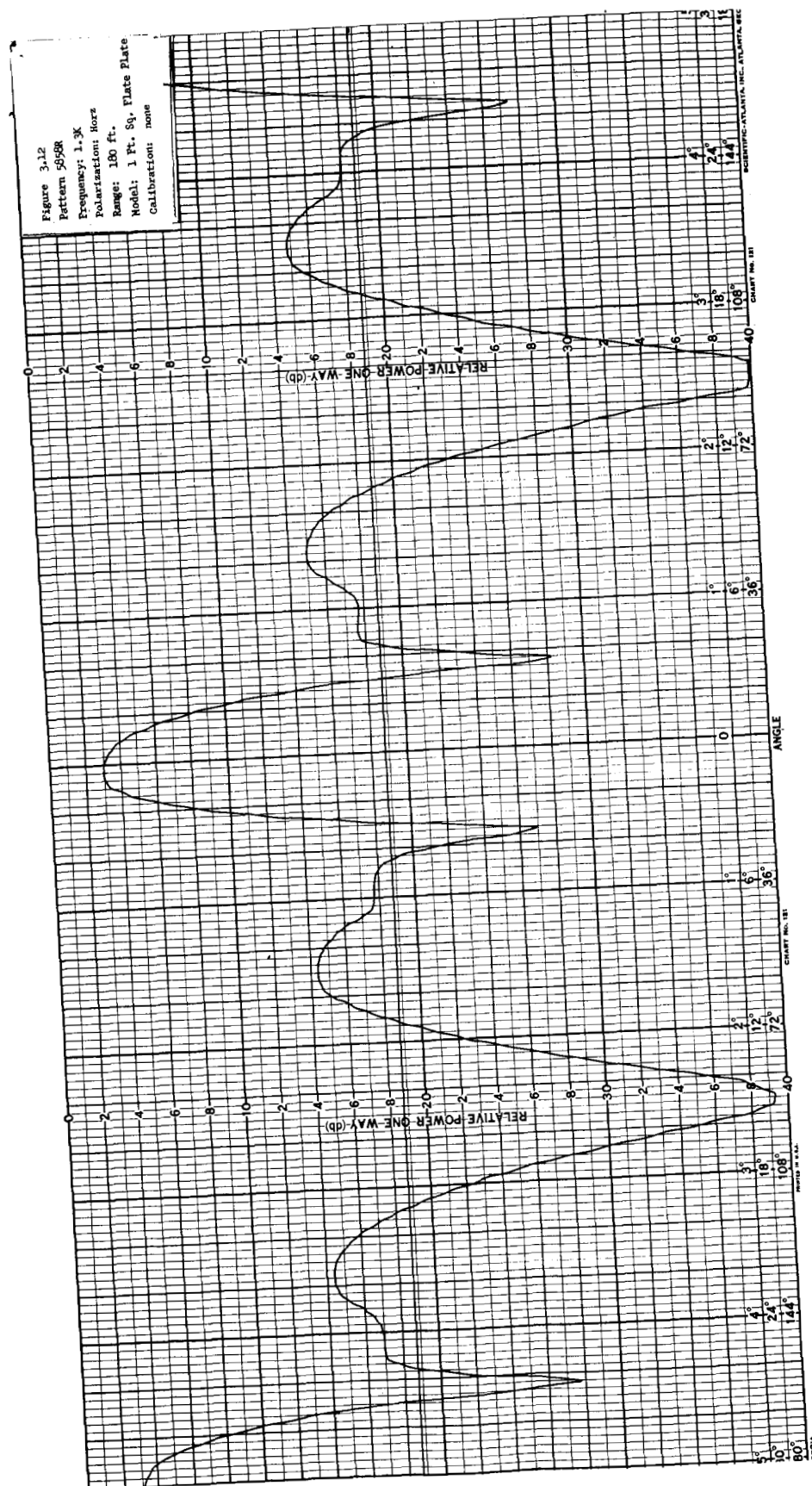
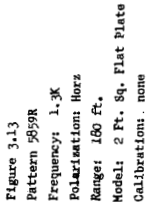


Figure 3.9 Block Diagram of Typical Bistatic CW Measurement System

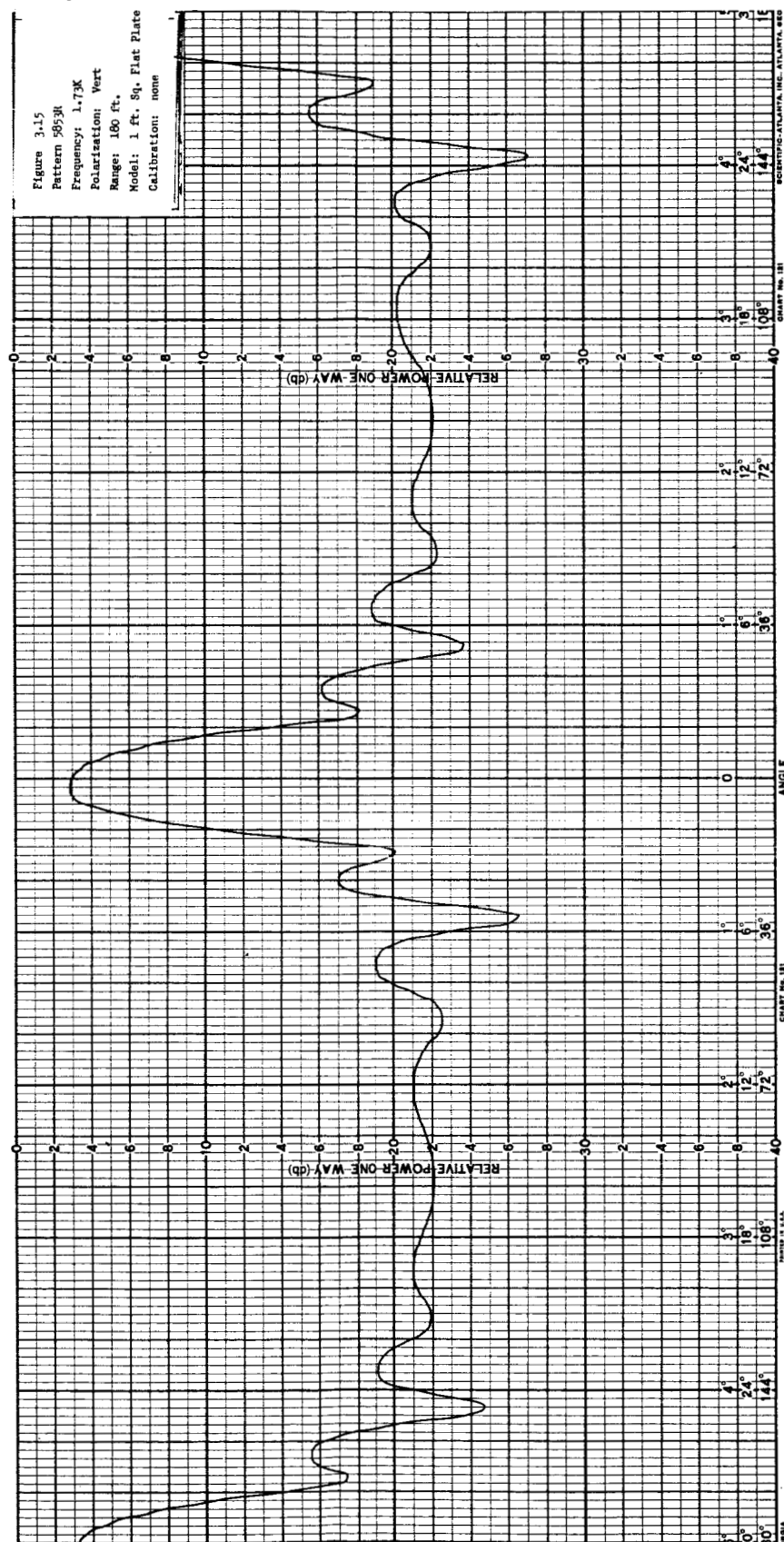






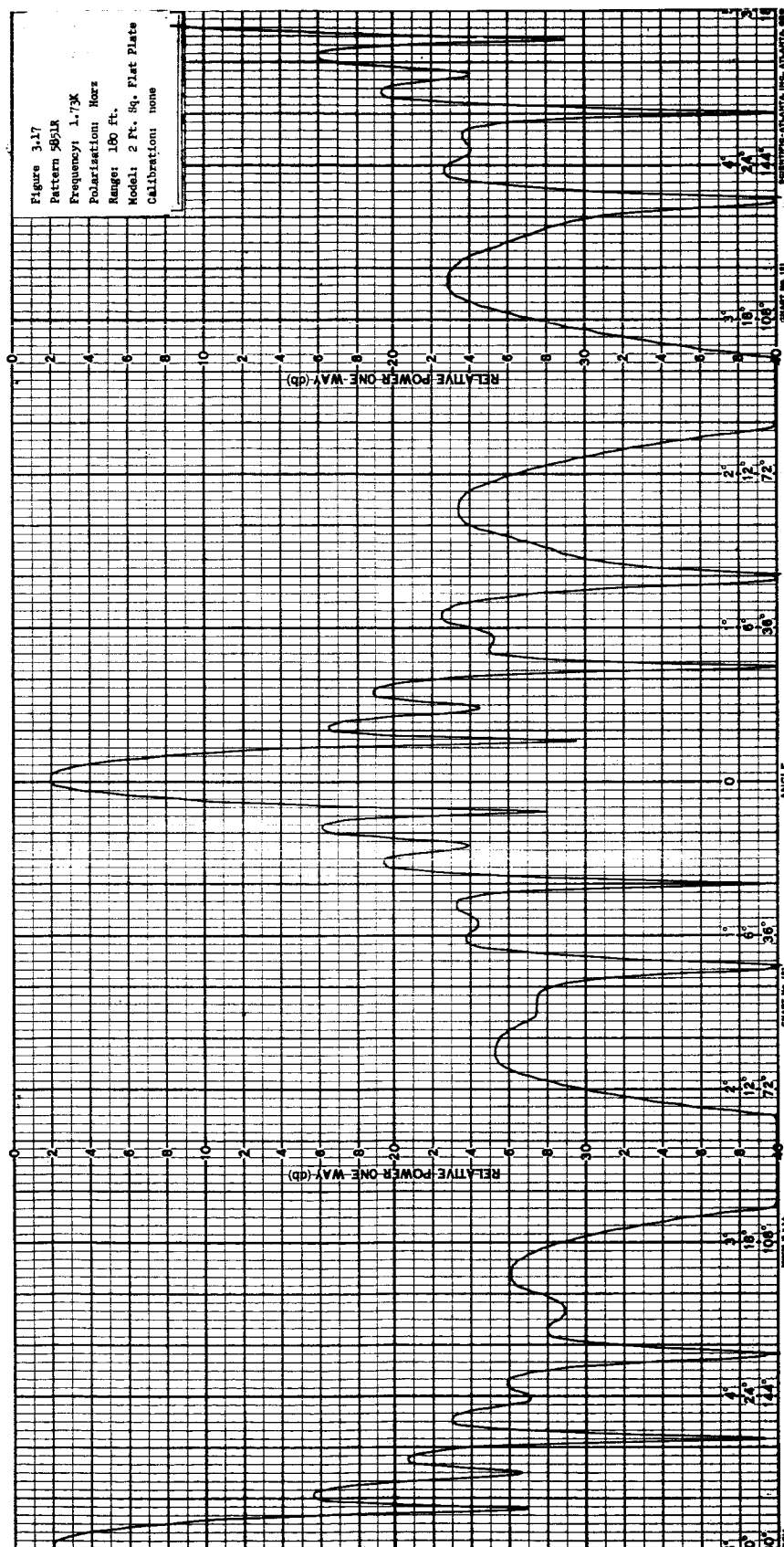














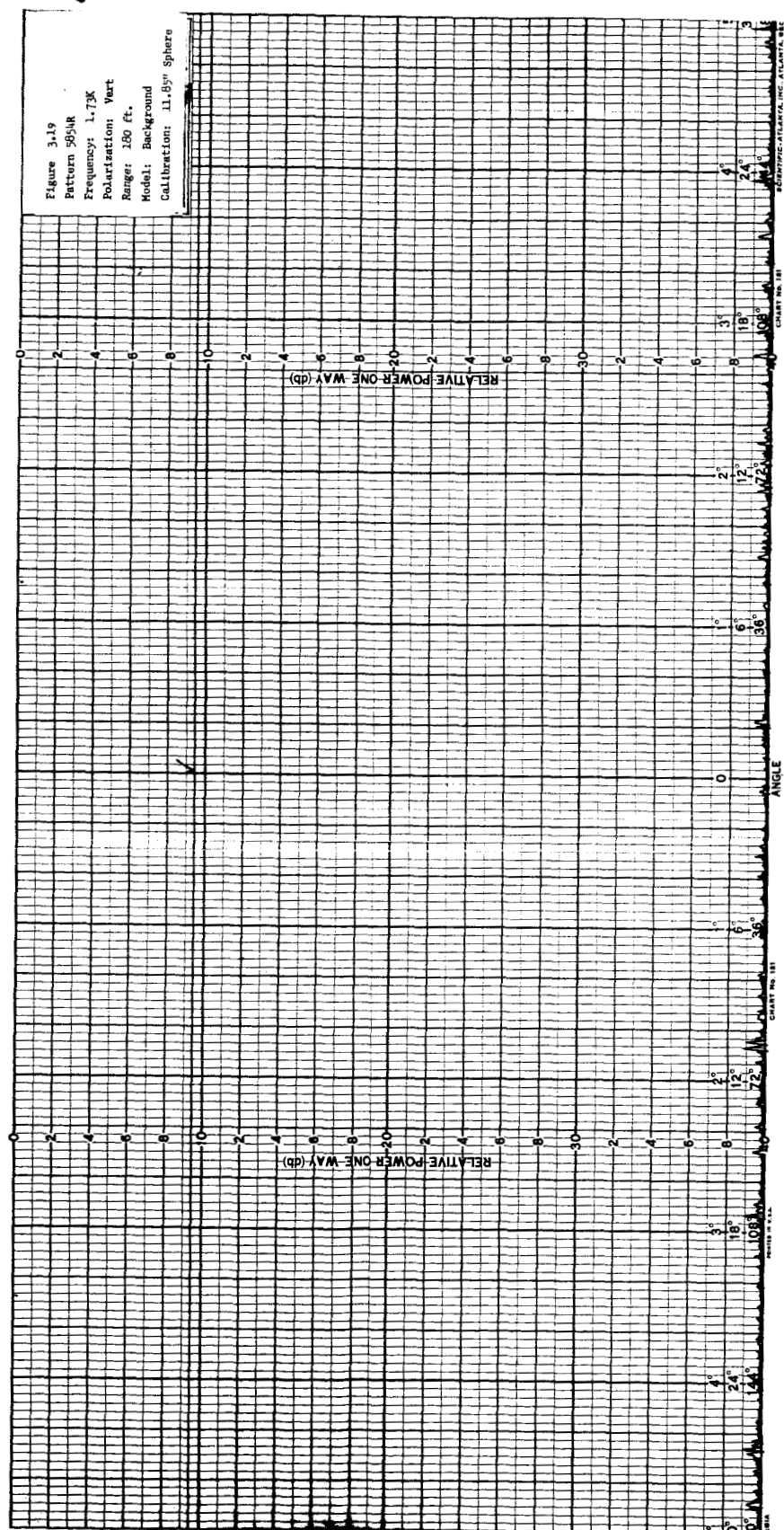
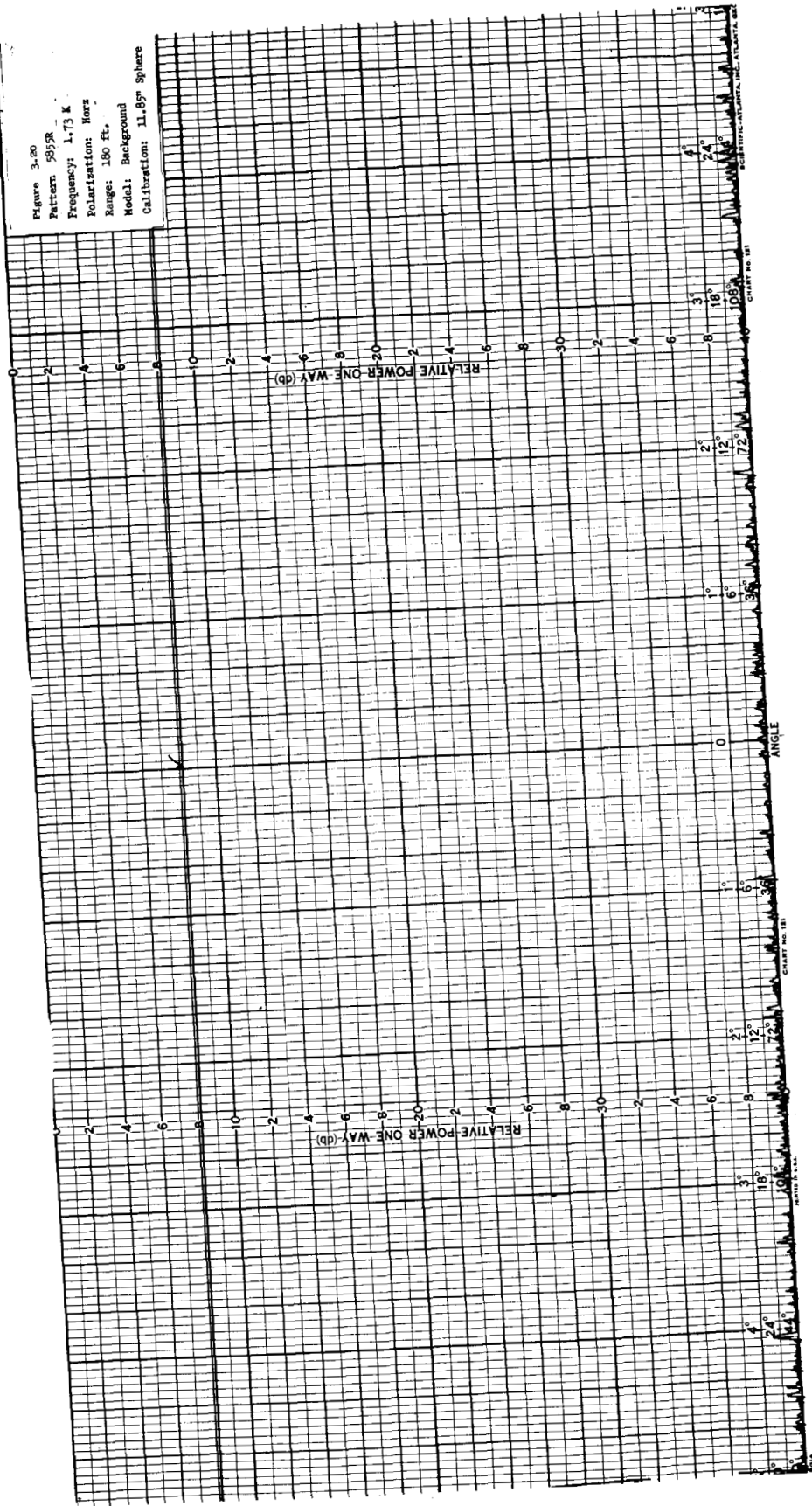


Figure 3.20  
 Pattern 595R  
 Frequency: 1.73 K  
 Polarization: Horz  
 Range: 180 ft.  
 Model: Background  
 Calibration: 11.89° Sphere



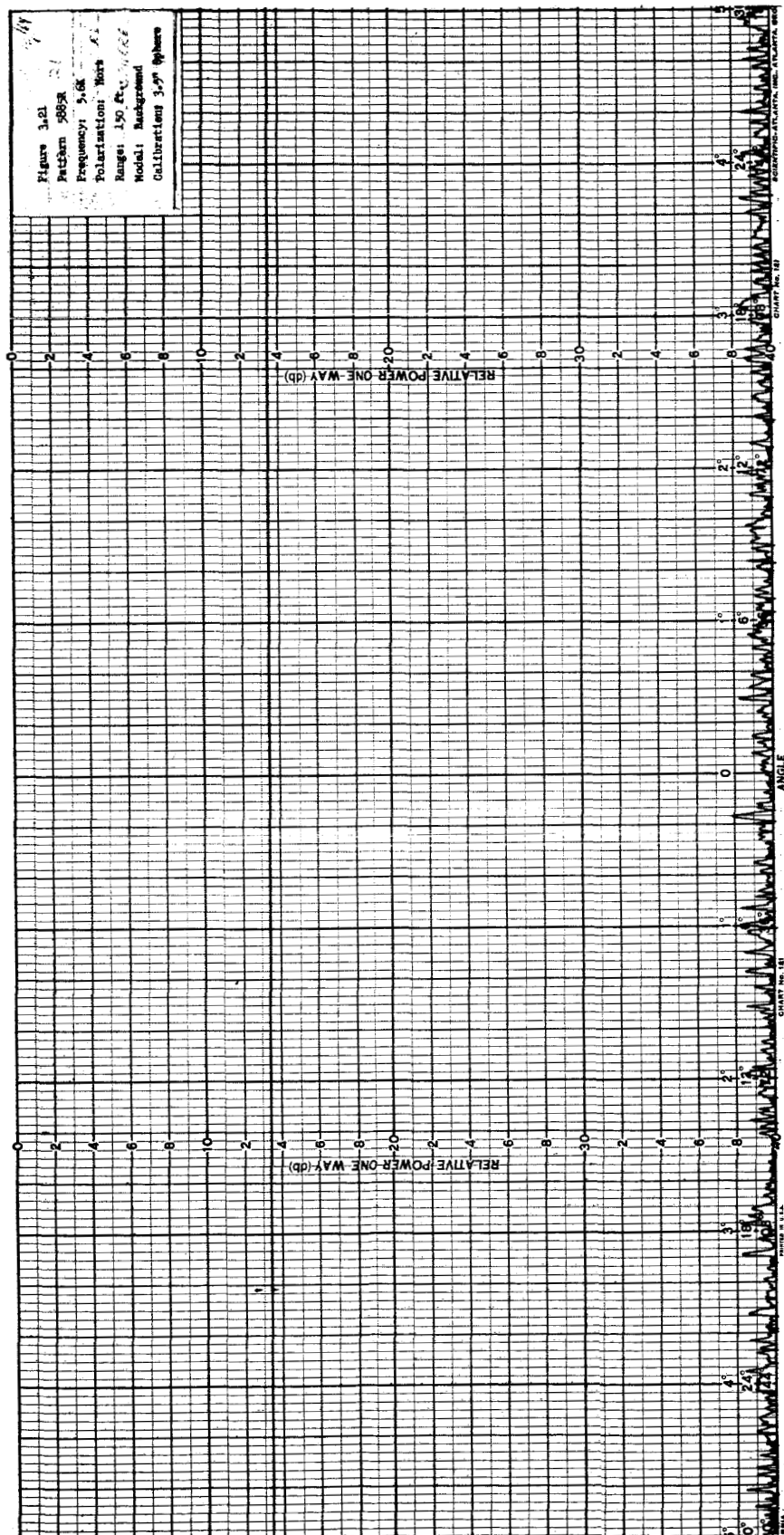
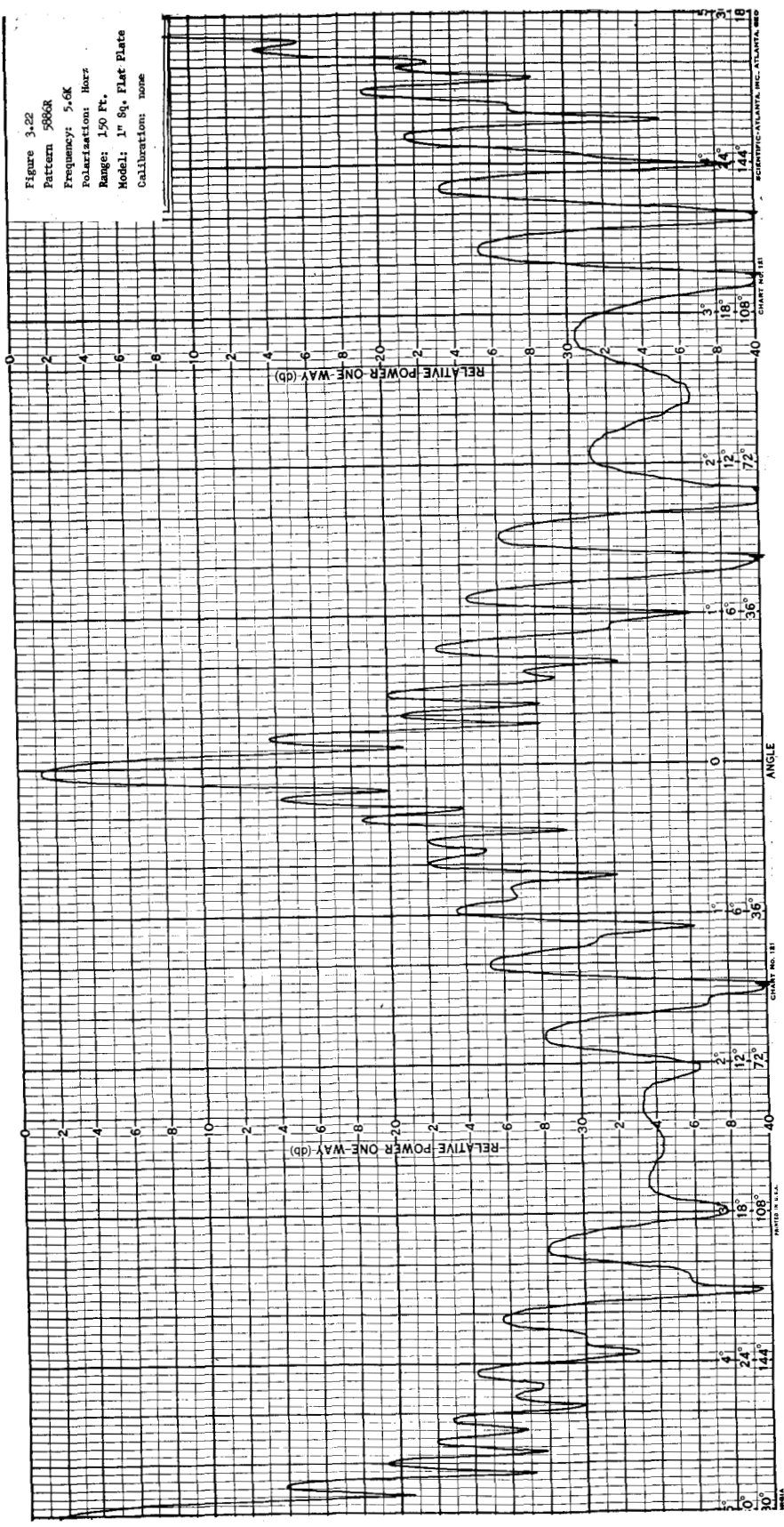


Figure 3-22  
 Pattern 588a  
 Frequency: 5.6K  
 Polarization: Horiz  
 Range: 150 Ft.  
 Model: 1" Sq. Flat Plate  
 Calibration: none



measured: a flat plate 1 foot square, a flat plate 2 feet square, a sphere 3.5 inches in diameter, and a sphere 11.85 inches in diameter. The results of these measurements indicated an excellent agreement with the theory.

For example, Figure 3.10 is the radar cross section of a flat plate which is 1 foot square, as measured outside the radome, and Figure 3.11 is the same plate measured inside the radome. This was a very important test since the radar cross section of the flat plate is very nearly equal to that of the radome. In Section 3.4.1 above, the radome was estimated to have a radar cross section of approximately 0.5 square meters or -6.0 db  $> m^2$ . The flat plate radar cross section is given by:

$$\sigma_{\text{flat plate}} = \frac{4\pi A^2}{\lambda^2}$$

where

A = flat plate area

$\lambda$  = wavelength and at 1.3 kmc = .23 meters

$\sigma_{\text{flat plate}}$  = 3.1 square meters

$\approx 5.0 \text{ db } > m^2$

Thus the difference in radar cross section between the flat plate and the radome is approximately 11 db and thus we would expect some distortion of the flat plate pattern as taken in the radome. Figure 3.11 shows some distortion in the sidelobe structure and indicates that the estimate of the radome echo area is essentially correct.

Figure 3.13 shows two reflection patterns of a flat plate 2 feet square mounted in the radome. These two patterns were taken at two different times and show the repeatability which can be obtained. Time stability is necessary to the correct evaluation of the ECHO segments and this pattern shows that the time stability of the measurement system is not affected by the presence of the radome. In general, the experimental data was consistent with previous estimates and it appears that excellent results will be obtained on the segment measurements, with no adverse effects introduced by the radome.

### 3.4.5 The Radome as a Housing for a Transmitting Antenna

As indicated at the beginning of Section 3.4, Conductron performed a limited analysis to determine the suitability of the radome as a housing for a transmitting antenna. The theoretical hypothesis was that a free space dipole antenna was located at the center of a large, spherical, thin-wall radome. The problem is to determine the extent to which the antenna radiation pattern is affected by the presence of the radome.

If the dipole source is located at the center of the spherical dielectric shell, the problem is straightforward and has already been solved by the Kellers<sup>(7)</sup> who considered the more general three-medium problem. Hence for our purpose, all that is required is to modify their results.

The notation we shall use is the same as in Reference (8) and differs from the Kellers' notation. The electromagnetic fields  $\vec{E} e^{-i\omega t}$  and  $\vec{H} e^{-i\omega t}$  are written in terms of the vector potential  $\vec{A} e^{-i\omega t}$  satisfying

$$(\nabla^2 + k^2) \vec{A} = 0 \quad (3.25)$$

in the following manner

$$\begin{aligned} \vec{H} &= \nabla \times \vec{A}, \\ \vec{E} &= \frac{i\omega}{k^2} [\nabla (\nabla \cdot \vec{A}) + k^2 \vec{A}]. \end{aligned} \quad (3.26)$$

For a point dipole with axis in the z-direction, in a medium of infinite extent, the solution of Equation (3.25) is found to be a vector with a single component

$$A_z = A_0 (e^{ikr}/r), \quad (3.27)$$

where  $A_0$  is a constant proportional to the dipole strength.

---

(7) H. B. Keller and J. B. Keller, "Reflection and Transmission of Electromagnetic Waves by a Spherical Shell", J. App. Phys. 20, 393-396 (1949).

(8) J. J. Bowman, "High-Frequency Scattering from a Conducting Sphere Surrounded by a Thin-Wall Radome", Conductron Memo D4420-233-M, August 20, 1964.



With the presence of the spherical dielectric shell, the solution of Equation (3.25) is a vector with the following non-zero component

$$\begin{aligned}
 A_z &= A_0 \frac{e^{ikr}}{r} + A_1 \frac{e^{-ikr}}{r}, \quad 0 < r < b \\
 A_z &= A_2 \frac{e^{ik_1 r}}{r} + A_3 \frac{e^{-ik_1 r}}{r}, \quad b < r < a \\
 A_z &= A_4 \frac{e^{ikr}}{r}, \quad a < r
 \end{aligned} \tag{3.28}$$

where  $k_1 = \sqrt{\epsilon}k$  is the propagation constant with the dielectric. The coefficient  $A_1$  for the reflected field and the coefficient  $A_4$  for the transmitted field are given by Keller. Adopting and simplifying their expressions to suit our problem, we find

$$\frac{A_1}{A_0} e^{-2ikb} = \frac{(1-\epsilon) [F(\sqrt{\epsilon}) G^*(\sqrt{\epsilon}) - F(-\sqrt{\epsilon}) G^*(\sqrt{\epsilon}) e^{2ik_1 \delta}]}{(1+\sqrt{\epsilon})^2 F(\sqrt{\epsilon}) G(\sqrt{\epsilon}) - (1-\sqrt{\epsilon})^2 F(-\sqrt{\epsilon}) G(-\sqrt{\epsilon}) e^{2ik_1 \delta}}, \tag{3.29}$$

$$\frac{A_4}{A_0} = \frac{4\sqrt{\epsilon} e^{-ik\delta}}{(1+\sqrt{\epsilon})^2 F(\sqrt{\epsilon}) G(\sqrt{\epsilon}) e^{-ik_1 \delta} - (1-\sqrt{\epsilon})^2 F(-\sqrt{\epsilon}) G(-\sqrt{\epsilon}) e^{ik_1 \delta}}, \tag{3.30}$$

where

$$F(\sqrt{\epsilon}) = 1 - \frac{1}{ika} \left(1 - \frac{1}{\sqrt{\epsilon}}\right) - \frac{1}{k^2 a^2} \left(1 - \frac{1}{\sqrt{\epsilon}}\right)^2 - \frac{1}{i\sqrt{\epsilon}} \frac{1}{k^3 a^3} \left(1 - \frac{1}{\sqrt{\epsilon}}\right),$$

$$G(\sqrt{\epsilon}) = 1 + \frac{1}{ikb} \left(1 - \frac{1}{\sqrt{\epsilon}}\right) - \frac{1}{k^2 b^2} \left(1 - \frac{1}{\sqrt{\epsilon}}\right)^2 + \frac{1}{i\sqrt{\epsilon}} \frac{1}{k^3 b^3} \left(1 - \frac{1}{\sqrt{\epsilon}}\right),$$

and  $\delta = a-b$ . When  $ka$  and  $kb$  become infinite while  $a-b = \delta$  and  $r-b = x$  remain

finite and  $A_0 (e^{ikb}/r)$  approaches a limit  $A'_0$ , the problem reduces to that of plane waves normally incident on a flat plate separating two identical half-infinite media [See e.g. Reference (2) pp. 512(9)].

We are interested in the expansion of the transmitted field under the conditions

$$kb \gg 1 ,$$

$$k_1 \delta \ll 1 ,$$

and we obtain, to first order in  $k\delta$ ,

$$\frac{A_4}{A_0} = 1 - \frac{k\delta}{2i} (\epsilon-1) + \frac{1}{ikb} \frac{\delta}{2b} \frac{(\epsilon-1)(\epsilon-2)}{\epsilon} + O\left(\frac{1}{k^3 b^3}\right) . \quad (3.31)$$

Recall that to this order in  $k\delta$ , the amplitude transmission coefficient for a plane sheet is given by

$$T_E = T_H = 1 - \frac{k\delta}{2i} (\epsilon-1) \quad (3.32)$$

Since the transmission coefficient of the material in the NASA radome is high, we would not expect to encounter any difficulty in using this radome as a housing for a transmitting antenna.

#### 4. TEST FIXTURE

A test fixture has been constructed inside the radome which is capable of accepting segments of satellite material for radar transmission and reflection testing. The basic structure is constructed of light-weight aluminum and is 20 feet in diameter. An inflatable torus is fitted around the outside circumference to achieve an overall diameter of 22 feet. The satellite material is mounted on the front of the fixture with its edge passing over the torus. An air-tight seal is made between the satellite material and structure. An inflation envelope is made by enclosing the back of the fixture with a film of mylar 0.0075 inch thick. An air tight seal is also made between the mylar film and the structure. The fixture is mounted on a heavy duty, three-axis antenna positioner which was supplied to Conductron for use on this project by the National Aeronautics and Space Administration. The concept is shown in Drawing #124204 in Appendix B, and the assembled test fixture is shown in Figure 4.1 and 4.2.

##### 4.1 Construction of Basic Structure

The basic structure is circular in shape and constructed of light-weight aluminum. A complete set of fabrication drawings are included in this report as Appendix B.

The outer rim of the structure is made of 14 aluminum castings having a configuration as shown in Drawing #122402. As can be seen from the drawing, each casting has a doubly curved surface. The concave rim surface has a 6 inch radius of curvature and was designed as a mounting face for the inflatable torus. The convex rim surface is curved so that when the castings are bolted together end to end, a circular structure 20 feet in diameter is formed. Each casting was fabricated using typical sand casting techniques and X-rayed to insure freedom from structural defects. The surface irregularities were removed by sandblasting or hand grinding wherever necessary. The planer surface of each casting was milled to a tolerance of  $\pm .005$  inch to provide a flat mounting surface for the support trusses, the segment material, and the mylar film.

The rim structure is supported by four trusses which are constructed of aluminum tubing. Mounting plates are welded to each end of the truss structure so that the truss can be bolted to the rim and to the positioner mounting plate. The

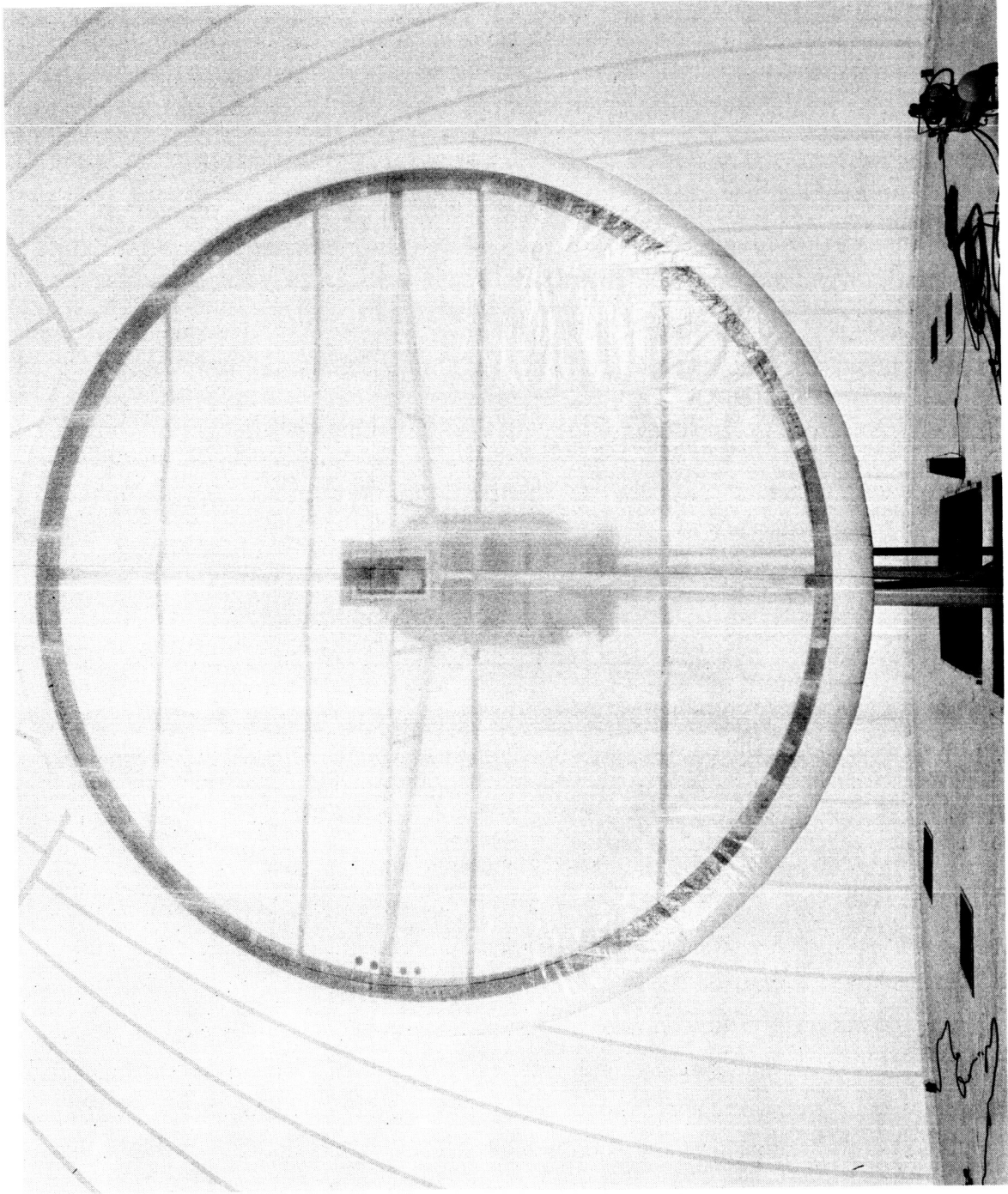


Figure 4.1 Test Fixture, Front View

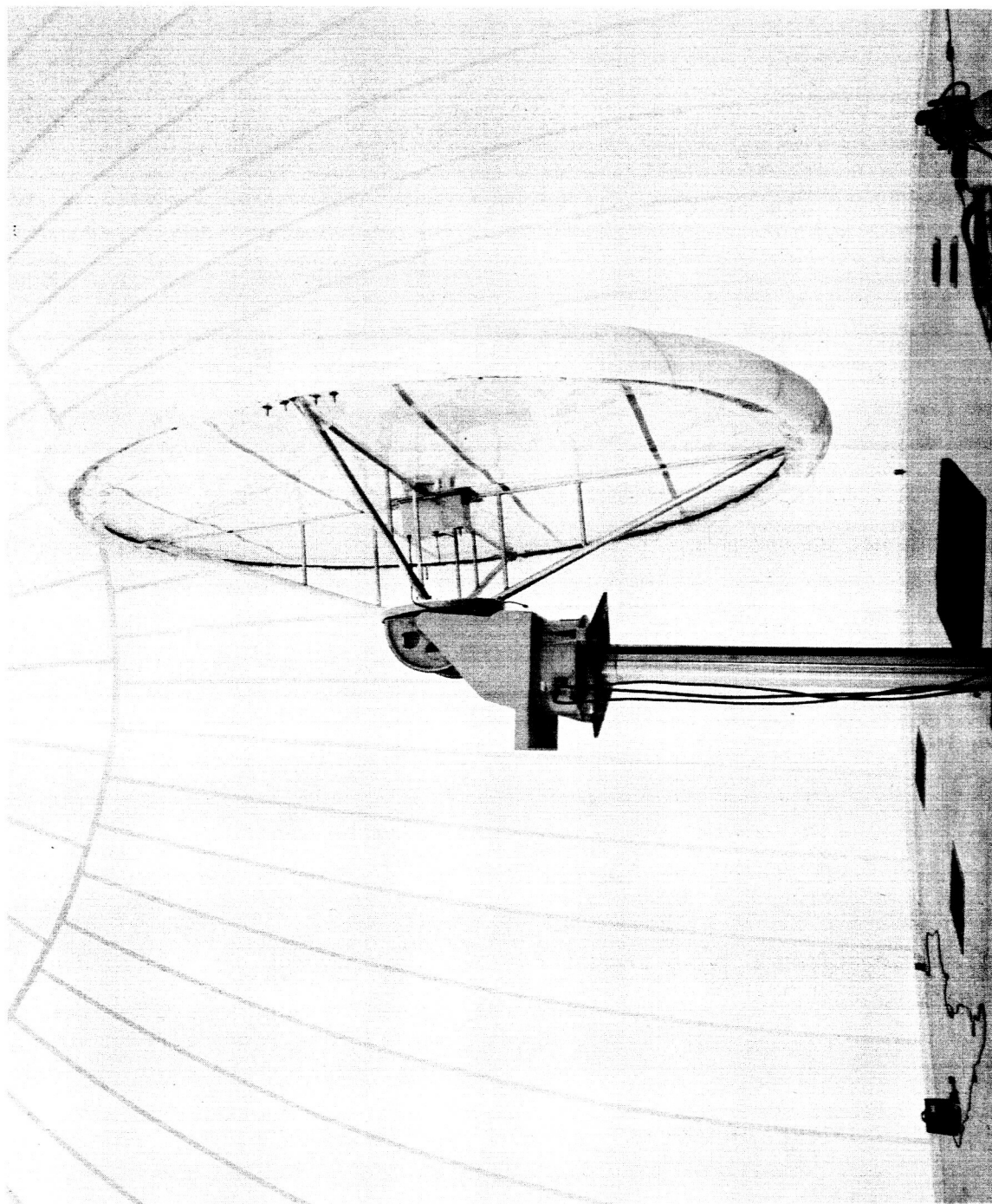


Figure 4.2 Test Fixture, Rear View

support trusses also provide a mounting base for the transmission measurement antenna assembly. The truss assembly is shown in Drawing #122407 and in Figure 4.2, the mounting plate is shown in Drawing #122430, and the antenna assembly is shown in Drawing #122457.

The fixture is assembled by first bolting together the rim structure in an inverted position so that the planer mounting surface is upward. A cork gasket is then cemented to the mounting surface and the mylar backing material is bonded to the cork. The support trusses are then bolted to the rim structure and the positioner mounting plate is bolted to the trusses tying the entire structure together. Figure 4.3 shows the method which is used to attach the rim sections together and the attachment between the rim and the support trusses. Figure 4.4 shows the attachment between the support trusses and the positioner mounting plate.

The mylar retaining ring is then bolted into place making an air-tight seal between the rim structure and the mylar. The retaining ring is constructed of 0.125 inch aluminum and is 3.9 inches wide. It is made in seven sections which are arranged so that each joint in the rim structure is spanned. A cork gasket is bonded to the under side of the ring, to insure the mylar air seal, and a foam rubber gasket is bonded to the upper side to protect the segment material from any sharp edges. The retaining ring is slotted and keyed to prevent interference with the support trusses.

The entire structure is then turned over, so that the mounting plate is on the under side, and placed on the antenna positioner. The weight of the structure is approximately 650 pounds, thus in order to turn it over, it is necessary that an overhead support mechanism, such as a crane, be employed to insure personnel and equipment safety. When the structure is turned over the positioner mounting plate is fastened securely to the antenna positioner using twelve 0.5 inch diameter bolts.

The torus is then installed by first positioning the air inlet valves on the inside diameter of the torus with the pass holes in the rim structure. The torus is then fitted to the outside rim in the same manner as an inner tube would be positioned. When the torus has been mounted and inflated the segment material can be mounted so that it passes over the torus. The material is held securely in place by the segment retaining ring. This ring is also constructed of 0.125 inch

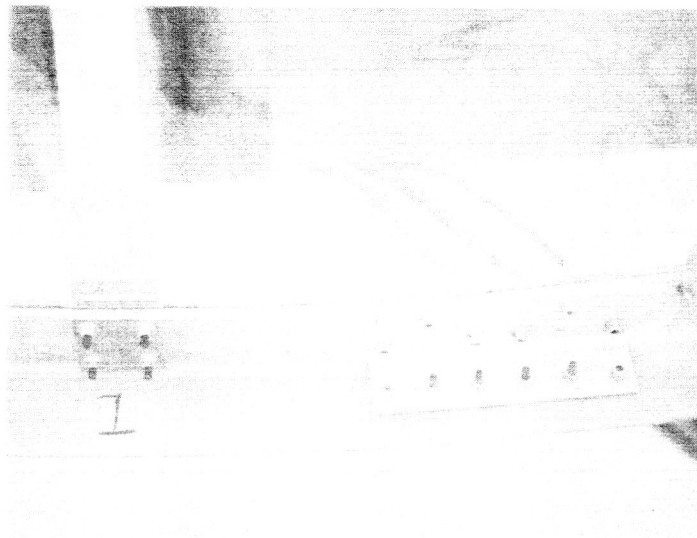


Figure 4.3 Rim Attachments

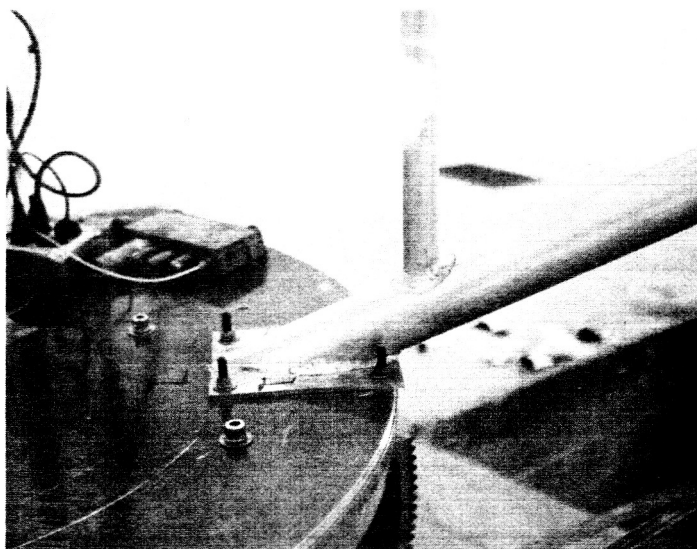


Figure 4.4 Mounting Plate Attachments

aluminum but is only 2.0 inches wide. It is made in seven sections and the bolting arrangement is such that each joint in the rim structure and in the mylar retaining ring spand. A foam rubber gasket is bonded to the under side of the ring to insure an air seal between the segment material and the rim structure and to prevent damage to the segment material from any sharp metallic edges. A cross section of this entire assembly is shown in Drawing #124205.

#### 4.2 Construction of the Torus

The torus is a bi-tubular structure designed to be capable of increasing its outside diameter, uniformly, from 22 feet to 22.5 feet. One tube, referred to as the main torus, has an outside diameter of 22 feet and a tube diameter of 1 foot. This is maintained at a constant pressure level so that it never changes size or shape. The second tube, referred to as the bladder, is attached to the outer circumference of the main torus. The bladder is expandable as a function of internal pressure and provides the capability for increasing the outside diameter from 22 feet to 22.5 feet. Figure 4.5 shows the torus with the bladder deflated, and Figure 4.6 shows the bladder inflated. The torus was designed and built by Raven Industries, Ind. of Sioux Falls, South Dakota.

The objective in constructing this torus was to provide a method for maintaining the overall radius of curvature as the segment skin stress increases. When the segment is initially mounted on the test fixture, the envelope formed between the segment and the mylar film is inflated just enough so that the segment will assume its designed shape.

The segment contour is measured using an optical technique. A vertical index rod is placed close to the segment with the plane defined by the fixture rim normal to the ground. A horizontal index rod is placed underneath the segment and fixture. A photograph is then taken and compared with a standard grid. In this way a silhouette contour is obtained. The segment is then rolled about its axis and silhouette contours are obtained to insure that the segment is symmetrical. Figure 4.7 is a curve showing segment radius of curvature as a function of the distance between the segment center and the plane defined by the front edge of the torus.

When the initial contour has been defined it is necessary to maintain that



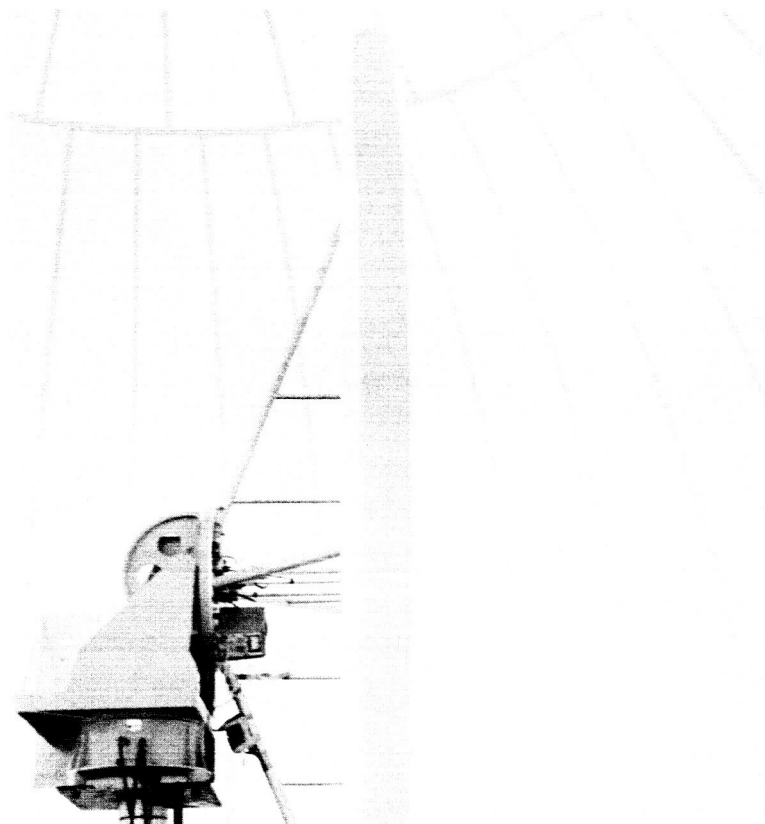


Figure 4.5 Torus, Bladder Inflated

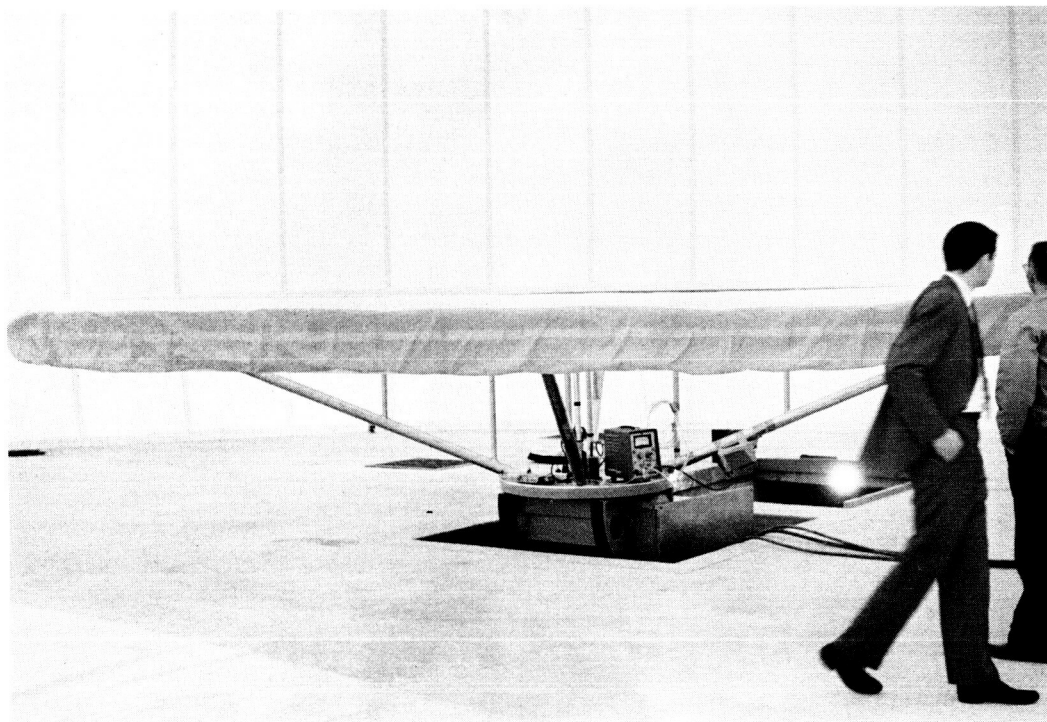


Figure 4.6 Torus, Bladder Deflated

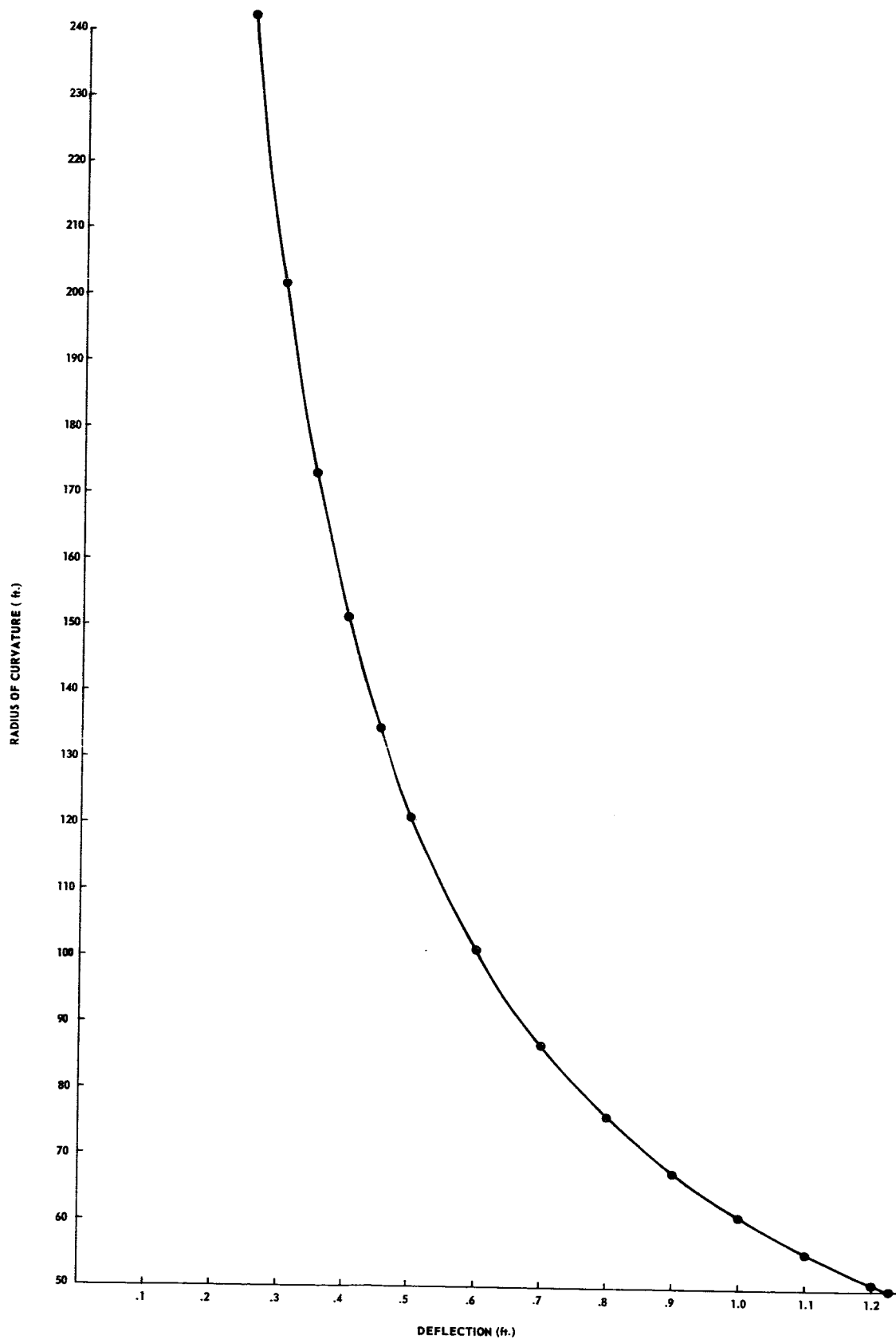
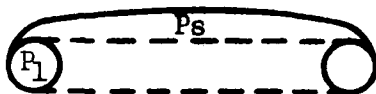


Figure 4.7 Radius of Curvature VS Deflection for a 22 Foot Diaphragm Tester

contour throughout the remainder of the tests. As the internal pressure between the segment and the mylar film is increased the segment skin stress increases and the segment material expands. The overall radius of curvature may be maintained by expanding the edge diameter to compensate for the material expansion. As the material skin stress increases the tension loading on the torus increases proportionately.

The main torus is a gored structure made of a dacron-mylar material. The tolerance on the inside diameter was specified to be  $\pm 0$  and  $-1/4\%$  of the inside diameter when the structure is maintained at the operating pressure under no load. The tolerance on the outside diameter was specified to be  $\pm 0.5$  inch when maintained at the operating pressure under no load and with the bladder collapsed. The bladder is a nylon-mylar material constructed in the same way as the main torus.

One of the more important problems in the design of the torus was to determine the material strength required to withstand the shear forces exerted by the segment material. If one considers a torus supporting a spherical cap, as shown below, the material stresses in the cap should be the same as those in a full sphere having the same radius of curvature and the same internal pressure,  $p_s$ . The stresses should then be given as



$$S_s = \frac{p_s r}{2t} \text{ psi}$$

where  $t$  is thickness and  $r$  is radius, both in inches. If the maximum inflation pressure were .0723 (2 inches of water) in a sphere of 67.5 ft. radius, the skin stresses per unit thickness will be

$$S_s t = \frac{p_s r}{2} = \frac{.0723 \cdot 67.5 \cdot 12}{2} = 29.28 \text{ lbs./in.} \quad (\text{See Figure 4.8})$$

One can then consider the half torus shown below as loaded evenly with centrally directed loads of  $L$  lbs./in. about its circumference. A free force analysis of this section then indicates that the components of load directed normal to the diameter of the torus along which it was severed must be opposed by the forces on

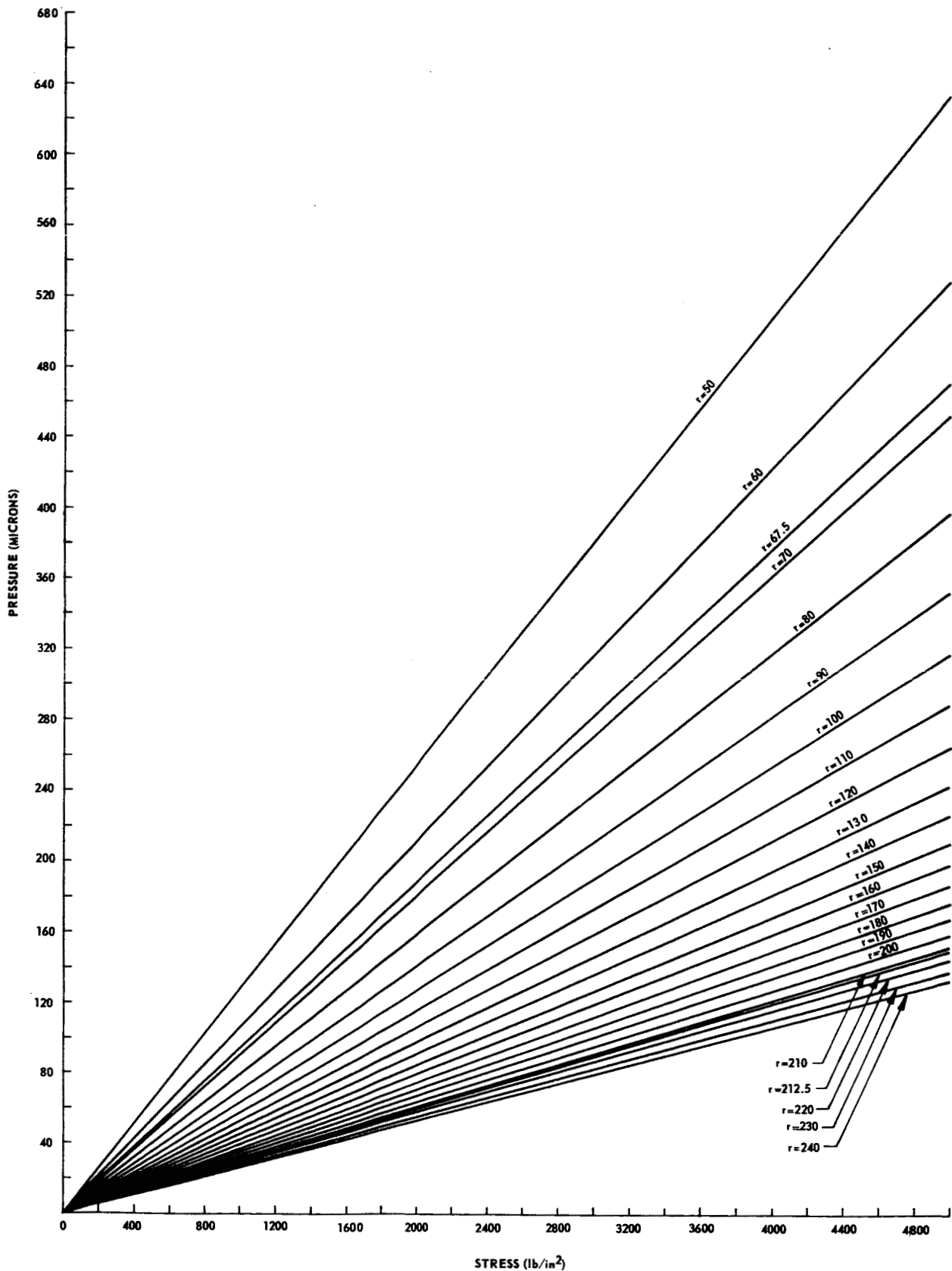
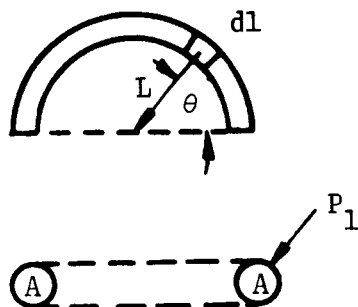


Figure 4.8 Pressure VS Stress for S-SIN-1 & 2 Material  
at Various Radii ( $t = 7.35 \times 10^{-4}$  in)

the severed cross sections, i.e.



$$2p_{iA} = \pi r L \int_0^\pi \sin \theta d\theta$$

$$2p_i \pi r^2 = \pi r L 2$$

$$p_i = \frac{L}{r} = \frac{29.28 \text{ lbs./in.}}{6 \text{ in.}}$$

$$p = 4.88 \text{ psi}$$

In a case in which the structure is to be used repeatedly and must never be allowed to expand into an inelastic region of elongation, safety factors of three or more are justifiable. The greatest stress on the torus will be in a circumferential direction given by

$$S_c = \frac{p_i r}{t}$$

for a tube radius of 6 inches, an internal pressure of 5 psi, and a safety factor of 3, a material strength of

$$S_{ct} = 15.6 = 90 \text{ lbs./in.}$$

is necessary.

High-strength fabric materials are usually heavy and stiff and, therefore, unsuitable for repeated handling. The only material which was suitable for this application was the dacron-mylar bi-laminate. This material is light, weighing only 3.2 ounces per square yard, and is flexible and easy to handle. The material has a strength of approximately 140 pounds per inch.

The second main design problem was the construction of the bladder. In order to properly design the bladder it was necessary to determine the way in which

a bladder expands as a function of tension in the segment material and pressure in the bladder. Tests were performed on a cylinder section, approximately five feet in height and one foot in cross section, simulating a section of the actual torus. Tests were conducted on bladders of six inch and eight inch diameters (fully expanded). The entire test model was constructed of nylon-mylar material.

The test apparatus is shown schematically in Figure 4.9. The basic support was a cylinder section made of sheet steel in the form of a 5" arc of a 1 foot diameter cylinder, five feet long, (C). (A) and (B) are the main torus and bladder, respectively, (D) is a 0-2 psi pressure gauge and (E) and (F) are control valves to allow reading the air pressure in the bladder. (G) are screw closure valves leading to the bladder and torus, respectively. (H) is a Hunter load gauge, (L) is the loading membrane, and K is a crank to allow adjustment of the load.

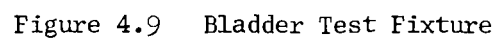
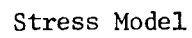
The experimental procedure is as follows:

The cylinder section, with the bladder collapsed, is placed in the rig and the desired air pressure is placed in the main tube, which is then sealed off. The desired load level is registered on the Hunter gauge by adjusting crank K. The bladder is then inflated slowly, while maintaining a constant load on the membrane. As the pressure in the bladder increases, the increase in the bladder expansion along the x axis of Figure 4.9, is recorded as a function of pressure by measuring the distance between the outermost point of the bladder and a fixed reference point on the x axis.

These points are shown in the graphs Figure 4.10 and 4.11, for the six inch and eight inch diameter bladders, respectively. The theoretical curves shown in each of these graphs are plotted from the results of a theoretical analysis of the bladder operation.

Assuming the bladder material to be partially in the form of two half cylinders of radius  $r$  and the rest in the form of two cylinder segments subtending an angle  $\theta$  at the center of the main cylinder as shown below. These sections have radii of  $R$  and  $R + 2r$ . The total surface area of the bladder must always be a constant given by  $A_T = 2\pi r_0 h$  where  $r_0$  is the radius of the fully expanded bladder, and  $h$  is the cylinder height.

The loaded membrane may, at any time, be considered as being supported by the area  $A$ , given by





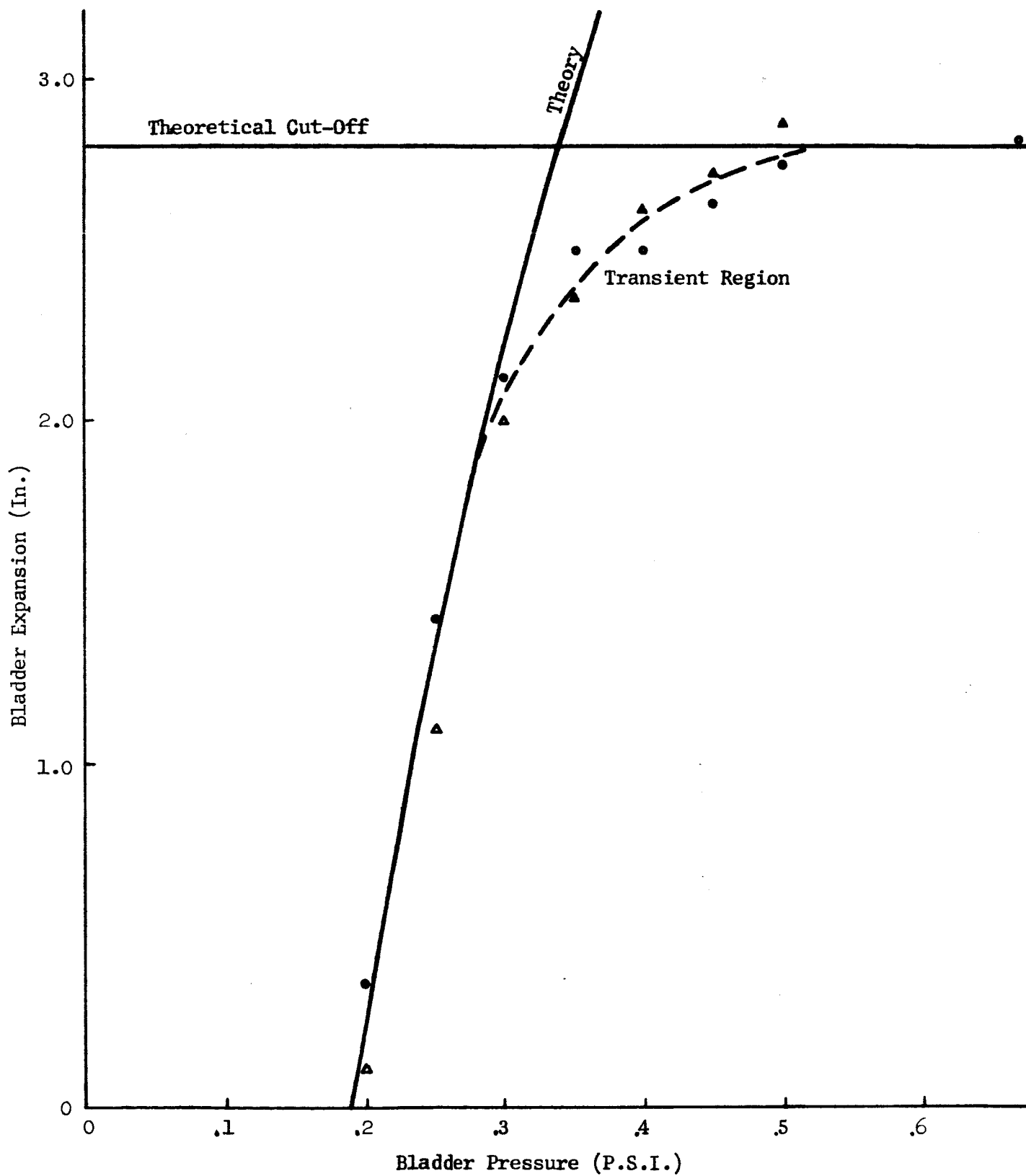


Figure 4.10 Comparison of Theory and Experiment 6" Bladder

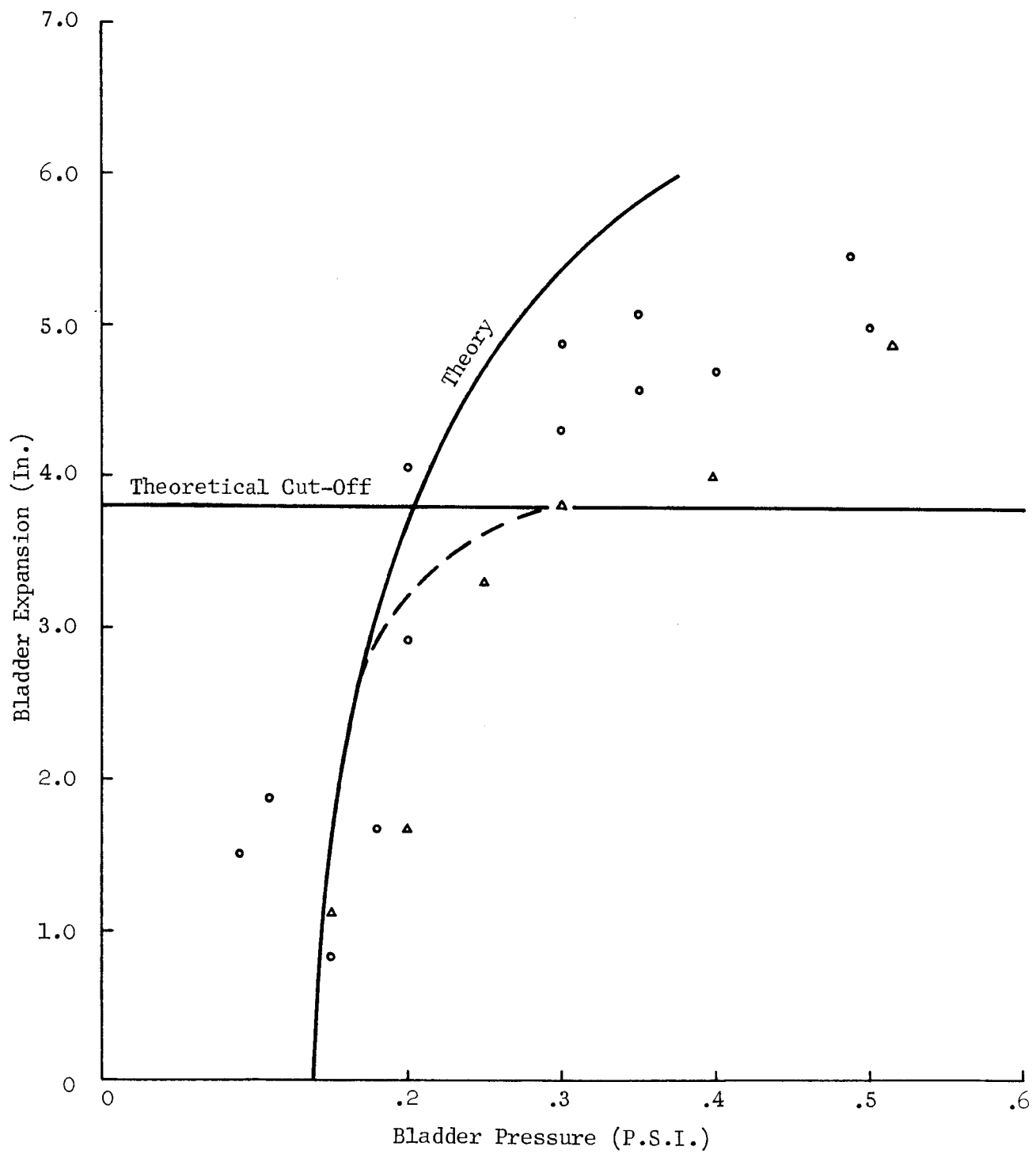
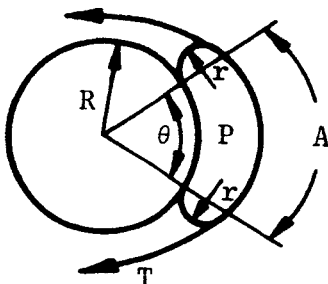


Figure 4.11 Comparison of Theory and Experiment 8" Bladder

$$A = \frac{\theta}{2\pi} (R+2r)h = \theta h (R+2r)$$



Now  $\theta$  may be found from the fact that surface area of the bladder is a constant so that

$$A_T = 2\pi r_o h = \theta h (R+2r) + \theta R h$$

or

$$\theta = \frac{\pi (r_o - r)}{R + r}$$

$$\therefore A = \frac{h (R + 2r) \pi (r_o - r)}{R + r}$$

The force exerted by the tension in the loading medium must be counteracted by the pressure,  $P$ , in the bladder acting over area  $A$  . .

$$PA = 2T = \text{const.}$$

One additional limitation on  $\theta$  exists, however, in that the bladder is taped to the main torus over a reasonably large area so that full expansion is not possible.

In the case of the six inch diameter tube, the minimum value that  $\theta$  can attain is  $2/3$  rad. resulting in a maximum bladder diameter of 2.8 inches as shown by the rapid "tailing off" of the  $P$  vs  $d$  curve in Figure 4.10. A similar analysis shows that the maximum diameter for the eight inch bladder should be 3.81 inches. These lines are shown as theoretical cut-off lines in Figures 4.10 and 4.11. Of course, the bladder will not be in the assumed shape throughout its expansion. Thus the agreement between experiment and theory is expected primarily as low pressures. Also, it is probable that readings will be obtained above the

theoretical limit. Also,  $2T$  was taken as 100 lbs. throughout the tests. The pressure in the main torus was maintained at 1.0 psi.

The agreement between theory and experiment is excellent for the six inch bladder and is fairly good for the eight inch bladder. A good deal more difficulty was encountered in obtaining the latter data due to the difficulty in keeping the bladder from rotating as the load membrane was adjusted. This difficulty is not expected in the actual torus, partly because the hoop stresses on the inflating bladder will tend to make it maintain its position and partly because frictional forces between the bladder and segment material are expected to be much smaller.

It is expected, therefore, that theory will provide a reasonably accurate representation of bladder pressure vs expansion.

The eight inch diameter bladder was adopted for use in the torus itself since the pressure vs expansion curve will remain in the near-linear range over the 3 inch expansion desired.

## 5. INSTRUMENTATION

The instrumentation at the radome facility was designed for the measurement of large pressurized segments. The four systems which comprise the facility instrumentation are:

- (1) R. F. System
- (2) Pressure monitoring System
- (3) Positioning system
- (4) Bistatic Cart

A block diagram of the instrumentation is shown in Figure 5.1.

### 5.1 R. F. System

The R. F. system consists of a setup for measuring the amount of energy which is reflected from the front side of the segment, and a setup for measuring the amount of energy which is transmitted through the segment.

The reflection measurement setup is considerably different from the one discussed in Section 3.4 above. No balancing network is required for measuring segment reflection since the segment radar cross section is the order of 1200 square meters. Therefore, the segment reflection characteristics can be measured with a simple two antenna system as shown in Figure 5.2 below.

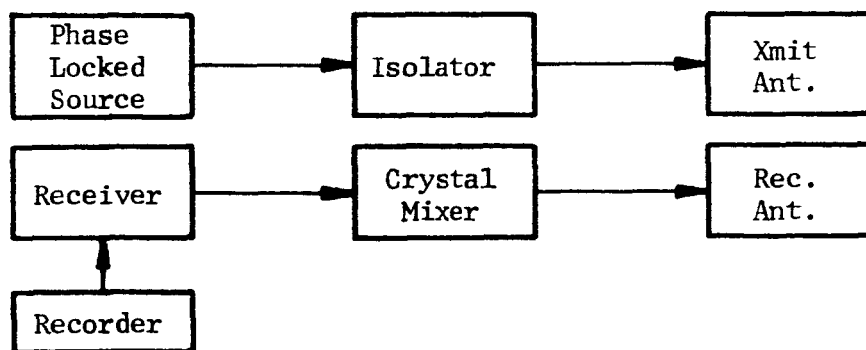


Figure 5.2 Reflection Measurement System

The transmitted antenna is fixed at one end of the bistatic track. The receiving antenna is mounted on a portable tower. The tower rests on rails which extend the length of the bistatic track and is motor driven so that the position of the tower on the bistatic track can be changed remotely. Reflection

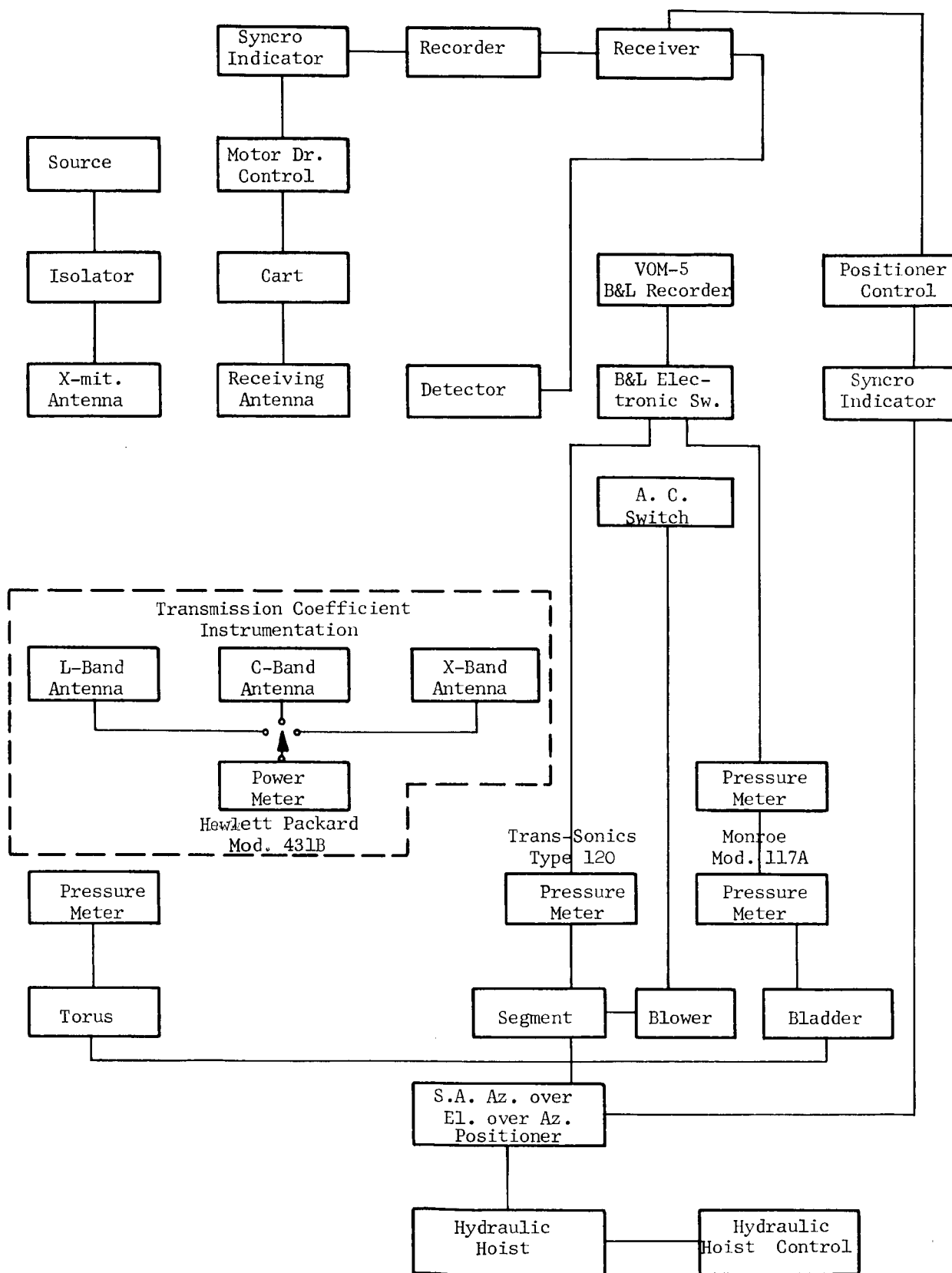


Figure 5.1 Radome Facility Instrumentation

measurements are possible using this antenna system at any bistatic angle from 0 to 30°. The receiving antenna tower is discussed more completely in section 5.4 below. Both reflection and transmission measurements are possible at three different microwave frequencies. L. F. E. Series 814 ultrastable microwave oscillators are used as R.F. sources for all three (L, C, and X) frequency bands. These units have frequency stability of the order of 1 part in  $10^6$ , long term and 3 parts  $10^8$ , short term. The receiving and recording units are the Scientific-Atlanta series 402B and series APR-20 respectively. The specifications for this equipment are shown below.

#### RECEIVER SPECIFICATIONS MODEL 402B

Frequency Coverage	30 mc - 100 kmc
Dynamic Range	40db
Sensitivity	(30 mc - 10 kmc) = - 85 dbm
I.F. Frequency	65 mc
I.F. Bandwidth	1 mc
Linear Deviation of output	0.5 db

#### RECORDER SPECIFICATIONS MODEL APR-20

Pen Writing Speed	= 40 inches/sec.
Pen Accuracy	= 0.25 db
B.W.	= 2% of center frequency @ 3 db
Chart Speed	= 12 inches/sec.
Chart Cycle Length	= 20 inches

The transmission measuring system consists of six standard gain horns, two each for the L, C and X band frequency regions. During operation, one antenna for each of the three bands is inserted into the pressurized compartment at the center of the radome, directly behind the test segment, (see Figure 5.3) thus allowing transmission measurement through the material to be made. The other three antennas are identical to the first, and are used to receive the direct signal from the transmitter, thereby providing the necessary calibration infor-

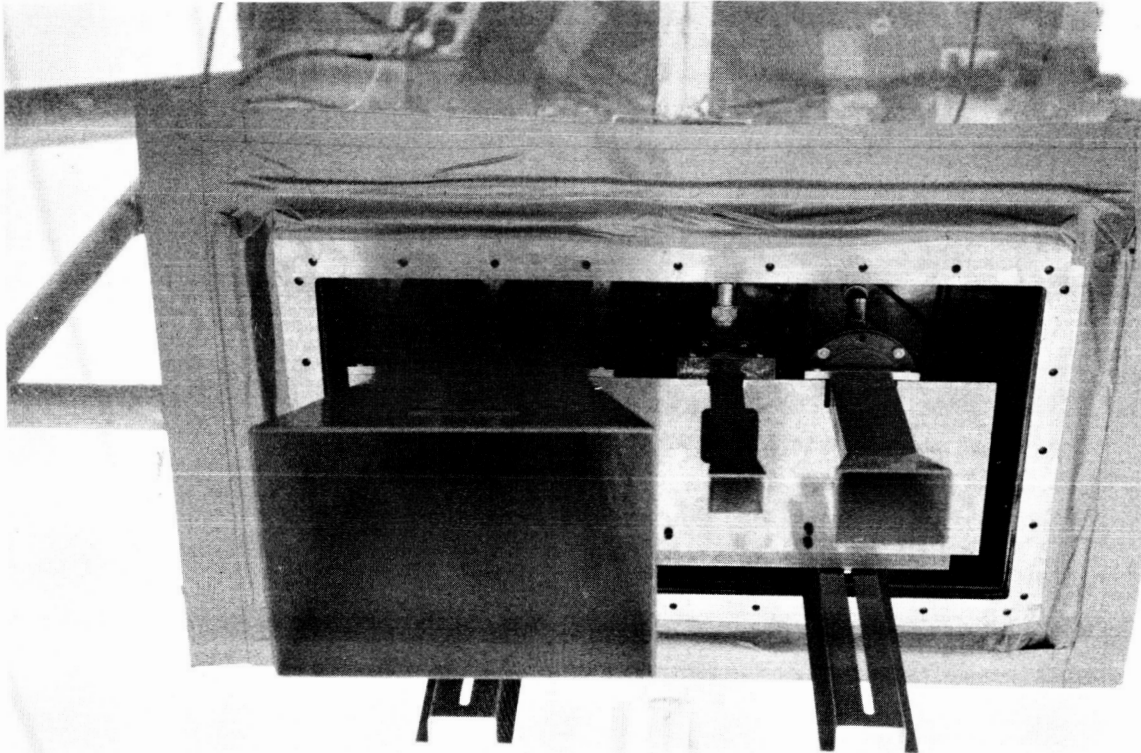


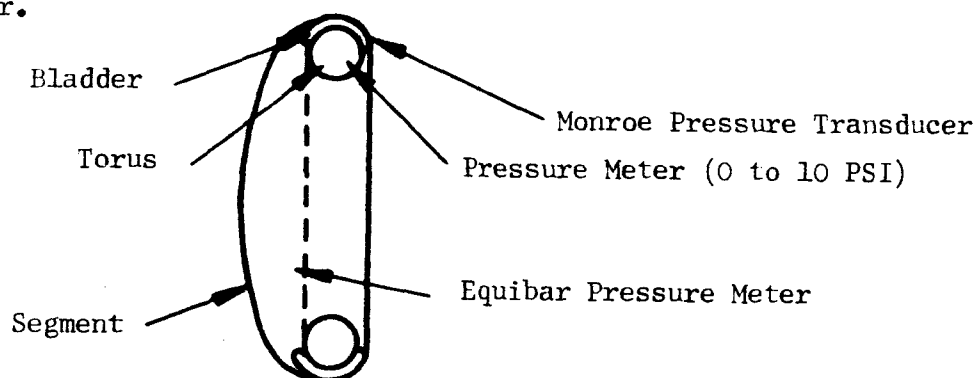
Figure 5.3    Antennas Used for a Transmission Measurements  
as Mounted on the Test Fixture



mation. The power received by the antennas is fed into a Hewlett Packard model 431B power meter which provides a visual indication of the transmitted power.

## 5.2 Pressure Monitoring System

The pressure monitoring equipment consists of one Equibar Type 120 pressure meter, which is used for monitoring segment pressure. One Marsh 0-10 PSI pressure meter which is used to monitor torus pressure, and one Monroe model 117A differential pressure transducer is used to measure the bladder pressure. The outputs of the models 117A and 120 pressure meters are fed to a Bausch and Lomb model VOM-5 recorder.



All of the pressure readings are taken relative to the radome pressure which is maintained at approximately 2.5 inches of water.

## 5.3 Positioning System

The positioning system consists of a 14 foot hydraulic cylinder, and a Scientific Atlanta azimuth over elevation over azimuth positioner.

The hydraulic cylinder can be controlled from within the radome, and provide continuous height adjustment of the segment. When the hydraulic system is in the full down position, the fixture is approximately 4.5 feet above the radome floor and provides an easy working height for segment mounting. This system is discussed more completely in Section 2 above.

The three-axis positioner provides continuous remote control of the targets pitch, roll and azimuth position, and is controlled at the mast control room by means of a Scientific-Atlanta model PC-4 positioner control. A few of the positioners specifications are listed below

Azimuth Accuracy	= $\pm .05^{\circ}$
Elevation Accuracy	= $\pm 0.1^{\circ}$
Azimuth Speed	= 1.5 RPM
Elevation Speed	= $90^{\circ}/\text{Min.}$

1:1 and 36:1 syncros are provided on all three axes of the positioner, to drive the remote position indicator units, and necessary chart drive.

#### 5.4 Bistatic Cart

The bistatic cart is driven by means of a remote controlled  $3/4$  H.P. D.C. motor and a 50:1 gear reduction. The drive motor is controlled by using a Scientific-Atlanta model Pc-4 Positioner Control Unit. The speed of the cart may be continuously adjusted from 0 to approximately 35 feet per minute, thus allowing the  $30^{\circ}$  arc to be transversed in approximately 2.5 minutes. The antenna tower which is mounted on top of the bistatic cart allows continuous antenna height adjustment to approximately 15 feet above ground level. The antenna tower, cart and bistatic track are shown in Figure 5.4.

A 1:1 synchro transmitter is located on the receiver cart and is used to provide the necessary chart drive to the recording and position-indicating equipment. A drawing of the receiver tower is shown in Appendix A.

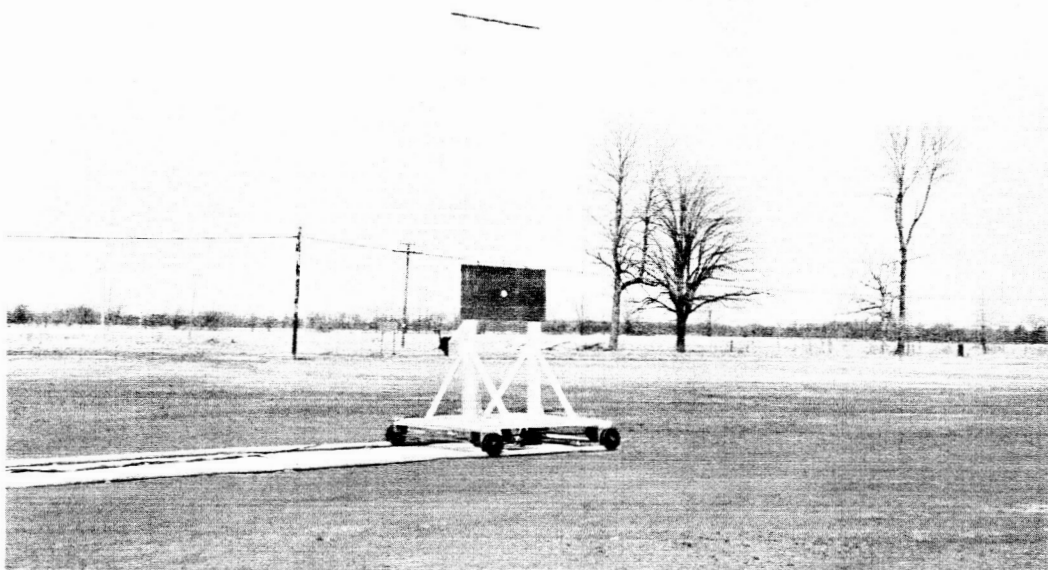
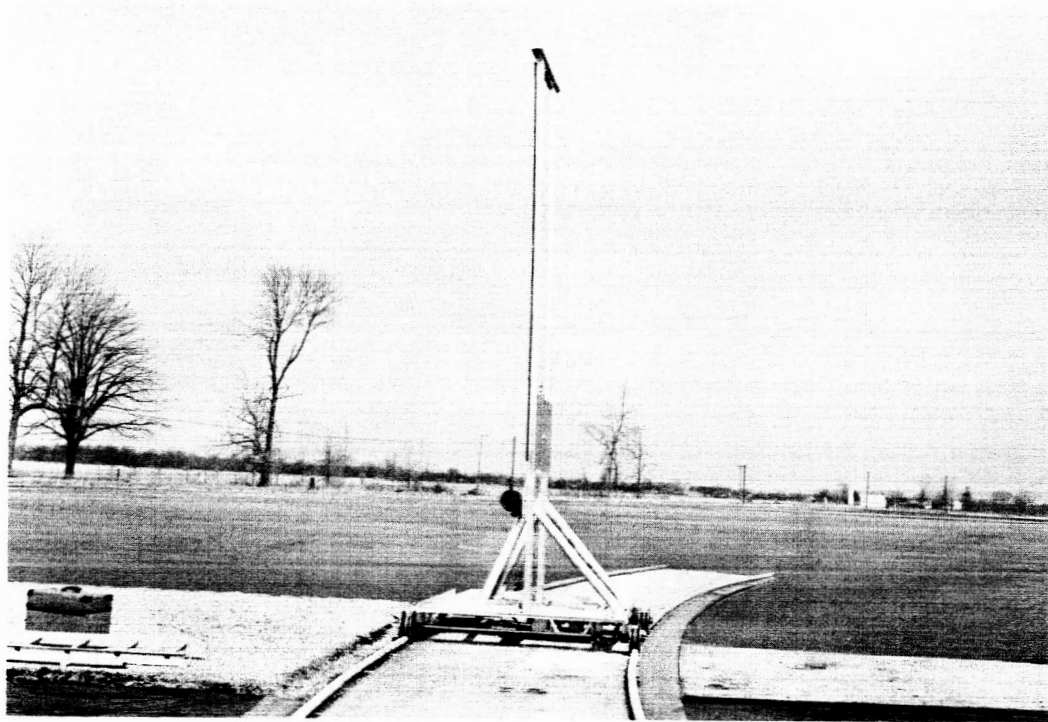
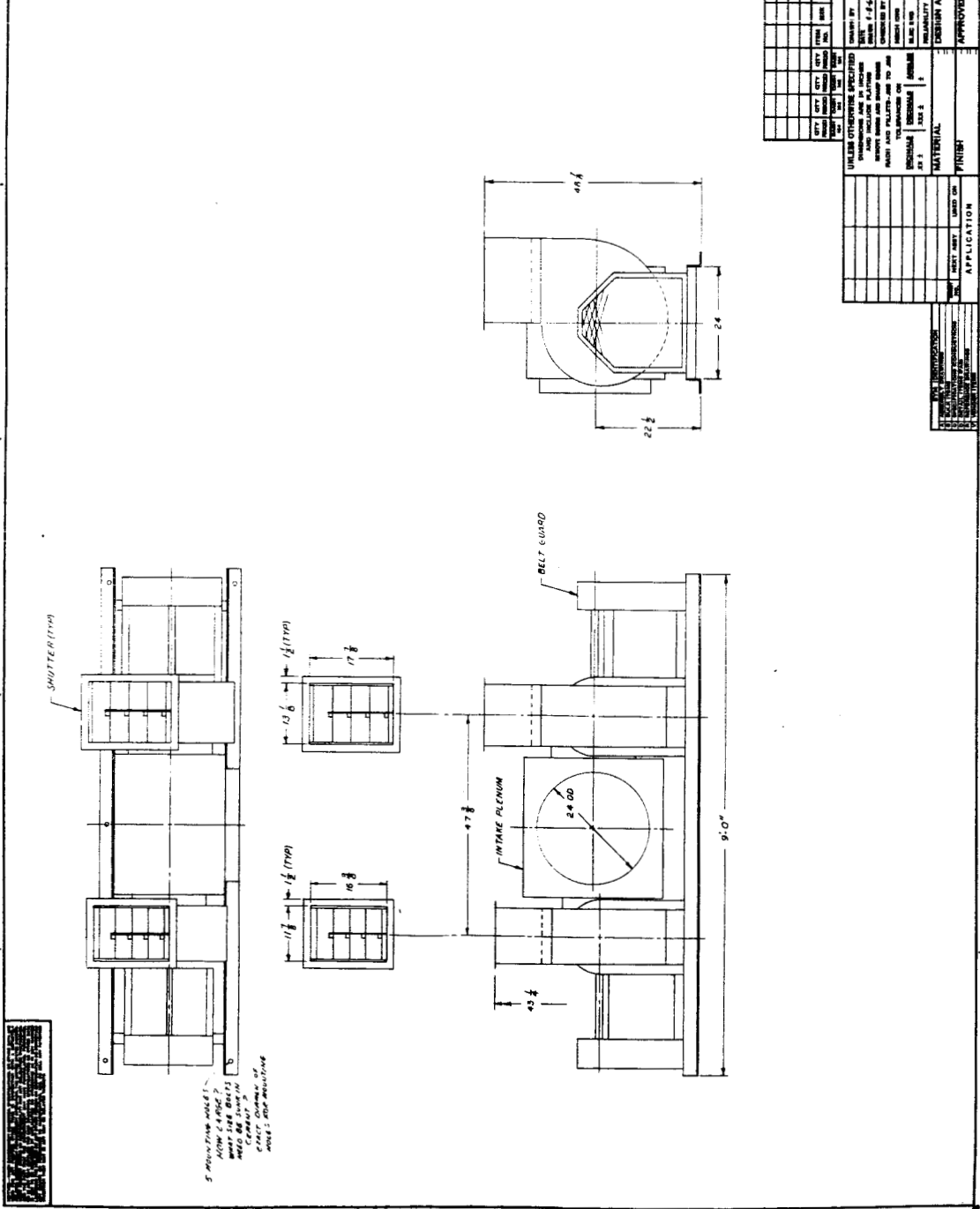


Figure 5.4 Bistatic Cart



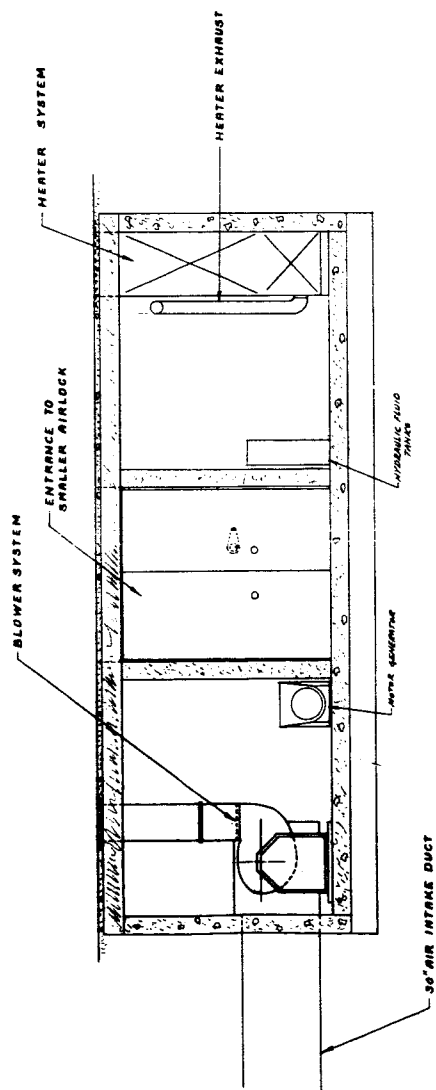
## APPENDIX A - SUPPORT FACILITY DRAWINGS

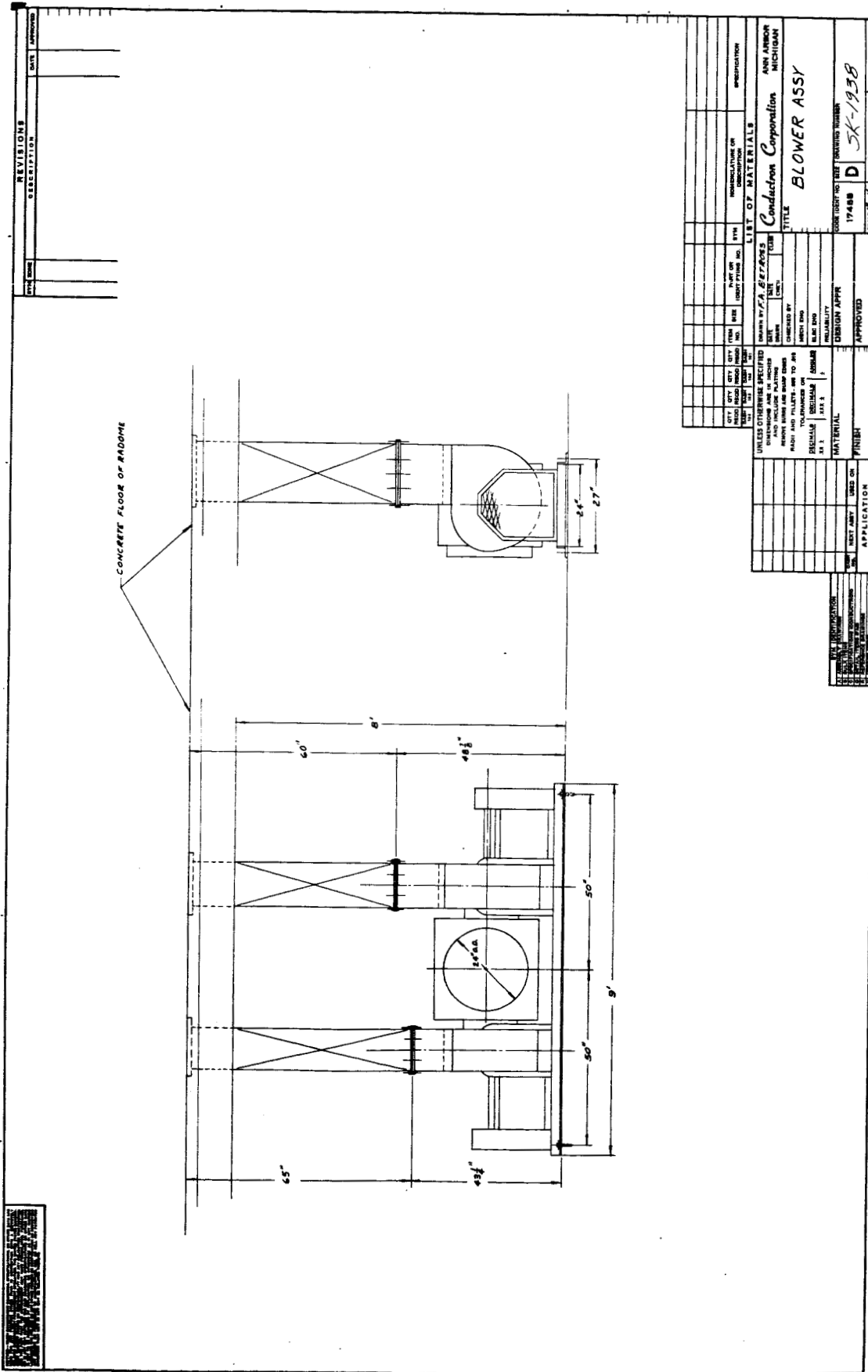
REVISIONS		DATE	APPROVED
	DESCRIPTION		



Blower # 6406-4-6

UNLESS OTHERWISE SPECIFIED		DRAWN BY		G. C. CHEN		TEAM		CONDOR CONSTRUCTION CORPORATION		ANN ARBOR MICHIGAN	
STANDARD AND 1/4" INCHES		DATE		1.1.14		DATE		1.1.14		DATE	
STANDARD AND 1/4" INCHES		CHECKED BY		G. C. CHEN		DATE		1.1.14		DATE	
STANDARD AND 1/4" INCHES		APPROVED BY		G. C. CHEN		DATE		1.1.14		DATE	
STANDARD AND 1/4" INCHES		MATERIAL		CONDOR CONSTRUCTION CORPORATION		ANN ARBOR MICHIGAN		CONDOR CONSTRUCTION CORPORATION		ANN ARBOR MICHIGAN	
STANDARD AND 1/4" INCHES		FINISH		CONDOR CONSTRUCTION CORPORATION		ANN ARBOR MICHIGAN		CONDOR CONSTRUCTION CORPORATION		ANN ARBOR MICHIGAN	
STANDARD AND 1/4" INCHES		APPROVED		CONDOR CONSTRUCTION CORPORATION		ANN ARBOR MICHIGAN		CONDOR CONSTRUCTION CORPORATION		ANN ARBOR MICHIGAN	
STANDARD AND 1/4" INCHES		SCALE		1/8" = 1'-0"		DATE		1.1.14		DATE	
STANDARD AND 1/4" INCHES		SHEET NO.		17408		SHEET NO.		17408		SHEET NO.	
STANDARD AND 1/4" INCHES		TOTAL SHEETS		17408		TOTAL SHEETS		17408		TOTAL SHEETS	

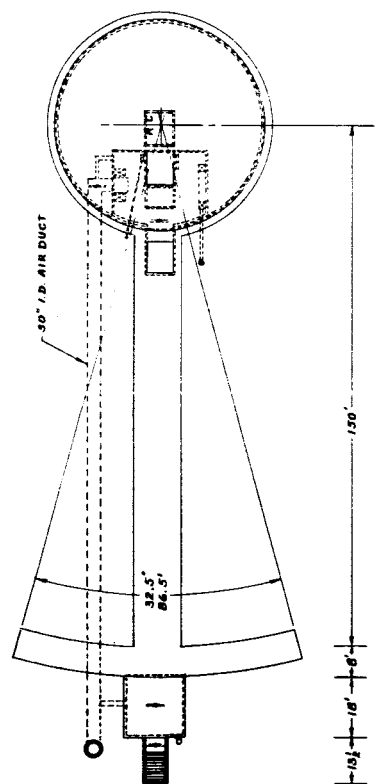
[illegible][illegible]







REVISIONS	
DATE	DESCRIPTION

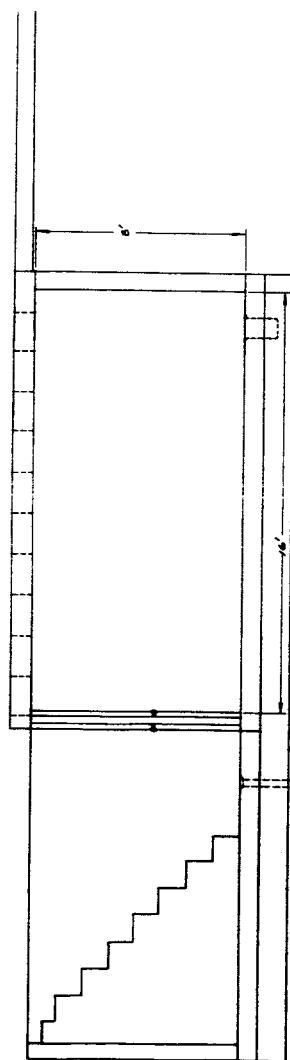


DRAWN BY		DATE		CHECKED BY		DATE		DESIGNED BY		DATE		APPROVED		DATE	
UNLESS OTHERWISE SPECIFIED															
DIMENSIONS ARE IN INCHES															
FRACTIONS ARE TO BE SHOWN															
RADI AND FILLETS - 1/8\"/>															





REVISIONS	
NO.	DESCRIPTION
1	AS SHOWN



FOOTING - 20" WIDE x 18" DEEP REINFORCED WITH TWO #4 BARS. 2500 PSI CONCRETE

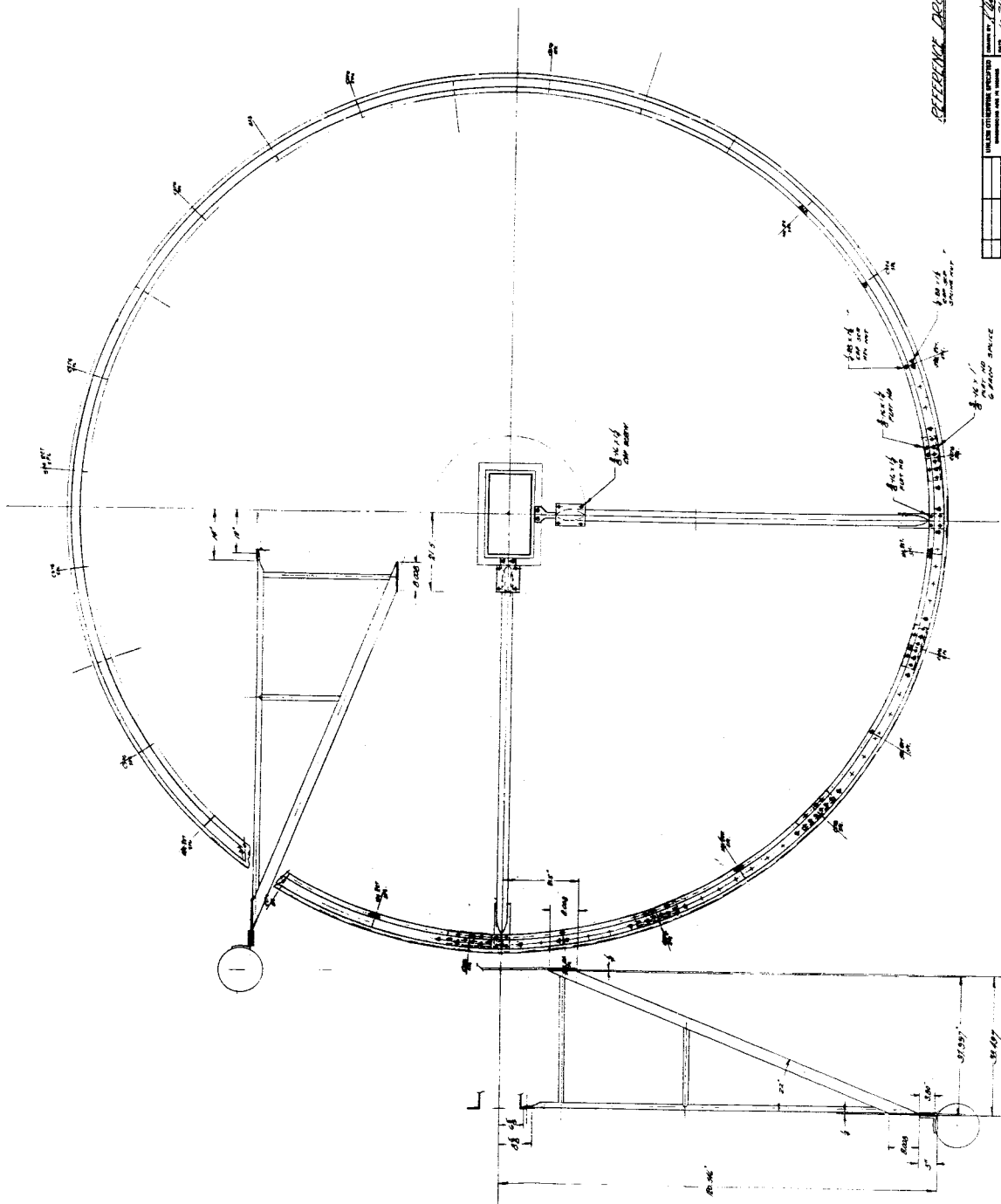
DESIGNER'S NAME F. J. MATTHEWS		DATE 1/15/45		PROJECT NO. 17488		SHEET NO. 1	
OWNER'S NAME Conduction Corporation		LOCATION ANN ARBOR MICHIGAN		TITLE CONTROL ROOM		SCALE 1/4" = 1'-0"	
DESIGNED BY F. J. MATTHEWS		CHECKED BY F. J. MATTHEWS		APPROVED BY F. J. MATTHEWS		DATE 1/15/45	
MATERIAL CONCRETE		FINISH AS SHOWN		APPLICATION CONTROL ROOM		REMARKS SEE SHEET 2	

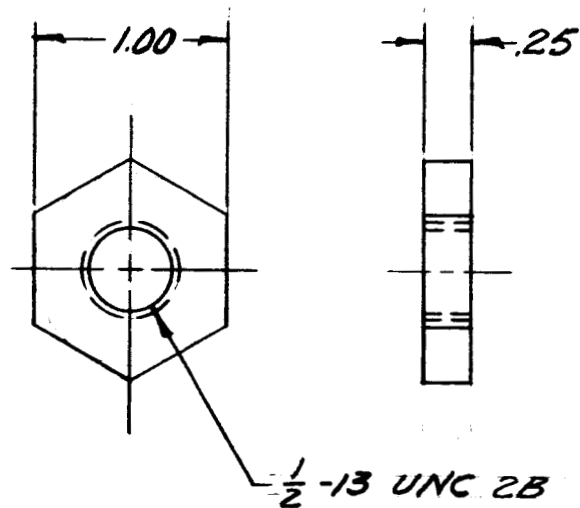
LIST OF MATERIALS	
QTY	DESCRIPTION
1	CONCRETE
1	REINFORCEMENT





## APPENDIX B - TEST FIXTURE DRAWINGS

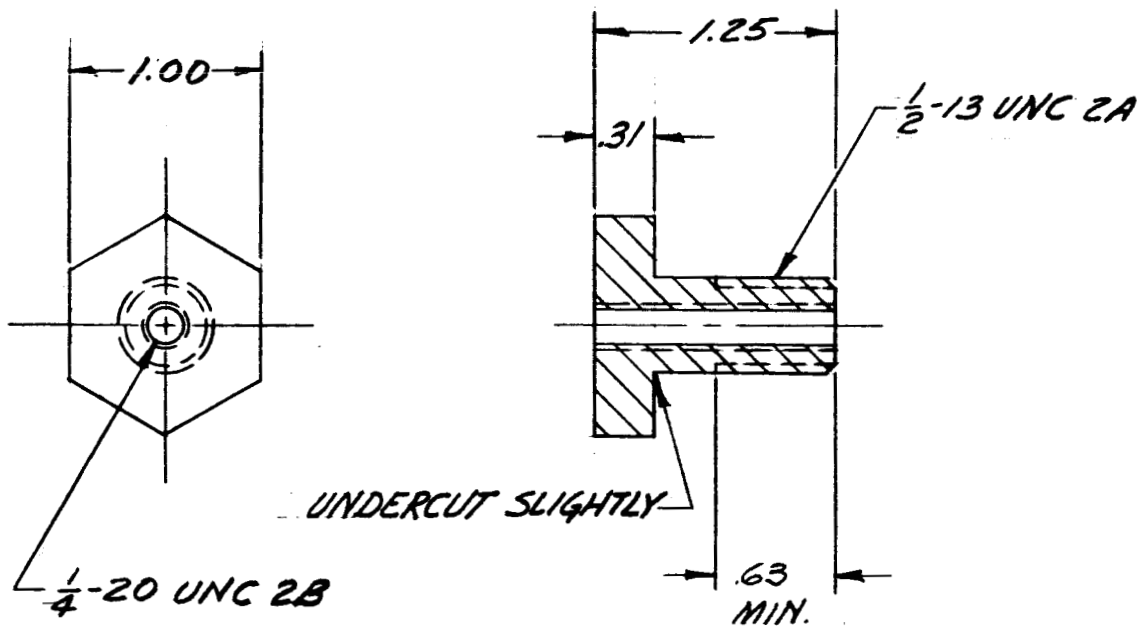
[illegible]



PART NO. 122398-1

<b>Conductron Corporation</b>		ANN ARBOR MICHIGAN
TITLE <i>NUT</i>		
CODE IDENT NO. <b>17468</b>	SIZE <b>B</b>	DRAWING NUMBER <i>122398</i>
SCALE <i>1:1</i>	WEIGHT	SHEET





PART NO. 122399-1

Conductron Corporation		ANN ARBOR MICHIGAN
TITLE NUT, RETAINING		
CODE IDENT NO. 17468	SIZE B	DRAWING NUMBER 122399
SCALE 1:1	WEIGHT	SHEET





PART NO. 122401-1



[illegible]





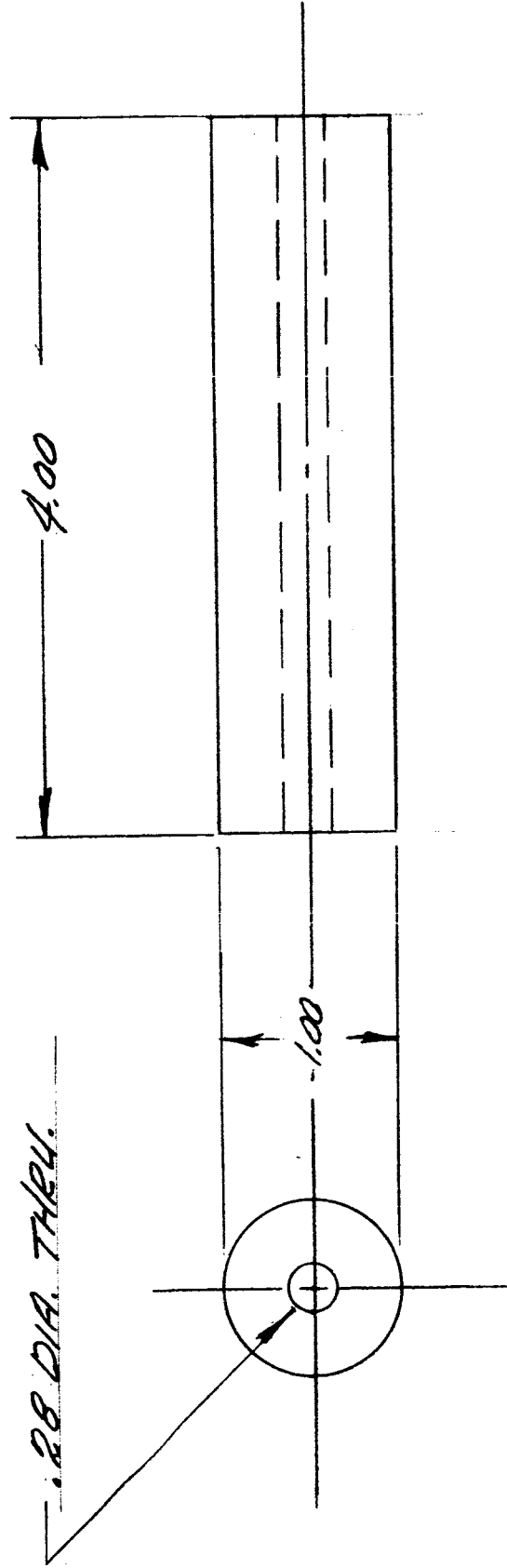




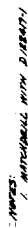








Conduction Corporation		ANN ARBOR MICHIGAN	
TITLE HANDLE - CRANK			
CODE IDENT NO.	SIZE	DRAWING NUMBER	
17468	B	122409	
SCALE	WEIGHT	SHEET	

[illegible]

REVISIONS		DATE	APPROVED
1	REVISION		
2			
3			
4			
5			

WELDED STEEL  
CORNERS WITH SHIMS

4 CORNERS

4 CORNERS

4 CORNERS

4 CORNERS

4 CORNERS

4 CORNERS

4 CORNERS

4 CORNERS

4 CORNERS

4 CORNERS

4 CORNERS

4 CORNERS

4 CORNERS

4 CORNERS

4 CORNERS

4 CORNERS

4 CORNERS

4 CORNERS

4 CORNERS

4 CORNERS

4 CORNERS

4 CORNERS

4 CORNERS

4 CORNERS

4 CORNERS

4 CORNERS

4 CORNERS

17.50' x 20.00'

20.00' x 20.00'

20.00' x 20.00'

20.00' x 20.00'

NOTES: 1. MATERIALS TO BE USED AS SHOWN.

FIG. NO. 122417-1

LIST OF MATERIALS		APPROVED	
NO.	DESCRIPTION	DATE	BY
1	STEEL PLATE, 1/2" THICK	1/15/78	ANN ARBOR
2	STEEL PLATE, 1/4" THICK	1/15/78	ANN ARBOR
3	STEEL PLATE, 1/8" THICK	1/15/78	ANN ARBOR
4	STEEL PLATE, 1/16" THICK	1/15/78	ANN ARBOR
5	STEEL PLATE, 1/32" THICK	1/15/78	ANN ARBOR
6	STEEL PLATE, 1/64" THICK	1/15/78	ANN ARBOR
7	STEEL PLATE, 1/128" THICK	1/15/78	ANN ARBOR
8	STEEL PLATE, 1/256" THICK	1/15/78	ANN ARBOR
9	STEEL PLATE, 1/512" THICK	1/15/78	ANN ARBOR
10	STEEL PLATE, 1/1024" THICK	1/15/78	ANN ARBOR
11	STEEL PLATE, 1/2048" THICK	1/15/78	ANN ARBOR
12	STEEL PLATE, 1/4096" THICK	1/15/78	ANN ARBOR
13	STEEL PLATE, 1/8192" THICK	1/15/78	ANN ARBOR
14	STEEL PLATE, 1/16384" THICK	1/15/78	ANN ARBOR
15	STEEL PLATE, 1/32768" THICK	1/15/78	ANN ARBOR
16	STEEL PLATE, 1/65536" THICK	1/15/78	ANN ARBOR
17	STEEL PLATE, 1/131072" THICK	1/15/78	ANN ARBOR
18	STEEL PLATE, 1/262144" THICK	1/15/78	ANN ARBOR
19	STEEL PLATE, 1/524288" THICK	1/15/78	ANN ARBOR
20	STEEL PLATE, 1/1048576" THICK	1/15/78	ANN ARBOR
21	STEEL PLATE, 1/2097152" THICK	1/15/78	ANN ARBOR
22	STEEL PLATE, 1/4194304" THICK	1/15/78	ANN ARBOR
23	STEEL PLATE, 1/8388608" THICK	1/15/78	ANN ARBOR
24	STEEL PLATE, 1/16777216" THICK	1/15/78	ANN ARBOR
25	STEEL PLATE, 1/33554432" THICK	1/15/78	ANN ARBOR
26	STEEL PLATE, 1/67108864" THICK	1/15/78	ANN ARBOR
27	STEEL PLATE, 1/134217728" THICK	1/15/78	ANN ARBOR
28	STEEL PLATE, 1/268435456" THICK	1/15/78	ANN ARBOR
29	STEEL PLATE, 1/536870912" THICK	1/15/78	ANN ARBOR
30	STEEL PLATE, 1/1073741824" THICK	1/15/78	ANN ARBOR
31	STEEL PLATE, 1/2147483648" THICK	1/15/78	ANN ARBOR
32	STEEL PLATE, 1/4294967296" THICK	1/15/78	ANN ARBOR
33	STEEL PLATE, 1/8589934592" THICK	1/15/78	ANN ARBOR
34	STEEL PLATE, 1/17179869184" THICK	1/15/78	ANN ARBOR
35	STEEL PLATE, 1/34359738368" THICK	1/15/78	ANN ARBOR
36	STEEL PLATE, 1/68719476736" THICK	1/15/78	ANN ARBOR
37	STEEL PLATE, 1/137438953472" THICK	1/15/78	ANN ARBOR
38	STEEL PLATE, 1/274877907344" THICK	1/15/78	ANN ARBOR
39	STEEL PLATE, 1/549755814688" THICK	1/15/78	ANN ARBOR
40	STEEL PLATE, 1/1099511629376" THICK	1/15/78	ANN ARBOR
41	STEEL PLATE, 1/2199023258752" THICK	1/15/78	ANN ARBOR
42	STEEL PLATE, 1/4398046517504" THICK	1/15/78	ANN ARBOR
43	STEEL PLATE, 1/8796093035008" THICK	1/15/78	ANN ARBOR
44	STEEL PLATE, 1/17592186070016" THICK	1/15/78	ANN ARBOR
45	STEEL PLATE, 1/35184372140032" THICK	1/15/78	ANN ARBOR
46	STEEL PLATE, 1/70368744280064" THICK	1/15/78	ANN ARBOR
47	STEEL PLATE, 1/140737488560128" THICK	1/15/78	ANN ARBOR
48	STEEL PLATE, 1/281474977120256" THICK	1/15/78	ANN ARBOR
49	STEEL PLATE, 1/562949954240512" THICK	1/15/78	ANN ARBOR
50	STEEL PLATE, 1/1125899908481024" THICK	1/15/78	ANN ARBOR
51	STEEL PLATE, 1/2251799816962048" THICK	1/15/78	ANN ARBOR
52	STEEL PLATE, 1/4503599633924096" THICK	1/15/78	ANN ARBOR
53	STEEL PLATE, 1/9007199267848192" THICK	1/15/78	ANN ARBOR
54	STEEL PLATE, 1/18014398535696384" THICK	1/15/78	ANN ARBOR
55	STEEL PLATE, 1/36028797071392768" THICK	1/15/78	ANN ARBOR
56	STEEL PLATE, 1/72057594142785536" THICK	1/15/78	ANN ARBOR
57	STEEL PLATE, 1/144115188285571072" THICK	1/15/78	ANN ARBOR
58	STEEL PLATE, 1/288230376571142144" THICK	1/15/78	ANN ARBOR
59	STEEL PLATE, 1/576460753142284288" THICK	1/15/78	ANN ARBOR
60	STEEL PLATE, 1/1152921506284568576" THICK	1/15/78	ANN ARBOR
61	STEEL PLATE, 1/2305843012569137152" THICK	1/15/78	ANN ARBOR
62	STEEL PLATE, 1/4611686025138274304" THICK	1/15/78	ANN ARBOR
63	STEEL PLATE, 1/9223372050276548608" THICK	1/15/78	ANN ARBOR
64	STEEL PLATE, 1/18446744100553097216" THICK	1/15/78	ANN ARBOR
65	STEEL PLATE, 1/36893488201106194432" THICK	1/15/78	ANN ARBOR
66	STEEL PLATE, 1/73786976402212388864" THICK	1/15/78	ANN ARBOR
67	STEEL PLATE, 1/14757395280444777728" THICK	1/15/78	ANN ARBOR
68	STEEL PLATE, 1/29514790560889555456" THICK	1/15/78	ANN ARBOR
69	STEEL PLATE, 1/59029581121779110912" THICK	1/15/78	ANN ARBOR
70	STEEL PLATE, 1/118059162243558221824" THICK	1/15/78	ANN ARBOR
71	STEEL PLATE, 1/236118324487116443648" THICK	1/15/78	ANN ARBOR
72	STEEL PLATE, 1/472236648974232887296" THICK	1/15/78	ANN ARBOR
73	STEEL PLATE, 1/944473297948465774592" THICK	1/15/78	ANN ARBOR
74	STEEL PLATE, 1/1888946595896931549184" THICK	1/15/78	ANN ARBOR
75	STEEL PLATE, 1/3777893191793863098368" THICK	1/15/78	ANN ARBOR
76	STEEL PLATE, 1/7555786383587726196736" THICK	1/15/78	ANN ARBOR
77	STEEL PLATE, 1/15111572767175452393472" THICK	1/15/78	ANN ARBOR
78	STEEL PLATE, 1/30223145534350904786944" THICK	1/15/78	ANN ARBOR
79	STEEL PLATE, 1/60446291068701809573888" THICK	1/15/78	ANN ARBOR
80	STEEL PLATE, 1/120892582137403619147776" THICK	1/15/78	ANN ARBOR
81	STEEL PLATE, 1/241785164274807238295552" THICK	1/15/78	ANN ARBOR
82	STEEL PLATE, 1/483570328549614476591104" THICK	1/15/78	ANN ARBOR
83	STEEL PLATE, 1/967140657099228953182208" THICK	1/15/78	ANN ARBOR
84	STEEL PLATE, 1/1934281314198457906364416" THICK	1/15/78	ANN ARBOR
85	STEEL PLATE, 1/3868562628396915812728832" THICK	1/15/78	ANN ARBOR
86	STEEL PLATE, 1/7737125256793831625457664" THICK	1/15/78	ANN ARBOR
87	STEEL PLATE, 1/15474250513587663250915328" THICK	1/15/78	ANN ARBOR
88	STEEL PLATE, 1/30948501027175326501830656" THICK	1/15/78	ANN ARBOR
89	STEEL PLATE, 1/61897002054350653003661312" THICK	1/15/78	ANN ARBOR
90	STEEL PLATE, 1/123794004108701306007322624" THICK	1/15/78	ANN ARBOR
91	STEEL PLATE, 1/247588008217402612014645248" THICK	1/15/78	ANN ARBOR
92	STEEL PLATE, 1/495176016434805224029290496" THICK	1/15/78	ANN ARBOR
93	STEEL PLATE, 1/990352032869610448058580992" THICK	1/15/78	ANN ARBOR
94	STEEL PLATE, 1/1980704065739220896117161984" THICK	1/15/78	ANN ARBOR
95	STEEL PLATE, 1/3961408131478441792234323968" THICK	1/15/78	ANN ARBOR
96	STEEL PLATE, 1/7922816262956883584468647936" THICK	1/15/78	ANN ARBOR
97	STEEL PLATE, 1/15845632525913767168937295872" THICK	1/15/78	ANN ARBOR
98	STEEL PLATE, 1/31691265051827534337874591744" THICK	1/15/78	ANN ARBOR
99	STEEL PLATE, 1/63382530103655068675749183488" THICK	1/15/78	ANN ARBOR
100	STEEL PLATE, 1/126765060207310137351498366976" THICK	1/15/78	ANN ARBOR

122417

D

17488

DATE

1/15/78

ANN ARBOR

ANN ARBOR

ANN ARBOR

ANN ARBOR

ANN ARBOR

ANN ARBOR

ANN ARBOR

ANN ARBOR

ANN ARBOR

ANN ARBOR

ANN ARBOR

ANN ARBOR

ANN ARBOR

ANN ARBOR

ANN ARBOR

ANN ARBOR

ANN ARBOR

ANN ARBOR

ANN ARBOR

ANN ARBOR

ANN ARBOR

ANN ARBOR

ANN ARBOR

ANN ARBOR

ANN ARBOR

ANN ARBOR

ANN ARBOR

ANN ARBOR

ANN ARBOR

ANN ARBOR

ANN ARBOR

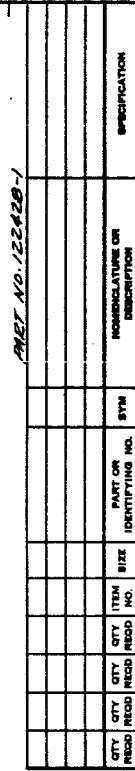
ANN ARBOR

ANN ARBOR

ANN ARBOR

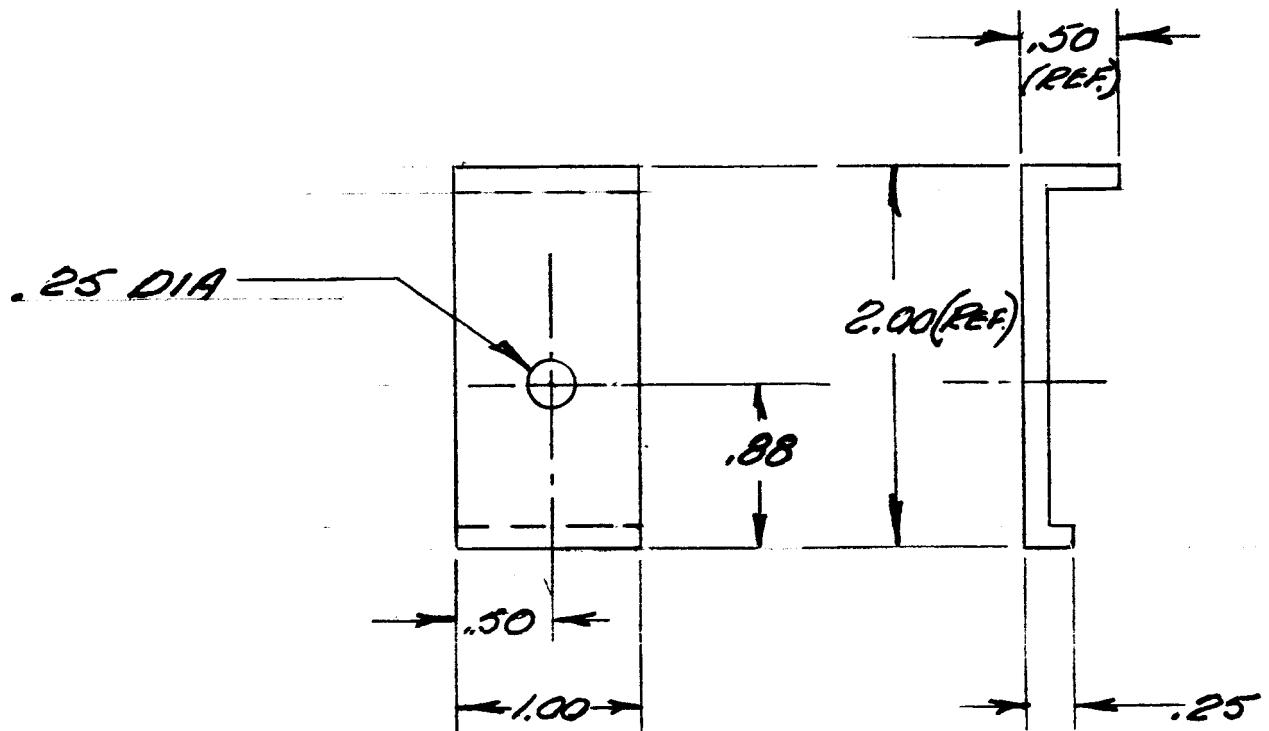
ANN ARBOR

ANN ARBOR

[illegible][illegible]

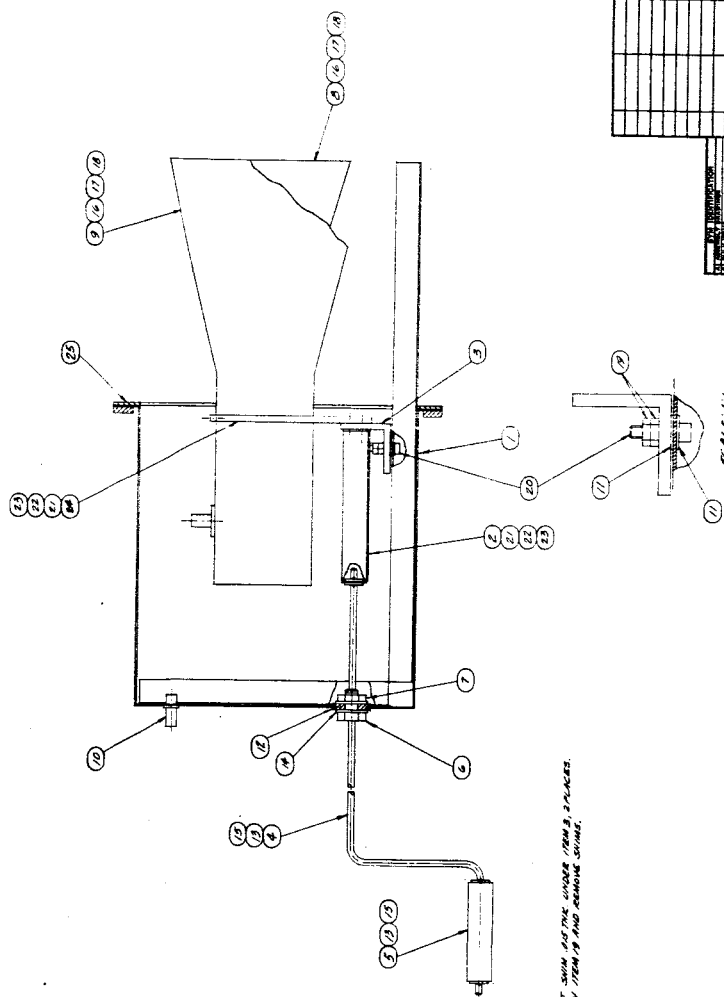






Conductron Corporation		ANN ARBOR MICHIGAN
TITLE CLAMP CHANNEL		
CODE IDENT NO. 17468	SIZE B	DRAWING NUMBER 122431
SCALE 1:1	WEIGHT	SHEET

[illegible]



NOTES:

1. INSERT SWIM PAST THE UNDER ITEM 3, 2 PLACES.  
TWENTY ITEM 19 AND REMOVE SWIMS.

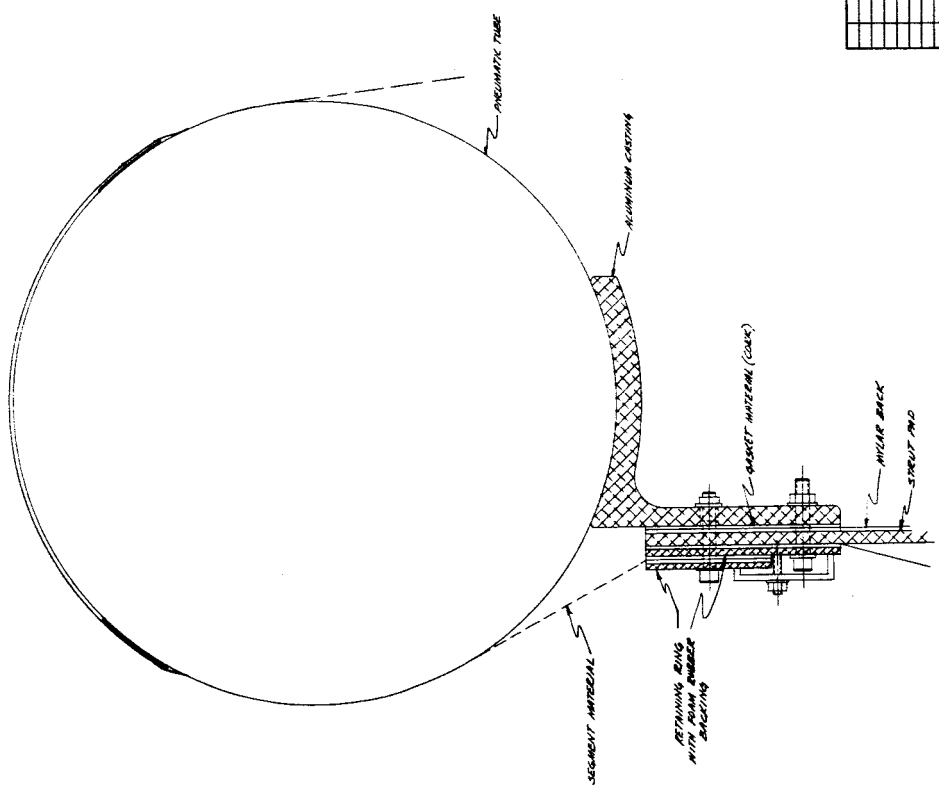
REVISIONS			
DATE	DESCRIPTION	DATE	APPROVED
1	ORIGINAL DRAWING TO THESE STANDARDS	10/1/82	

DATE	TIME	LOCATION	TYPE	DESCRIPTION	REMARKS
1	10:00	1000	1000	1000	1000
2	10:00	1000	1000	1000	1000
3	10:00	1000	1000	1000	1000
4	10:00	1000	1000	1000	1000
5	10:00	1000	1000	1000	1000
6	10:00	1000	1000	1000	1000
7	10:00	1000	1000	1000	1000
8	10:00	1000	1000	1000	1000
9	10:00	1000	1000	1000	1000
10	10:00	1000	1000	1000	1000
11	10:00	1000	1000	1000	1000
12	10:00	1000	1000	1000	1000
13	10:00	1000	1000	1000	1000
14	10:00	1000	1000	1000	1000
15	10:00	1000	1000	1000	1000
16	10:00	1000	1000	1000	1000
17	10:00	1000	1000	1000	1000
18	10:00	1000	1000	1000	1000
19	10:00	1000	1000	1000	1000
20	10:00	1000	1000	1000	1000
21	10:00	1000	1000	1000	1000
22	10:00	1000	1000	1000	1000
23	10:00	1000	1000	1000	1000
24	10:00	1000	1000	1000	1000
25	10:00	1000	1000	1000	1000
26	10:00	1000	1000	1000	1000
27	10:00	1000	1000	1000	1000
28	10:00	1000	1000	1000	1000
29	10:00	1000	1000	1000	1000
30	10:00	1000	1000	1000	1000
31	10:00	1000	1000	1000	1000
32	10:00	1000	1000	1000	1000
33	10:00	1000	1000	1000	1000
34	10:00	1000	1000	1000	1000
35	10:00	1000	1000	1000	1000
36	10:00	1000	1000	1000	1000
37	10:00	1000	1000	1000	1000
38	10:00	1000	1000	1000	1000
39	10:00	1000	1000	1000	1000
40	10:00	1000	1000	1000	1000
41	10:00	1000	1000	1000	1000
42	10:00	1000	1000	1000	1000
43	10:00	1000	1000	1000	1000
44	10:00	1000	1000	1000	1000
45	10:00	1000	1000	1000	1000
46	10:00	1000	1000	1000	1000
47	10:00	1000	1000	1000	1000
48	10:00	1000	1000	1000	1000
49	10:00	1000	1000	1000	1000
50	10:00	1000	1000	1000	1000
51	10:00	1000	1000	1000	1000
52	10:00	1000	1000	1000	1000
53	10:00	1000	1000	1000	1000
54	10:00	1000	1000	1000	1000
55	10:00	1000	1000	1000	1000
56	10:00	1000	1000	1000	1000
57	10:00	1000	1000	1000	1000
58	10:00	1000	1000	1000	1000
59	10:00	1000	1000	1000	1000
60	10:00	1000	1000	1000	1000
61	10:00	1000	1000	1000	1000
62	10:00	1000	1000	1000	1000
63	10:00	1000	1000	1000	1000
64	10:00	1000	1000	1000	1000
65	10:00	1000	1000	1000	1000
66	10:00	1000	1000	1000	1000
67	10:00	1000	1000	1000	1000
68	10:00	1000	1000	1000	1000
69	10:00	1000	1000	1000	1000
70	10:00	1000	1000	1000	1000
71	10:00	1000	1000	1000	1000
72	10:00	1000	1000	1000	1000
73	10:00	1000	1000	1000	1000
74	10:00	1000	1000	1000	1000
75	10:00	1000	1000	1000	1000
76	10:00	1000	1000	1000	1000
77	10:00	1000	1000	1000	1000
78	10:00	1000	1000	1000	1000
79	10:00	1000	1000	1000	1000
80	10:00	1000	1000	1000	1000
81	10:00	1000	1000	1000	1000
82	10:00	1000	1000	1000	1000
83	10:00	1000	1000	1000	1000
84	10:00	1000	1000	1000	1000
85	10:00	1000	1000	1000	1000
86	10:00	1000	1000	1000	1000
87	10:00	1000	1000	1000	1000
88	10:00	1000	1000	1000	1000
89	10:00	1000	1000	1000	1000
90	10:00	1000	1000	1000	1000
91	10:00	1000	1000	1000	1000
92	10:00	1000	1000	1000	1000
93	10:00	1000	1000	1000	1000
94	10:00	1000	1000	1000	1000
95	10:00	1000	1000	1000	1000
96	10:00	1000	1000	1000	1000
97	10:00	1000	1000	1000	1000
98	10:00	1000	1000	1000	1000
99	10:00	1000	1000	1000	1000
100	10:00	1000	1000	1000	1000

[illegible]



REVISIONS	
DATE	DESCRIPTION

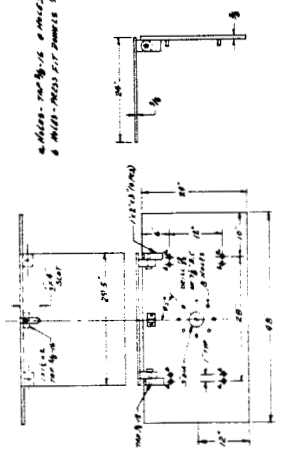


DRAWN BY: <i>A. SIMPSON</i>		CHECKED BY: <i>[Signature]</i>	
DATE: <i>10/1/54</i>		DATE: <i>10/1/54</i>	
SYMBOL NO.:		SYMBOL NO.:	
PART OR IDENTIFICATION NO.:		PART OR IDENTIFICATION NO.:	
QUANTITY:		QUANTITY:	
MATERIAL:		MATERIAL:	
FINISH:		FINISH:	
APPLICATION:		APPLICATION:	
DESIGN APPROV.:		DESIGN APPROV.:	
APPROVED:		APPROVED:	
SCALE: <i>1/1</i>		SCALE: <i>1/1</i>	
WORK:		WORK:	

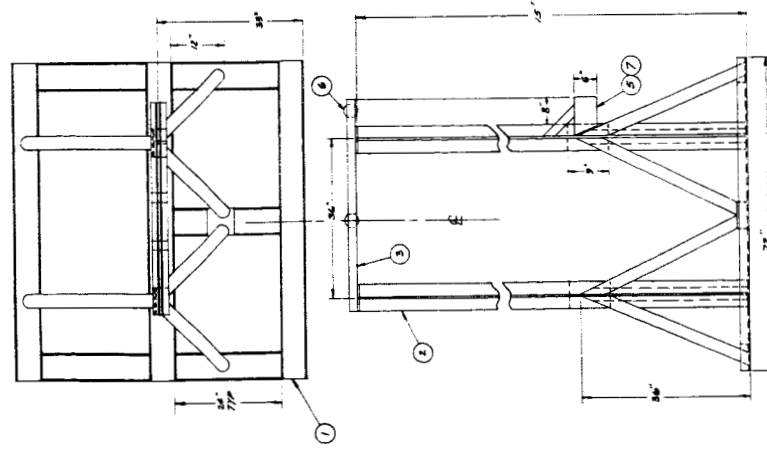
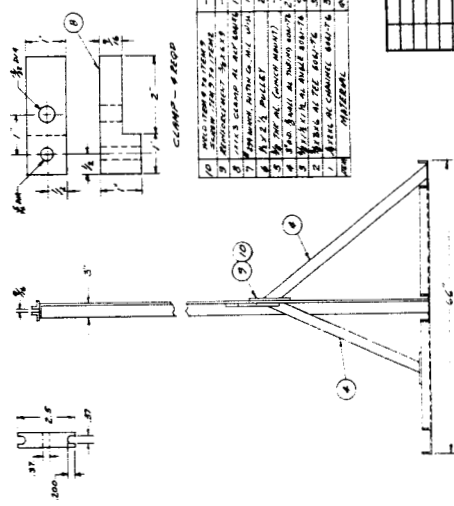
ANN ARBOR  
 CONDUCTRON CORPORATION  
 MICHIGAN  
 TITLE: *PRESSURE SEAL ASSY*  
 17488  
 124205

REVISIONS		DATE	APPROVED
	DESCRIPTION		

ALL DIMENSIONS IN INCHES  
UNLESS OTHERWISE SPECIFIED



ANTENNA MOUNTING PLATE - 1800



LIST OF MATERIALS	
QTY	DESCRIPTION
1	ANTENNA TOWER 1800
1	ANTENNA MOUNTING PLATE 1800
1	ANTENNA MAST 1800
1	ANTENNA CLAMP 1800
1	ANTENNA BRACKET 1800
1	ANTENNA SUPPORT 1800
1	ANTENNA BASE 1800
1	ANTENNA TOWER 1800
1	ANTENNA MOUNTING PLATE 1800
1	ANTENNA MAST 1800
1	ANTENNA CLAMP 1800
1	ANTENNA BRACKET 1800
1	ANTENNA SUPPORT 1800
1	ANTENNA BASE 1800

UNLESS OTHERWISE SPECIFIED	
DESIGNED BY	CONSTRUCTION CORPORATION
CHECKED BY	ANN ANDOR
DATE	12/20/08
TITLE	
ANTENNA TOWER ASSY	
SCALE	
17480	
APPROVED	
DESIGN APPR	
MATERIAL	
PRINT	
APPLICATION	